Submillimeter–wave Observations of the Shocked Molecular Gas Associated with Supernova Remnants

A dissertation presented

by

Yuji ARIKAWA

Doctor of Science

Department of Astronomical Science,
School of Mathematical and Physical Science,
The Graduate University for Advanced Studies

in

1999 (School Year)

Contents

Abstract

Supernova remnants (SNRs), which are very energetic objects, are thought to have great influence on the interstellar medium. The expanding shock waves of SNRs compress, heat, and accelerate the interstellar gas. Because the interaction of SNR with the molecular cloud may play an important role in the next-generation star formation, it is of considerable interest to study the physical and chemical processes of the interaction.

In order to search for the interaction between SNR and the molecular cloud, we observed two SNRs, W28 and γ Cygni SNR, which are supposed to be EGRET gamma-ray sources, in submillimeter-wave CO (J=3–2) line (345 GHz ; 0.9 mm) by using the 15 m *James Clerk Maxwell Telescope* (JCMT). In W28, we detected a broad emission (maximum linewidth reaches $\Delta V \sim 70$ km s^{-1}), which suggests an interaction between SNR and the molecular cloud ("shocked gas"), as well as a narrow emission from the "unshocked gas". However, the broad emission was not observed toward γ Cygni SNR.

For W28, the distribution of the CO gas is similar to that of the 327 MHz radio-continuum emission, and tends to be stronger along the radio-continuum ridge. This suggest that the compression of magnetic fields in the SNR by the cloud results in enhanced synchrotron radiation. In addition, all of the OH (1720 MHz) maser spots, which trace the interaction between SNR and the molecular cloud, are located along the filament of the shocked gas. *These facts convincingly indicate that SNR W28 interacts with the molecular cloud.* Our observations are consistent with a hypothesis that the interaction of the SNR with the molecular cloud can be the origin of gamma-rays. Moreover, the distribution of the unshocked and shocked gas is clearly resolved. The shocked gas is filamentary, and surrounds the center of the supernova explosion. The unshocked gas is displaced by 0.4 – 1.0 pc outward with respect to the shocked gas. *The spatial relationship between shocked and unshocked gas has been clarified for the*

first time for the interaction between SNRs and molecular clouds.

In order to obtain the distribution of the cold gas and the physical properties of the molecular gas associated with W28, we observed the millimeter-wave CO (J=1–0) line (115 GHz ; 2.6 mm) by using the 45 m telescope of the *Nobeyama Radio Observatory* (NRO). It is found that the line intensity of CO (J=1–0) emission is stronger than that of CO (J=3–2) emission in the narrow component, and while the CO (J=3–2) emission is stronger than CO (J=1–0) emission in the broad component. The distribution of CO (J=1–0) globally resembles that of CO (J=3–2). The unshocked gas has a gas kinetic temperature of $T_{\rm kin} \lesssim 20$ K and a density of $n({\rm H_2}) \lesssim 10^3$ cm^{-3}, and a total mass of $M_{\rm unshocked} = 4 \times 10^3\ M_\odot$. On the other hand, the shocked gas has $T_{\rm kin} \gtrsim 60$ K, $n({\rm H_2}) \gtrsim 10^4$ cm^{-3}, and $M_{\rm shocked} = 2 \times 10^3\ M_\odot$. The total kinetic energy deposited in the shocked molecular gas is 3×10^{48} erg, which corresponds to 0.3 % of the energy of the supernova explosion.

To understand the chemistry related to carbon in the interaction region between SNR and the molecular cloud, we observed in CO (J=3–2) at 345 GHz (0.9 mm) and CI ($^3P_1$–$^3P_0$) at 492 GHz (0.6 mm) toward the four SNRs, W28, IC 443, W44, and W51C by using the Mt. Fuji submillimeter-wave telescope, which we developed. This telescope is the first submillimeter-wave telescope in Japan. With this telescope, we can observe CI ($^3P_1$–$^3P_0$) and CO (J=3–2) simultaneously. The spatial resolution is suitable for the observation of the molecular cloud scale. Except for IC 443, the CI ($^3P_1$–$^3P_0$) emission was detected. We found that the distribution of the CI ($^3P_1$–$^3P_0$) emission is similar to that of the CO (J=3–2) emission. It is clear that the known OH (1720 MHz) maser spots are located at the edge of clumps in all 4 SNRs. In the interaction region between SNR and the molecular cloud, the CI ($^3P_1$–$^3P_0$)/CO (J=3–2) peak intensity ratio and the N(CI)/N(CO) column density ratio tend to be high. On the other hand, in molecular clouds unrelated with SNR, the ratios are lower. *This result might imply that the interaction of SNR with the molecular cloud enhances the CI abundance.*

At present, though 220 SNRs are cataloged in our Galaxy, the observational examples of the interaction between SNR and molecular clouds are small in number. The shock region in W28 has rather simple structure and "edge-on". In the future, W28 can be one of the best regions for detailed studies of the interaction between SNR and the molecular cloud. By increasing the number of the observational examples, we can obtain better understanding of the molecular cloud associated with SNR.

Chapter 1

General Introduction

1.1 What is the Supernova Remnant (SNR)

1.1.1 Supernova Explosion

Between stars, there exists diffuse gas called the "interstellar gas". It is known that the star is formed by the contraction of the interstellar gas. The star evolves differently depending on its initial mass. In the final stage of the stellar evolution, if the mass of the star is smaller than 1.4 $M_{\odot}$ that is called the Chandrasekhar limit, then it becomes the white dwarf, and quietly ends. If the mass of the star is larger than the Chandrasekhar mass, it has two cases. If the stellar mass loss is large enough to reduce the stellar mass below the Chandrasekhar mass, the star becomes the white dwarf. If not, the star finally explodes as "supernova (SN) ".

The rate of the supernova explosion in the Galaxy is estimated to be approximately one per 10 – 30 year. The supernova explosion is classified into two categories, Type I SN and Type II SN depending on whether the hydrogen line exists in the spectrum and the shape of the light curve (Type I SN explosion do not show hydrogen line, but Type II SN explosion shows). The Type I SN blows the whole star away. The Type II SN blows the outer layer away, but the iron core at the center of the star remains as a neutron star or a black hole, although it is also possible that the explosion blows the star away. The neutron star can be observed as the pulsar, if the pulse beam is directed to the earth. The progenitor of the Type II SN explosion is more massive than 8 $M_{\odot}$. The total kinetic energy of the supernova is around 10^{51} erg, and is an

important energy source to the interstellar matter. The blast wave from the supernova explosion heats and sweeps up the interstellar gas, and propagates in the interstellar space. The star forms in the interstellar gas, and the star returns its material to the interstellar gas by the stellar mass loss and the supernova explosion.

1.1.2 The supernova remnants (SNRs)

The fossil of the supernova explosion is called the supernova remnant (SNR). In our Galaxy, 220 SNRs are cataloged by Green (1998). The SNR has the enormous energy of up to 10^{51} erg. Researches of SNRs are thought to provide us with the important clues of physical and chemical process in the interstellar matter. The SNRs cause heating and compression of the interstellar gas, formation of turbulent motion, compression of magnetic field, acceleration of cosmic ray, and so on. They will determine the structure and evolution of the whole Galaxy. Heavy elements such as Fe, Si, O, C which are formed in the star will be released into the space. The released heavy elements play an important role in the formation of the solar system and the origin of life. Therefore, SNR is a very important object.

The shock wave from SNR collides with interstellar gas in the surroundings, and the gas is heated to high temperature, and the X–ray is radiated. The charged particles such as the electron are accelerated to very high energy, and the magnetic field was compressed and the electron spiraled the magnetic field radiates in the synchrotron radiation at radio and other wave lengths.

1.1.3 Classification of SNR

The standard of judgments identified as a SNR are to show that it has the spherical shell structure, the radio continuum emission in synchrotron processes with the nonthermal spectrum, or liner polarization. The feature of SNR are various morphology, then have classified into three categories from the morphology.

F : filled–center type (Plerionic)

S : shell–like type

C : composite type (shell–like type containing Plerions).

In the filled–center type (F–Type) SNR, the radio–continuume distribution is filled or centrally peaked. The typical example of this type is the Crab Nebula, therefore they are also called the Crab–like SNR. A number of this type have been discovered in the last decade. The energetic electrons which radiates the synchrotron emission are presumably supplied by the central neutron star. (Weiler & Panagia 1980).

The shell–like type (S–Type) SNR has a spherical shock shell. The Cygnus Loop and IC 443 (see Figure 1.2) are typical examples of this type at the late evolutionary stage. Cas A is an examples at the early evolutionary stage. Energetic electrons, which radiates the synchrotron emission, are accelerated by the shock wave traveling into the interstellar medium. (e.g. Reynolds & Chevalier 1981).

The composite type (C–Type) SNR shows both a centrally peaked emission together with a shell–like morphology. The Vela SNR and CTB 80 belong to this type. Raymond (1984) proposed that this type is at the intermediate evolutionary stage between F–Type (early) to S–Type (late), or Weiler (1985) proposed that the type difference is due to environment difference.

1.1.4 Evolution of SNR

The ejecta from the supernova explosion collides the interstellar gas, and it makes the shock wave. The SNR expands differently depending on its age. The typical evolution of SNR is divided into four stages as follows (Figure 1.1).

Free expansion phase ($t = 0$–10^3 yrs)

At the first stage, the expansion of the shock wave is hardly hindered by the interstellar gas, since the mass of the supernova ejecta is larger than that of the gas swept up from the interstellar gas. Therefore, SNR expands almost freely without decelerating the shock velocity. Assuming the spherical shock in the uniform medium, the total energy of the explosion is $E_0 \sim \frac{1}{2} M_0 v^2$, where M_0 is the mass of the supernova ejecta. The velocity at this phase is $v \sim 4000 - 10000$ km s^{-1}. A typical example of this phase is the Crab Nebula.

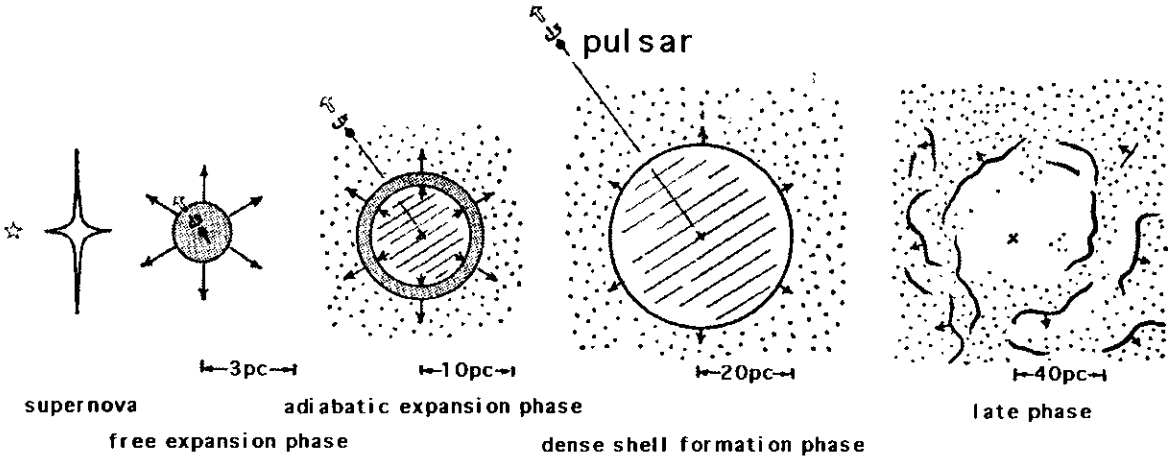

Fig. 1.1 The evolution of SNR

Adiabatic expansion phase ($t = 10^3$–10^4 yrs)

When the mass accumulated from interstellar matter M becomes equal the mass of ejecta from supernova M_0, that is $M_0 \sim M = \frac{4\pi}{3} r^3 \rho_0$ (where ρ_0 is the surrounding gas of density), the velocity of the gas begins to decrease. If the cooling time of the gas by the radiation is longer than time scale of the expansion of SNR, then the total energy of SNR is preserved, the spherical shock adiabatically expands. This phase is called the adiabatic phase or "Sedov phase". From a Sedov's similarity solution, it is shown that the radius of spherical shock r increases with time t as

$$r = \left(\frac{2E_0}{\rho_0}\right)^{1/5} t^{2/5}.$$

The velocity at this phase is of order $v \sim$ several hundred km s^{-1}. This velocity is correspondent to a temperature of order 10^6 - 10^7 K, and the cooling time of the gas near the shock is $t \sim 10^4$ yrs. Therefore this phase lasts 10^4 yrs

Dense shell formation phase ($t = 10^4$–10^5 yrs)

At this stage, since the radiative cooling of accumulated gas begins to be effective, the dissipation of the energy becomes important, and the adiabatic approximation is

not good any more. Behind the shock front, the temperature and pressure decrease. The gas is compressed strongly, and the dense shell is formed. The density of shell is $10^2 - 10^3$ cm^{-3}. The Cygnus Loop and IC 443 are typical examples of this phase. Due to various instabilities (e.g. thermal and hydorodynamical), the shell is fragmented into numerous filaments and sheets. The thickness of the dense shell is 0.1 – 1 pc, is much smaller than the radius (20 – 30 pc) of the SNR in this phase.

Late phase ($t > 10^5$ *yrs*)

At this stage, the velocity of shock wave decreases down to $v \lesssim 50$ km s^{-1}, the turbulent motion of interstellar gas (a few tens km s^{-1}) becomes important, the shape of SNR largely deviates from the shell structure. Finally, the shock wave dissipates in the interstellar space, and it disappears.

1.1.5 Σ–D relation and distance estimation

When the SNR shell expands, the surface brightness of the radio continuum decreases. The mean surface brightness Σ, which is defined as the total flux density S of SNR divided by the solid angle Ω, does not depend on the distance. One can plot Σ against the linear diameter of D of SNR. Huang & Thaddeus (1985) obtained

$$\log \Sigma_{1\ \mathrm{GHz}} = (-15.44 \pm 0.50) \pm (-3.21 \pm 0.32)\ \log D$$

where $\Sigma_{1\ \mathrm{GHz}}$ is the surface brightness at 1 GHz in units of W m^{-2} Hz^{-1} str^{-1}, and D is in pc. This is called the "Σ–D relation". We can estimate the distance by comparing the linear diameter D from the observed mean surface brightness Σ and the observed angular diameter.

1.2 Interaction with the Interstellar Matter

1.2.1 Molecular clouds interacting with SNR

The interstellar gas consists of various phases (cf. Myers 1978), and it is not uniform. The evolution of supernova remnant can be greatly affected by the presence of a nearby molecular cloud, if any. If the supernova explosion occurs in the vicinity of

the molecular cloud, the shock wave from supernova remnant collides with the molecular cloud, and the cloud surface is accelerated, heated, and compressed by the interaction. Some suggested that such interaction can be a trigger of the star formation (e.g. Opik 1953, Chevalier 1974). Moreover, the interaction will be related to the energy balance of the Galaxy.

Green et al. (1998) cataloged 220 SNRs in our Galaxy. The observational examples of interaction between SNR and the molecular cloud were very small in number. There is a few SNR with the direct observational evidence (emission from the molecular gas accelerated and compressed by the interaction). Until now,

IC 443 (e.g. DeNoyer 1979a; White et al. 1987, 1994; Burton et al. 1988)
W44 (Seta et al. 1998)
W51C (Koo & Moon. 1997a, 1997b)
3C 391 (Wilner et al. 1998; Reach & Rho 1999)

have been reported to show the shock-accelerated molecular gas. IC 443 has long been the unique example before 1997. Therefore, for two decades, the detailed study of the interaction between SNR and the molecular cloud has been made only for IC 443. From the morphological argument,

G109.1−1.0 (Tatematsu et al. 1985,1987,1990a)
HB21 (Tatematsu et al. 1991b)
γ Cygni SNR (Fukui & Tatematsu 1988)
W28 (Wootten et al. 1981)

and some more have been suggested to interact with the molecular cloud from CO observation, although they were not known to have the accelerated molecular gas. The physical processes and the detailed structure of the molecular gas in such interaction region is not well understood yet.

From survey observations, Huang & Thaddeus (1986) found the existence of molecular clouds in the vicinity of 26 SNRs in the outer Galaxy by using the GISS–Columbia 1.2 m telescope. However, since the angular resolution was too poor to identify the interaction.

1.2.2 A previous example : IC 443

The distance to IC 443 (Figure 1.2) is estimated to be $d \sim 1500$ pc (e.g. Sharpless 1965). The age is estimated to be 5×10^4 yrs (Lozinskaya 1969, 1975). For two decades, IC 443 was the sole observational example of the interaction between SNR and the molecular cloud. Therefore, observations in various molecular lines have been carried out for IC 443. (e.g. Cornett et al. 1977; DeNoyer 1978, 1979a, 1979b, 1983; DeNoyer & Frerking 1981; Burton et al. 1988, 1990; White et al. 1987; Huang et al. 1986; Ziurys et al. 1989; Dickman et al. 1992; Wang & Scoville 1992; Turner et al. 1992; van Dishoeck et al. 1993; Tauber et al. 1994; Richter et al. 1995).

There exists small dark cloud with a total mass of $\lesssim 10^4$ $M_\odot$ in the vicinity of IC 443 (Cornett et al. 1977). The evidence for the interaction between IC 443 and the molecular cloud was first presented by DeNoyer (1978) observing the high velocity neutral hydrogen (HI) line emission. Subsequently, in the region where the interaction is expected, the broad profile (wing) of the molecular line, which suggests the molecular gas accelerated due to interaction with SNR, was detected in various molecular lines. The CO (J=1–0) profile is asymmetric and broad ($\gtrsim$ 20 km s^{-1}) (e.g. DeNoyer & Frerking 1981, Huang et al. 1986, White et al. 1987). The distribution of the wing emission is shell-like, and consists of several clumps. The vibrationally excited emission of v=1–0 $S(1)$ line of shocked molecular hydrogen (wavelength is 2.122 μm), which traces hot ($\sim$ 7000 K) gas, was detected by Burton et al. (1988). Furthermore, shocked [OI] 63 μm line emission was detected in the same direction (Burton et al. 1990). From the viewpoint of the interstellar shock chemistry, the observations of various molecules have been carried out. The molecular species which indicate shocks, such as SiO, were detected (Ziurys et al. 1989, Turner et al. 1992, and van Dishoeck et al. 1993). However, observations of other molecular (e.g. HCO^+, HCN, and so on) indicate that the observed abundances do not differ by more than a factor of a few from those observed in cold, quiescent clouds (Ziurys et al. 1989, Turner et al. 1992, and van Dishoeck et al. 1993). Enhancement of the relative abundance of the neutral atomic carbon as a result of the interaction in IC 443 was suggested by Phillips et al. (1993) and White (1994). In the shock region of IC 443, the hard X-ray emission was detected (Keohane 1997). As described in detail in the following subsection, the region where IC 443 interacts is also

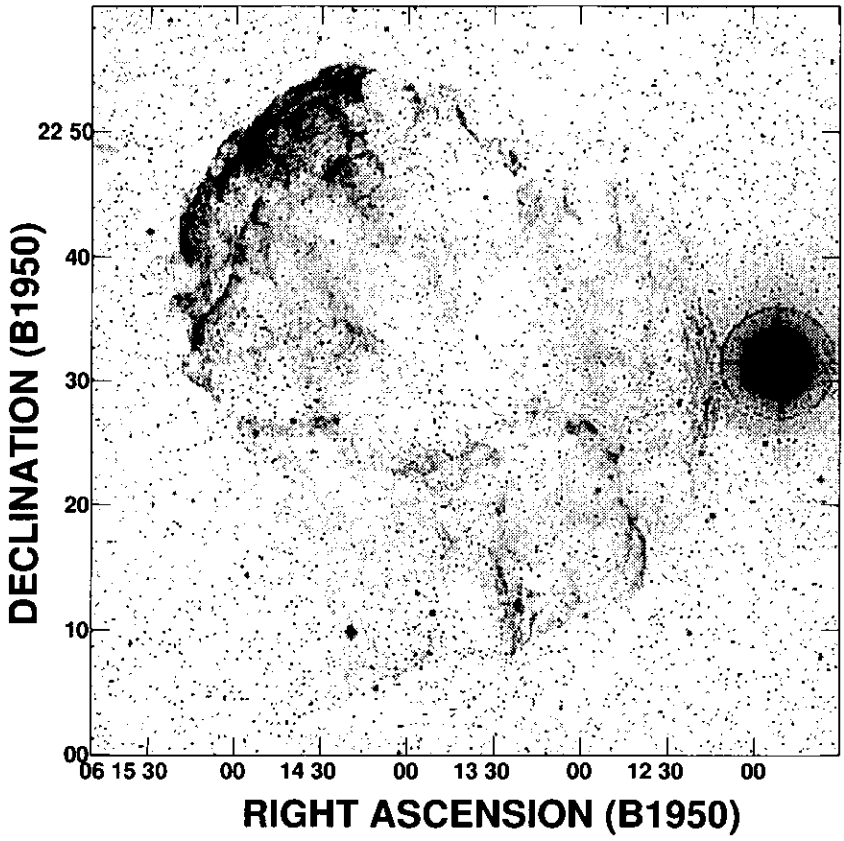

Fig. 1.2.— Digitized Sky Survey picture of the supernova remnant IC 443. At the distance of $\sim$ 1500 pc, 10′ corresponds to $\sim$ 4.4 pc. The bright star lying just to the west of the SNR is η Geminorum.

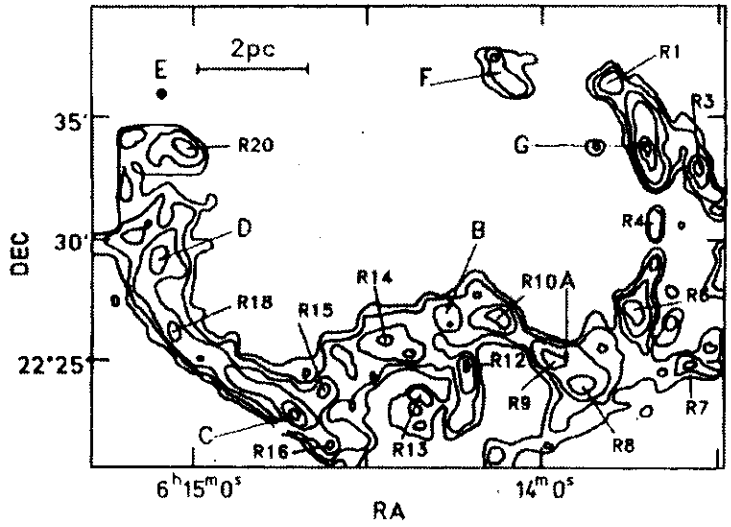

Fig. 1.3.— Map of shocked molecular hydrogen emission at 2.1 μm in the same region with the positions of the various clumps indicated (van Dishoeck et al. 1993)

related to the OH (1720 MHz) maseremission and possibly the gamma-ray emission.

1.2.3 Observations at various wavelengths

1720 MHz OH maser and 22 GHz H_2O maser

It has become clear that the satellite line from the ground state of the hydroxyl radical (OH) at 1720.53 MHz ($^2\prod_{3/2}, J = \frac{3}{2}, F$ =2-1) is a powerful tool for the research of the interaction between SNRs and molecular clouds, since the detection toward SNR W28 (Frail, Goss & Slysh 1994). Elitzur (1976) theoretically showed that the OH (1720 MHz) maser can be collisionally pumped by H_2 under the conditions of a kinetic temperature of $T_{\rm Kin} \sim 25$ - 200 K and a molecular hydrogen density of $n(H_2) \sim 10^3$ - 10^5 cm^{-3}. In the latest research, Lockett (1999) has constrained the physical condition for the pumping of the OH (1720 MHz) maser : the kinetic temperatures is 50 K $\lesssim T_{\rm kin} \lesssim$ 125 K, the molecular hydrogen density is $n(H_2) \sim 10^3$ cm^{-3}, and the OH column density is of order 10^{16} cm^{-2}.

Recently, many researchers have carried out the observations of the OH (1720 MHz) maser toward other galactic SNRs (Frail et al. 1996; Yusef-Zadeh et al. 1996; Green et al. 1997; Claussen et al. 1997, 1999; Koralesky et al. 1998, Frail & Mitchell 1998). Especially, Green et al. (1997) surveyed for the OH (1720 MHz) masers emission in the directions of 160 SNRs, and detected maser emission in a total of 17 SNRs (CND Sgr A East, Sgr D SNR, G1.4-0.1, W28, G16.7+0.1, Kes 69, 3C 391, W44, W51C, IC 443, CTB 33, CTB 37A, G349.7+0.2, G357.7+0.3, G357.7-0.1, G359.1-0.5). The 10 % of observed samples showed OH (1720 MHz) masers. From these results, it becomes clear that the SNR interacting with the molecular cloud only emits OH maser at 1720 MHz, but does not emit the other fine structure lines (1612, 1665, or 1667 MHz) and that OH (1720 MHz) maser is emitted by collisional excitation of the OH with the H_2 molecules. This is in contrast with OH masers in star formation region and evolved stars. Lockett et al. (1999) concluded that conditions for OH (1720 MHz) maser is satisfied only if the interaction of the SNR with the molecular cloud accompanies C-Type shocks.

The water maser (H_2O maser) was detected in W44 (Seta et al. 1997), but it was found that this maser is due to a late-type giant or supergiant star along the line of

sight to W44 and are not associated with the SNR (Claussen et al. 1999).

Thermal molecular lines

Detailed studies of various molecular lines have been made for only IC 443. Previously, the HCO^+ and HCN abundances ware reported to increase in the SNR shocked molecular gas (Dickinson et al. 1980, DeNoyer & Frerking 1981, White et al. 1987). However, more recent observations suggest that the molecular abundances are close to those in cold, quiescent clouds (Ziurys et al. 1989; Turner et al. 1992; van Dishoeck et al. 1993). Similar results were obtained in other molecular species (e.g. HNC, CS, SO, H_2CO, C_2H, $H^{13}CO^+$) except for SiO. The abundance of SiO, which is thought to be evaporated from the dust by shock, seems to be enhanced. Turner (1993) divided the observed molecular lines into two groups : Group 1 species ($n(H_2)$ ~(2 – 8) × 10^5 cm^{-3}, $T \lesssim$ 100 K) and Group 2 species ($n(H_2) \gtrsim 10^6$ cm^{-3}, $T \sim$ 200 – 300 K). van Dishoeck et al. (1993) also leads to the similar result (the lower density gas ($n(H_2) \sim 10^5$ cm^{-3}, $T \sim$ 80 K) and the higher density gas ($n(H_2) \sim 3 \times 10^6$ cm^{-3}, $T \sim$ 200 K)). It seems that the shocked gas is at least two phases.

Phillips et al. (1993) and White (1994) found that the abundance ratio of the atomic neutral carbon (CI) to CO is enhanced in the interaction region of IC 443. Phillips et al. (1993) suggested that the ratio marks the radiative precursor of the shock, while White (1994) suggested that it is due to cosmic ray ionization.

X–rays

The morphologies of the X–ray and radio continuum emission often resemble each other. However, some SNRs that have shell–like radio continuum morphologies appear centrally concentrated in the X–ray emission. Rho & Petre (1998) defined mixed–morphology (MM) supernova remnants that show shell–like in the radio continuum emission and that are centrally filled in the X–ray, and identified 19 SNRs (W28, W44, 3C 400.2, Kes 27, MSH 11–61A, 3C 391, CTB 1, W51C, CTA 1, W63, HB21, IC 443, Kes 79, HB3, G327.1−1.1, CTB 104A, W49B, 3C 397, MSH 11–54) as MM SNRs by using the *ROSAT* and the *ASCA* imaging data. They suggest the MM SNR interacts with the molecular cloud. At least 8 % of all Galactic SNRs and as much as 35 %

of all X–ray detected Galactic SNRs are MM SNRs. Most of these SNRs accompany molecular and/or HI clouds, and some SNRs accompany strong infrared line emission or OH (1720 MHz) masers.

Gamma–rays

It was proposed a long time ago that SNR shock is the place of cosmic ray origin and acceleration (e.g. Woosley & Weaver 1981). The gamma ray emission is expected to arise from interaction of cosmic rays with the interstellar matter via high–energy electron bremsstrahlung, nucleon–nucleon processes, the synchrotron emission, or inverse Compton scattering of low energy photons (Hunter et al. 1996). Together with the pulsar, active galactic nuclei (AGN), and gamma–ray bursts, the interaction between SNR and the molecular cloud can be one of the important mechanisms of the origin of gamma–rays.

Pollock (1985) identified two gamma–ray sources (2CG078+01 and 2CG006−00) observed with the *COS–B* satellite with radio–bright SNRs (G78.2+2.1 and W28, respectively), and proposed that the gamma–ray emission is a result of the interaction between SNR and the molecular cloud. In 1991, the *Compton Gamma Ray Observatory* (CGRO), which has the Energetic Gamma Ray Experiment Telescope (EGRET) aboard, was launched. Sturner and Dermer (1995) investigated the First EGRET catalog of high–energy gamma–ray sources (Fichtel et al. 1994) and found that four of 37 unidentified gamma–ray sources are possibly associated with nearby SNRs. They compared possible gamma–ray production mechanisms, and concluded that high–energy protons accelerated by the SNR shock wave collide with pions (π^0), which decay to gamma–rays. Esposito et al. (1996) investigated about 130 unidentified gamma–ray sources in the second EGRET catalog of high–energy (100 MeV – 10 GeV) gamma–ray sources (Thompson et al. 1995) and found that four SNRs (IC 443, W28, W44, and γ Cygni) apparently accompanying molecular cloud are gamma–ray sources.

1.3 Submillimeter–wave line emission

There were only a few observational examples of the interaction of the SNR with the molecular cloud. This low detection can be partly because observations were made

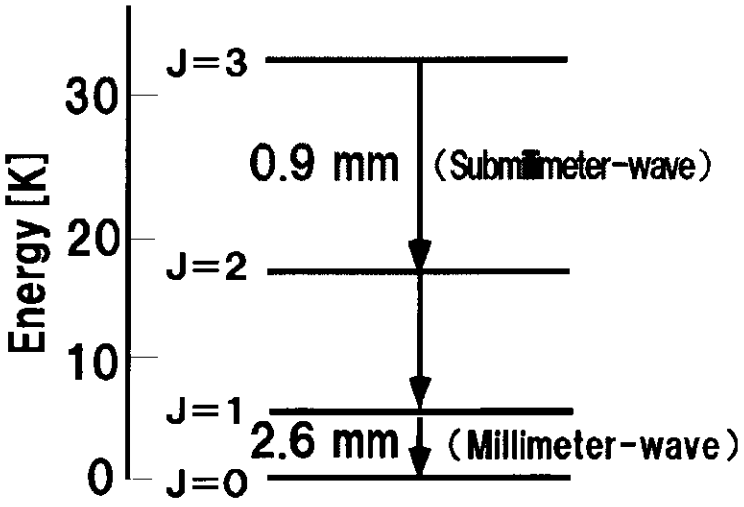

Fig. 1.4.— The CO rotational energy level diagram. CO (J=1–0) line in the millimeter-wave regime can emit at a temperature of $\leq$ 10 K. On the other ward, CO (J=3–2) line in the submillimeter-wave regime needs warmer ($\geq$ 20 K) gas to be emitted.

with millimeter-wave lines. It is clear from Figure 1.4 that the line in the millimeter-wave regime is radiated mainly from cold ($\sim$ 10 K) gas. Furthermore, the critical density, at which the collisional de-excitation rate be comes comparable to the spontaneous transition rate, increases with increasing J of the upper level ($\propto J^3$). So, low-J lines trace low density gas. Therefore, unrelated cold, quiescent molecular gas which does not interact with SNR is also detected by observing millimeter-wave lines. To survey for the interaction of SNRs with molecular clouds, millimeter-wave lines are not the best. The shocked molecular gas with high-temperature and high-density excites the molecule to higher energy levels by more frequent collision with the hydrogen molecule with higher thermal energy, and then, the line intensity is expected to be strong in the submillimeter-wave regime. Lines in the submillimeter-wave regime (for example, CO (J=3–2)) are more sensitive to dense ($\gtrsim 3 \times 10^3$ cm^{-4}), warm ($\gtrsim$ 30 K) gas. Moreover, due to the statistical weight $2J+1$, the line is more opaque, if thermalized, and we can make sensitive observations. Rotational lines in submillimeter-wave regime are very good tools in order to study the interaction between SNR and the molecular cloud. With this in mind, we search for the SNR-cloud interaction by using a line of the submillimeter-wave regime emission.

1.4 Thesis Outline

We carried out observations by using lines of submillimeter-wave regime in order to clarify the interaction between SNR and molecular cloud. The observed SNRs are W28, γ Cygni, W44, W51, and IC 443. The outline of this study is as follows.

We first describe in Chapter 2 observations of submillimeter-wave CO (J=3–2) line (0.9 mm, 345 GHz) by using the 15 m James Clerk Maxwell Telescope (JCMT) at Hawaii toward SNRs, W28 and γ Cygni SNR. In chapter 3, we report observations of millimeter-wave CO (J=1–0) line (2.6mm, 115 GHz) by using the 45 m telescope at Nobeyama Radio Observatory (NRO) toward SNR W28. Here, we study the distribution of the cold, unshocked gas and to estimate physical parameter (temperature, density, mass, and energy). In Chapter 4, we describe observations of CO (J=3–2) and CI ($^3P_1$–$^3P_0$) by using the Mt. Fuji submillimeter-wave telescope toward four SNRs, which interact with molecular clouds (IC 443, W28, W44, and W51C). Finally, the conclusions are given in Chapter 6, along with planned future work.

In Appendix A, we introduce the Mt. Fuji submillimeter-wave telescope, which is the first submillimeter-wave telescope in Japan. The control program for the Mt. Fuji submillimeter-wave telescope, which I developed, is explained in Appendix B. In Appendix C, we explain the large velocity gradient (LVG) model in order to obtain the physical parameters.

References

Becker, R.H., Boldt, E., Holt, S.S., Serlemitors, P.J., & White, N,E. 1980, ApJ, 237, L77

Burton, M.G., Geballe, T.R., Brand, P.W.J.L., Webster, A.S. 1988, MNRAS, 231, 617

Burton, M.G., Hollenbach, D.J., Haas, M.R., Erickson, E.F. 1990, ApJ, 355, 197

Chevalier, R.A., 1974, ApJ, 188, 501

Claussen, M.J., Frail, D.A., Goss, W.M., Gaume, R.A. 1997, ApJ, 489, 143

Claussen, M.J., Goss, W.M., Frail, D.A., & Desai, K. 1999, ApJ, 522, 349

Cornett, R.H., Chin, G., & Knapp, G.R. 1977, A&A, 54, 889

DeNoyer, L.K. 1983, ApJ, 264, 141

DeNoyer, L.K. 1978, MNRAS, 183, 187

DeNoyer, L.K. 1979a, ApJ, 232, L165

DeNoyer, L.K. 1979b, ApJ, 228, L41

DeNoyer, L.K., & Frerking, M.A. 1981, ApJ, 246, L37

Dickman, R.L., Snell, R.L., Ziurys, L.M., Huang Y.–L. 1992, ApJ, 400, 203

Elitzur, M. 1976, ApJ, 203, 124

Esposito, J.A., Hunter, S.D., Kanbach, G., Sreekumar, P. 1996, ApJ, 461, 820

Fichtel, C.E., et al. 1994, ApJS, 94, 551

Frail, D.A., Goss, W.M., Slysh, V.I. 1994, ApJ, 424, L111

Frail, D.A., Goss, W.M., Reynoso, E.M., Giacini, E.B., Green, A.J., Otrupeck, R. 1996, AJ, 111, 1651

Frail, D.A., & Mitchell, G.F. 1998, ApJ, 508, 690

Fukui Y., Tatematsu K. 1988, in IAU Colloquium 101, Supernova Remnants and Interstellar Medium, ed R.S. Roger, T.L. Landecker (Cambridge University Press, Cambidge) p261

Green, A.J., Frail, D.A., Goss, W.M., Otrupcek, R. 1997, AJ, 114, 2058

Green D.A. 1998, A Catalogue of Galactic Supernova Remnants (1998 September version) (Mullard Radio Astronomy Observatory, Cambridge)

Hunag, Y.–L., Dickman, R.L., & Snell, R.L. 1986, ApJ, 302, L63

Huang, Y.–L., & Thaddeus P. 1985, ApJ, 295, L13

Huang, Y.–L., & Thaddeus P. 1986, ApJ, 309, 804

Hunter, S.D., et al. 1994, ApJ, 436, 216

Keohane, J.W., Petre, R., Gotthelf, E.V., Ozeki, M., Koyama, K. 1997, ApJ, 484, 350

Koo, B.–C., & Moon, D.–S. 1997a, ApJ, 475, 194

Koo, B.–C., & Moon, D.–S. 1997b, ApJ, 485, 263

Koralesky, B., Frail, D.A., Goss, W.M., Claussen, M.J., Green, A.J. 1998, ApJ, 116, 1323

Lockett, P., Gautheir, E., Elitzur, M. 1999, ApJ, 511, 235

Lozinskaya, T.A. 1969, SvA, 12, 192

Lozinskaya, T.A. 1975, SvAL, 1, 35

Myers, P.C. 1978, ApJ, 225, 380

Raymond, J.C. 1984, ARAA, 22, 75

Reach, W.T., & Rho, J. 1999, ApJ, 511, 836

Reynolds, S.P., & Chevalier, R.A. 1981, ApJ, 245, 912

Rho, J., & Petre, R. 1998, ApJ 503, L167

Phillips, T.G., Keene, J., van Dishoeck, E.F. 1993, in The Physics and Chemistry in In terstellar Molecular clouds, ed G. Winnewisser G.C. Pelz, (Springer: Berliu) p.96

Richter, M.J., Graham, J.R., Wright, G.S., 1995, ApJ, 454, 277

Pollock, A.M.T. 1985, A&A, 150, 339

Seta, M., Hasegawa, T., Dame, T.M., Sakamoto, S., Oka, T., Handa, T., Hayashi, M., Morino, J., Sorai, K., Usuda, K.S. 1998, ApJ, 505, 286

Sharpless, S. 1965, In Stars and Stellar Systems, Vol.5, Galactic Structure, P. 136, eds Blaauw, A., & Schmidt, M., University of Chicago Press.

Sturner, S.J., Dermer, C.D. 1995, A&A, 293, L17

Tatematsu K., Nakano, M., Yoshida, S., Wiramihardja, S.D., Kogure, T. 1985, PASJ, 37, 345

Tatematsu, K., Fukui, Y., Nakano, M., Kogure, T., Ogawa, H., Kawabata, K. 1987, A&A, 184, 279

Tatematsu, K., Fukui, Y., Iwata, T., Seward, F.D., Nakano, M. 1990a, ApJ, 351, 157

Tatematsu, K., Fukui, Y., Landecker, T.L., Roger, R.S. 1990b, A&A, 237, 189

Tauber, J.A., Snell, R.L., Dickman, R.L., Ziurys, L.M., 1994, ApJ, 421, 570

Thompson, D.J., et al. 1995, ApJS, 120, 461

Turner, B.E., Chan, K., Green, S., & Lubowich D.A. 1992, ApJ, 399, 114

van Dishoeck, E.F., Jansen, D.J., Phillips, T.G. 1993, A&A, 279, 541

Wang, Z., & Scoville, N.Z. 1992, ApJ, 386, 158

White, G.J., Rainey, R., Hayashi, S.S., Kaifu, N. 1987, A&A, 173, 337

White, G.J. 1994, A&A, 283, L25

Weiler, K.W. 1985, in The Crab Nebula and Related Supernova Remnants, ed. M.C. Kafatos and R.B.C. Henry (Cambidge: Cambridge University Press), p.227

Weiler, K. W., & Panagia, N. 1980, A&A, 90, 269

Wilner, D.J., Reynolds, S.P., Moffett, D.A. 1998, AJ, 115, 247

Woosley, S.E., & Weaver, T.A. 1981, ApJ, 243, 651

Wootten, H.A. 1977, ApJ, 216, 440

Wootten, H.A. 1981, ApJ, 245, 105

Yusef-Zadeh, F., Roberts, D.A., Goss, W.M., Frail, D.A., Green, A.J. 1996, ApJ, 466, L25

Zirys, L.M., Snell, R.L., Dickman, R.L. 1989, ApJ, 341, 857

Chapter 2

CO (J=3–2) observations toward W28 and γ Cygni SNR

Abstract

We observed two SNRs, W28 and γ Cygni SNR, which are supposed to be EGRET gamma-ray sources, in submillimeter-wave CO (J=3–2) line (345 GHz, 0.9 mm) in order to search for the interaction between the supernova remnant (SNR) and the molecular cloud by using the 15 m *James Clerk Maxwell Telescope* (JCMT). In W28, a broad CO (J=3–2) line emission (maximum linewidth reaches $\Delta V \sim 70$ km s^{-1}), which suggests an interaction between the molecular cloud and SNR, was detected, but not detected toward γ Cygni SNR. For SNR W28, the distribution of the CO (J=3–2) gas is similar to that of the 327 MHz radio-continuum emission (Frail et al. 1994), and tends to be stronger along the radio-continuum ridge. In addition, the distribution of the unshocked and shocked gas is clearly resolved. The shocked gas is filamentary, and surrounds the center of the supernova explosion. The unshocked gas is displaced by 0.4 – 1.0 pc outward with respect to the shocked gas. The spatial relationship between shocked and unshocked gas has been clarified for the first time for the interaction of SNRs with molecular clouds. All of the known OH (1720 MHz) maser spots are located along the filament of the shocked gas. These facts convincingly indicate that SNR W28 interacts with the molecular cloud.

2.1 Introduction

In this chapter, we report on high–resolution submillimeter–wave observations of the molecular gas toward SNR W28 and γ Cygni SNR in CO (J=3–2) emission. It has been proposed that the interaction of SNR with the molecular cloud is one of the possible mechanisms for the origin of gamma–rays (Pollock 1985, Sturner & Dermer 1995, Esposito et al. 1996). Esposito et al. (1996) suggested that four SNRs (IC 443, W44, W28, and γ Cygni SNR) are gamma–ray sources based on the second catalog from the *Energetic Gamma–Ray Experiment Telescope* (EGRET) instrument (100 MeV – 2 GeV) aboard the *Compton Gamma Ray Observatory* (CGRO). The four SNRs are listed in Table 2.1. Two (W28 and γ Cygni SNR) were selected for our observations, because the position of the gamma–rays is known with better accuracy. We planned to examine the relationship between gamma–rays and the interaction.

2.1.1 γ Cygni SNR (G78.2+2.1)

γ Cygni SNR is a circular SNR with a diameter of 60 arcmin and has a radio bright region in the southeast. The distance to the SNR is 1.8 $\pm$ 0.6 kpc (Higgs et al. 1977). The SNR age is estimated to be (1.4 $\pm$ 0.6) $\times$ 10^4 *yrs* (Landecker et al. 1980). Using the Nagoya 4 m radio telescope, Fukui & Tatematsu (1988) made millimeter–wave CO (J=1–0) observations toward γ Cygni SNR. There exist two molecular clouds in the southeast direction of γ Cygni SNR, and they suggested from the morphology, that dynamical interaction of SNRs with molecular clouds. The EGRET gamma–ray point source, which is the strongest among the four, is located near the molecular cloud. The X–ray emission fills inside the SNR (Takahashi et al.).

2.1.2 W28 (G6.4–0.1)

The SNR W28 is classified as a composite–type SNR, which appears as a shell of 42 arcmin diameter in the radio continuum emission (Green 1998), and is located in a complex region of the Galactic plane (l = 6°.4, b = –0°.2). Wootten (1981) has pointed out the possibility of an interaction based on the kinetic signature of the line broadening (ΔV $\sim$ 12 km s^{-1} at full width half maximum) from observations of millimeter–wave CO (J=1–0) line with a 2′.3 beam. However, DeNoyer (1983) did not

TABLE 2.1

Characteristics of the SNRs in the Survey (Esposito et al. 1996)

Name	Diameter [arcmin]	EGRET Source	Position l	Position b	Error circle [arcmin]
γ Cygni SNR	60	2EG J2020+4026	78.12	2.10	6
W28	42	2EG J1801−2312	6.73	−0.14	9
IC 443	45	2EG J0618+2234	189.13	3.19	12
W44	35 × 42	2EG J1857+0118	34.80	−0.76	27

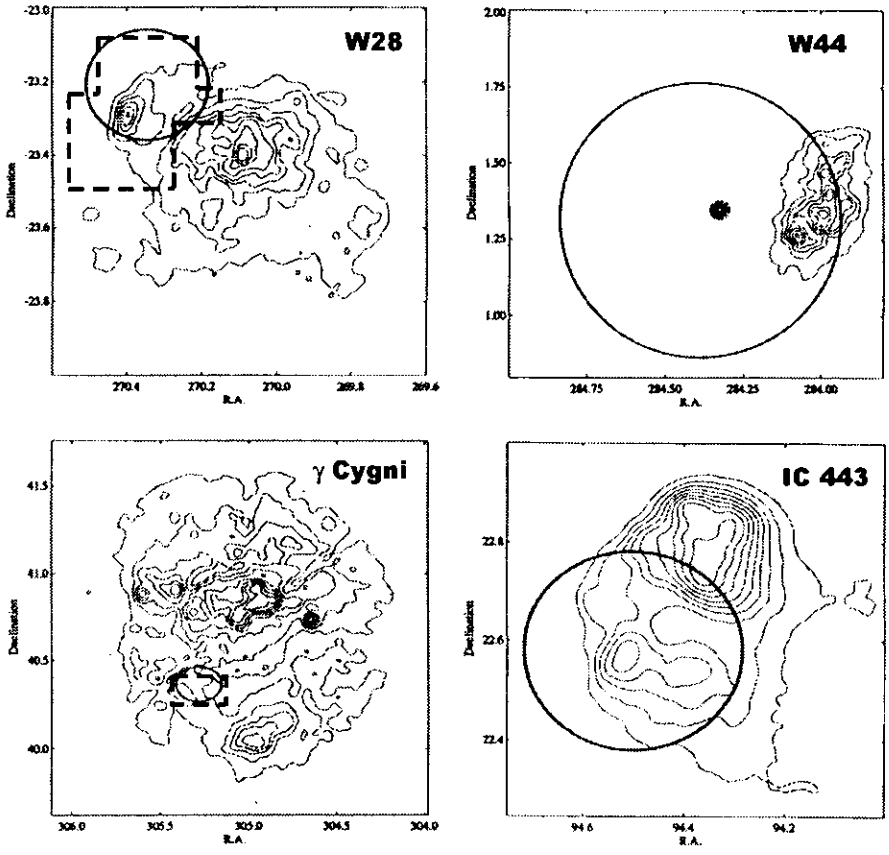

Fig. 2.1.— The 95 % confidence contour of the detected gamma-ray emissions is shown as a thick circle. The figure includes *ROSAT* contours of the supernova remnants. (Esposito et al. 1996). The dashed lines in γ Cygni SNR and W28 show the region which we observed. The coordinates are in J2000.

obtain any evidences of an interaction, such as an enhancement of the abundances of various molecular species (HCO+, HCN, CS, N_2H+, OCS, and SO_2). Frail et al. (1994), Green et al. (1997), and Claussen et al. (1997) detected OH (1720 MHz) masers, which are thought to be collisionally excited by the passage of SNR shock waves through a molecular cloud, in the northeast of SNR W28. The EGRET position is also located in the north–eastern side of SNR W28, which is close to the molecular cloud observed by Wootten (1981). The SNR age is estimated to be 6×10^4 *yrs* (Lozinskaya 1974). The estimated distance to the SNR ranges from 1.8 kpc (Goudis 1976 based on the Σ–D relation) to 4.0 kpc (Lozinskaya 1981 based on the mean optical velocity).

2.2 Observations

Figure 2.1 shows *ROSAT* images as thin contours and EGRET error circle as a thick ellipses (Esposito et al. 1997). The line used for observations is submillimeter–wave emission of CO in order to detect the molecular gas which has a high temperature and a high density by the interaction. The CO (J=3–2) data were obtained by using the 15 m James Clerk Maxwell Telescope (JCMT) on Mauna Kea in 1997 July. This telescope has a beam size of $\sim 13''$ and a main–beam efficiency $\eta_{\rm mb}$ of ~ 61 %. The receiver frontend is a superconductor–insulator–superconductor (SIS) receiver with image band rejection. The SSB system noise temperature was 700 – 1500 K. The employed backend was a digital autocorrelation spectrometer (DAS), having a spectral resolution of 374 kHz (0.43 km s^{-1}). The data were obtained in the on–the–fly (OTF) method at spacings of $15''$. The total integration time was typically 10 s for each position. For SNR W28, the observed map center is the EGRET position of RA(B1950) = $17^{\rm h}58^{\rm m}20^{\rm s}.3$, DEC(B1950) = $-23°12'23''$, and the observed region is $25' \times 25'$, which covers the EGRET error circle (95% confidence; Esposito et al. 1996). For γ Cygni SNR, the observed map center is the EGRET position of RA(B1950) = $20^{\rm h}19^{\rm m}20^{\rm s}.9$, DEC(B1950) = $40°12'20''$, and the observed region is $10' \times 13'$. In this chapter, we report the line intensity in terms of the corrected antenna temperature ($T_{\rm A}{}^*$).

2.3 Results

2.3.1 γ Cygni SNR

Figure 2.2 shows the integrated intensity map of the CO (J=3–2) emission toward γ Cygni SNR with typical profiles at selected positions. The map represents the intensity integrated between $V_{\rm LSR} = -10$ km s^{-1} and 5 km s^{-1}. In Figures 2.6 and 2.7, the channel maps at 1 km s^{-1} velocity intervals are shown, and the velocity of the channel center is labeled at the upper right corner of each panel.

For γ Cygni SNR, the linewidth of profiles is narrow ($\Delta V \sim 1 - 2$ km s^{-1}). The two clumps were detected in the southwest side of the observed region. One clump has a radial velocity of $V_{\rm LSR} = -8$ km s^{-1}, and the other has $V_{\rm LSR} = -3$ km s^{-1}. The antenna temperature is $T_{\rm A}* = 16 - 17$ K at the strongest position (RA(B1950) = $20^{\rm h}18^{\rm m}47^{\rm s}.8$, DEC(B1950) = 40°06′42″). The position and velocity of the two clumps are consistent with those detected by Fukui & Tatematsu (1988).

All of the profiles obtained our observation were narrow, and the shock accelerated molecular gas was not detected. However, after the observation, it was found that the latest position of EGRET is different from that we used. The observation was carried out in the EGRET position of RA(B1950) = $20^{\rm h}19^{\rm m}20^{\rm s}.9$, DEC(B1950) = 40°12′21″ in Esposito et al. (1996). The latest EGRET position is RA(B1950) = $20^{\rm h}18^{\rm m}46^{\rm s}.4$, DEC(B1950) = 40°16′50″. We need to extend the map in order to conclude whether there is no shock accelerated molecular gas in γ Cygni SNR.

2.3.2 SNR W28

Figure 2.3 shows the integrated intensity map of the CO (J=3–2) emission toward SNR W28 with typical profiles at selected positions. The map represents the intensity integrated between $V_{\rm LSR} = -30$ km s^{-1} and 40 km s^{-1}. In Figures 2.8 and 2.9, the channel maps at 2 km s^{-1} velocity intervals are shown, and the velocity of the channel center is labeled at the upper right corner of each panel.

For W28, it is clear from (a1) - (a4) of Figure 2.3 that the line profile drastically changes from place to place. The line profiles of CO (J=3–2) consist of two components. One component is a narrow profile with an FWHM linewidth of $\Delta V \sim 3$ km s^{-1}

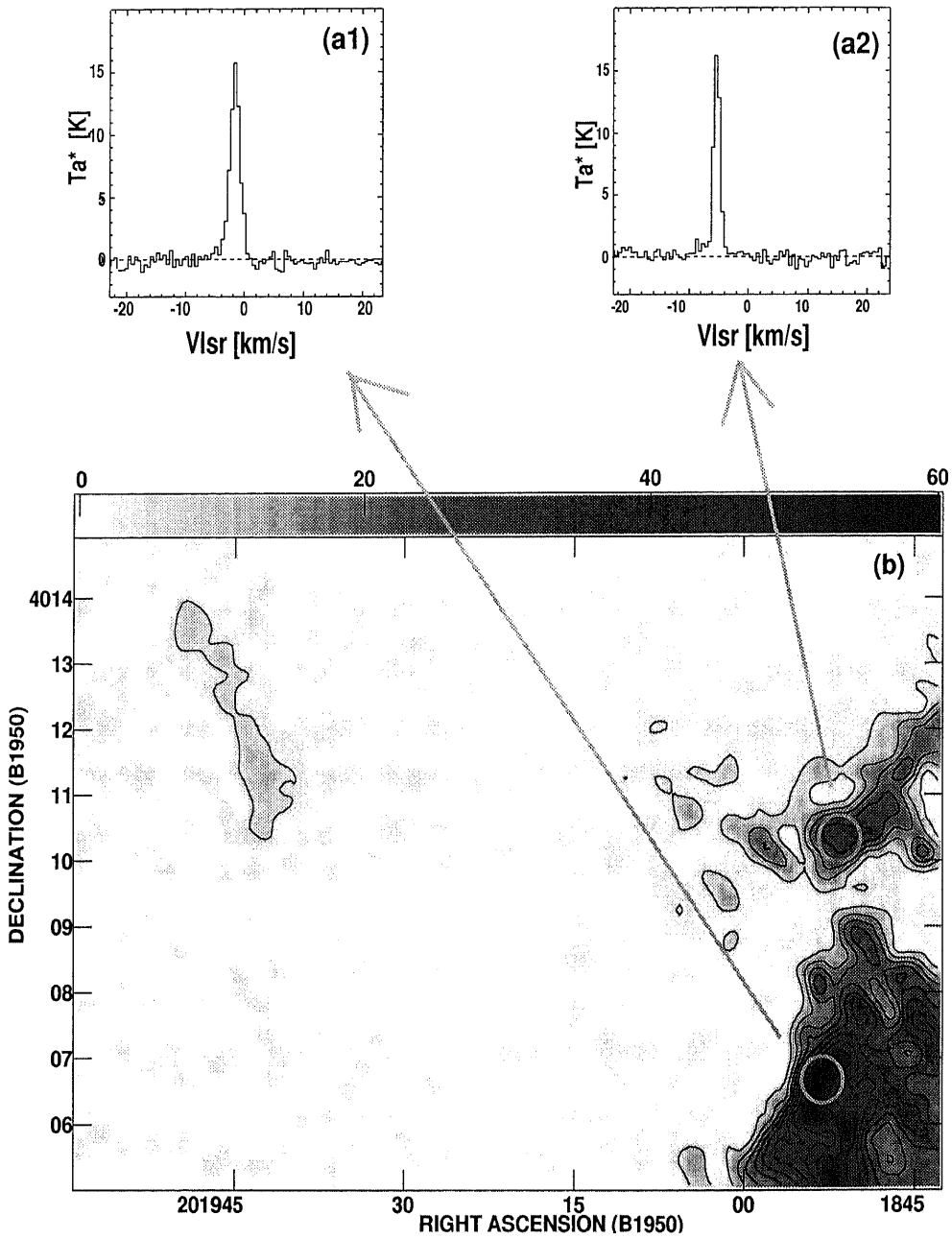

Fig. 2.2.— (a1,a2) Typical profile of the CO (J=3–2) emission toward γ Cygni SNR. The velocity scale in each spectrum runs from $V_{\rm LSR}$ = −10 km s^{-1} to 5 km s^{-1} and the temperature scale from $T_{\rm A}*$ = −3 to 20 K. (b) Integrated intensity map of the CO (J=3–2) emission at 345.796 GHz toward γ Cygni SNR. The contour interval is 6.1 K km s^{-1}. The integration range is between $V_{\rm LSR}$ = −10 km s^{-1} and 5 km s^{-1}.

at $V_{\rm LSR}$ = 7 km s^{-1} and 21 km s^{-1}. The other is a broad component with an FWHM linewidth of $\Delta V \gtrsim$ 20 km s^{-1}. The maximum linewidth of the broad component reaches 70 km s^{-1} (full width at zero intensity) at RA(B1950) = $17^{\rm h}58^{\rm m}30^{\rm s}.3$, DEC(B1950) = $-23°24'29''$. The existence of narrow and broad components has been previously reported for IC 443 (e.g., DeNoyer 1979; White et al. 1987, 1994) and 3C 391 (Wilner et al. 1998; Reach & Rho 1999). As shown in the followings, the narrow component is emission from the quiescent cloud, and the broad component is emission from "shocked gas" which is accelerated by the shock wave of SNR. There are two velocity components in the narrow emission, judging from the channel map (Figures 2.8 and 2.9) and the position–velocity (P–V) diagram (typical example of P–V diagram is shown in Figure 2.5), the 7 km s^{-1} narrow component seems to correspond to "unshocked", quiescent molecular gas associated with SNR W28. The kinematic distance corresponding to this velocity component is estimated to be 1.8 kpc by adopting a rotation curve by Clemens (1985) for a galactocentric distance of the Sun of 8.5 kpc. A distance of 1.8 kpc is consistent with a distance of 1.8 $\pm$ 1 kpc estimated for W28 from the Σ–D relation (Goudis 1976, Clark & Caswell 1976; see introduction), and is in reasonable agreement with a distance of 2.22 $\pm$ 0.16 kpc from the star counts (Armandroff & Herbst 1981). The 21 km s^{-1} narrow component is probably an unrelated cloud located along the line of sight by chance.

From the integrated intensity map ((b) of Figure 2.3), two cloud are detected. One cloud at RA(B1950) $\sim$ $17^{\rm h}58^{\rm m}30^{\rm s}$ to $17^{\rm h}59^{\rm m}10^{\rm s}$, DEC(B1950) $\sim$ $-23°30'$ to $-23°15'$ was previously observed by Wootten (1981), and we call the cloud "east cloud". The other is a filamentary cloud along DEC(B1950) $\sim$ $-23°15'$ newly discovered by our observations, we call this cloud "north cloud". Moreover, the distribution of the clouds are very similar to that of the 327 MHz radio continuum emission (the synchrotron radiation from the relativistic electron spiraling the magnetic field) from SNR W28 ((a) of Figure 2.10 ; Frail et al. 1993), and the intensity of the CO (J=3–2) emission tends to be stronger along the intense "ridge" in the radio continuum map. In the channel map (Figures 2.8 and 2.9), the distribution of 7 km s^{-1} component are also very similar to that of the radio continuum emission.

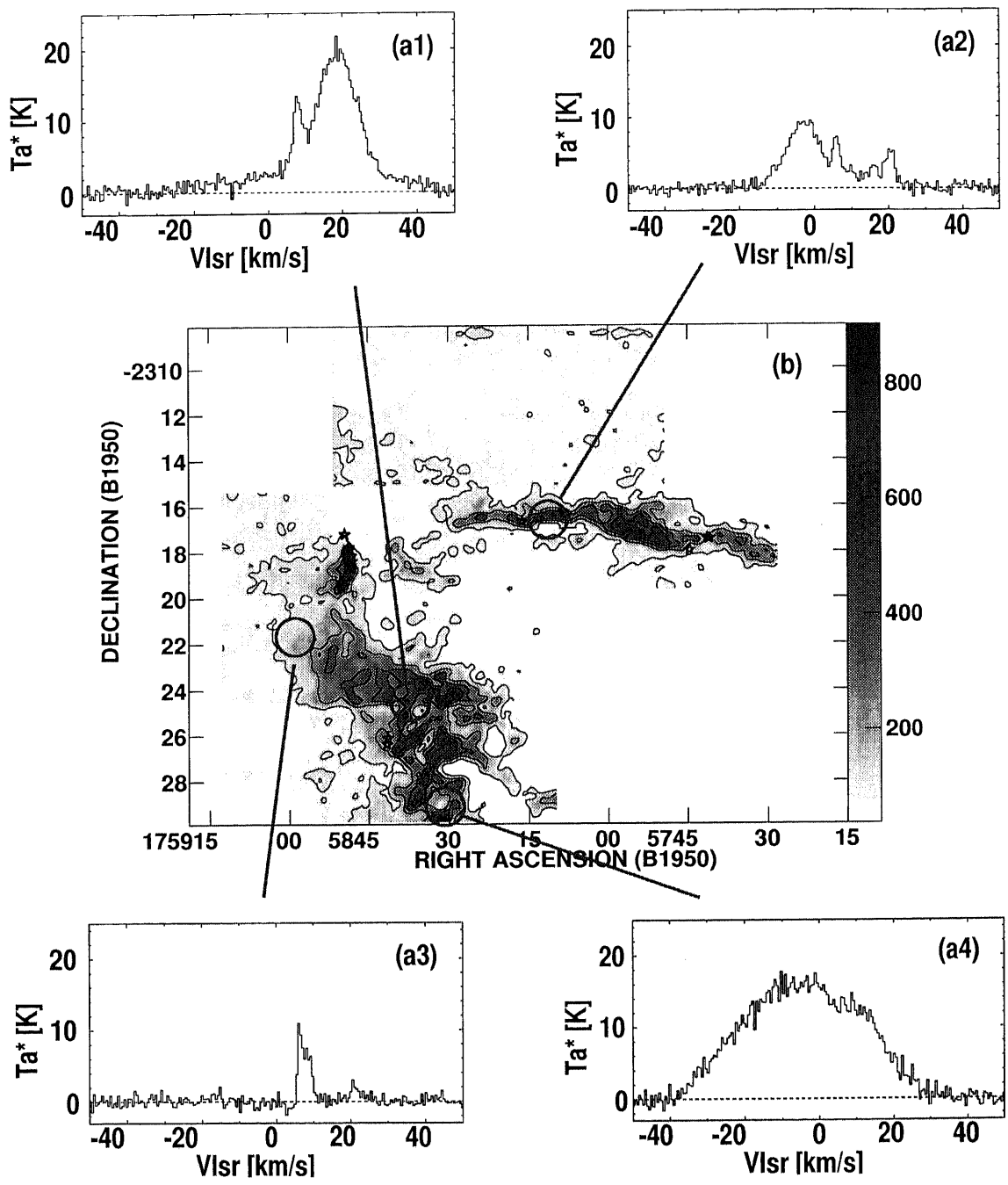

Fig. 2.3.— (a1, a2, a3, a4) Typical profile examples of the CO (J=3–2) emission toward SNR W28. The velocity scale in each spectrum runs from $V_{\rm LSR}$ = −50 km s^{-1} to 50 km s^{-1} and the temperature scale from $T_{\rm A}*$ = −3 to 25K. (b) Integrated intensity map of the CO (J=3–2) emission toward SNR W28. The integration was made between $V_{\rm LSR}$ = −30 km s^{-1} and 40 km s^{-1}. The contour interval is 154 K km s^{-1} starting from 97 K km s^{-1}.

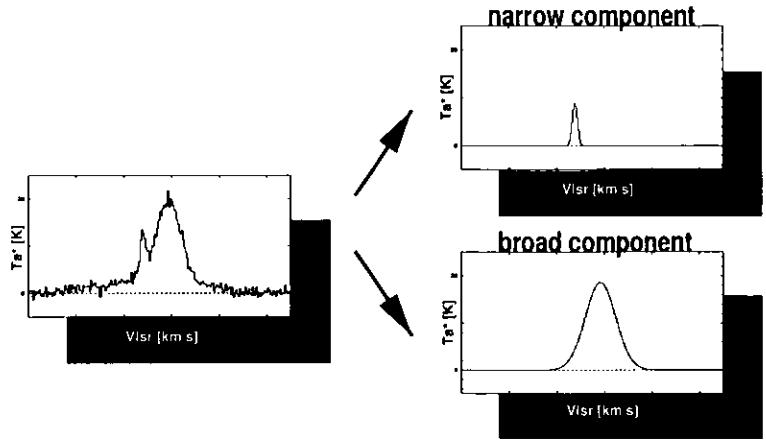

Fig. 2.4.— Example of *Gaussian* fit. The narrow component ($\Delta V \sim 2-3$ km s^{-1}) at $V_{\rm LSR} = 7$ km s^{-1} and the broad component ($\Delta V \geq 20$ km s^{-1}) are fit to two *Gaussians*.

2.4 Discussion

In the following, only SNR W28, in which broad emission (the shock accelerated gas) was detected, is discussed.

First, we investigate the detailed distribution of the unshocked and shocked gas. We fitted multiple *Gaussians* to the observed spectrum as Figure 2.4. The result is shown in Figure 2.10. (a) is the 327 MHz radio continuum (Frail et al. 1993). The red oval represents the EGRET error circle (Esposito et al. 1996). In (b) of Figure 2.10, the blue contours represent the distribution of the unshocked gas, and the red contours represent that of the shocked gas. The shocked and unshocked gas clearly show different spatial distributions. The central position of the supernova explosion is RA(B1950) = $17^{\rm h}57^{\rm m}31^{\rm s}.0$, DEC(B1950) = $-23°12'$. The unshocked gas is displaced by $50''$ – $100''$ outward from the SNR center with respect to the shocked gas. At a distance of 1.8 kpc, the displacement corresponds to 0.4 – 1.0 pc. The width of the filamentary shock gas is typically 0.5 pc. The displacement of the unshocked and shocked gas is clearly shown for the interaction of SNR with the molecular cloud for the first time. Figure 2.5 shows a position-velocity (P–V) diagram of the CO (J=3–2) emission from the molecular cloud near SNR W28 along RA(B1950) = $17^{\rm h}58^{\rm m}08^{\rm s}.2$. It

is clear that the shock front is located at DEC(B1950) = $-23°16'15''$. A feature with a linewidth of $\Delta V \sim 30$ km s^{-1} at DEC(B1950) = $-23°16'30''$ is the shocked gas, and the filamentary clump perpendicular to the broad emission at $V_{\rm LSR} = 7$ km s^{-1} in the north side is the unshocked gas. The shock wave from SNR is expanding upward in the figure. The 21 km s^{-1} component seems to be an unrelated cloud along the line of sight.

It is known that the OH (1720 MHz) maser can be pumped due to the interaction of the SNR with the molecular cloud (Frail et al. 1994; Green et al. 1997; Claussen et al. 1997). In SNR W28, Frail et al. (1994) detected 26 OH (1720 MHz) maser spots, and Claussen et al. (1997) detected 41 spots. The green filled circles in Figure 2.10 mark 41 OH (1720 MHz) maser detected by Claussen et al. (1997), and the white cross in Figure 2.5 marks one of the OH (1720 MHz) maser spots in the P–V diagram. It is clear that all of the OH (1720 MHz) maser spots are located along the edge of the shocked gas, or at the boundary between the narrow component and the broad component in the P–V diagram. This suggests that the OH (1720 MHz) maser spots are located in the shock front. Moreover, it is also clear that the velocity of the OH (1720 MHz) maser is close to that of the narrow component (the unshocked gas). The OH (1720 MHz) maser can be collisionally pumped in a warm (50 K $\lesssim T_{\rm k} \lesssim$ 125 K), dense ($n({\rm H_2}) \sim 10^3$ cm^{-3}) gas (Lockett 1999). Together with the OH (1720 MHz) maser data, our observation clearly showed that there exists warm and dense gas shocked by SNR W28. It is found that the SNR W28 is one of the objects which unambiguously interact with the molecular cloud.

We found that the interaction of the SNR with the molecular cloud takes place within the EGRET error circle as shown in Figure 2.10. Our observations support a hypothesis that the interaction between supernova remnant and the molecular cloud can be the origin of gamma-rays (Pollock 1985, Sturner & Dermer 1995, and Esposito et al. 1996). The charged particle (the cosmic-ray) accelerated by shock wave of SNR collides with the target particle (H and He) in the molecular cloud, and resultant pions decay to gamma-rays. Another possibility is that gamma-ray is emitted as relativistic bremsstrahlung emission.

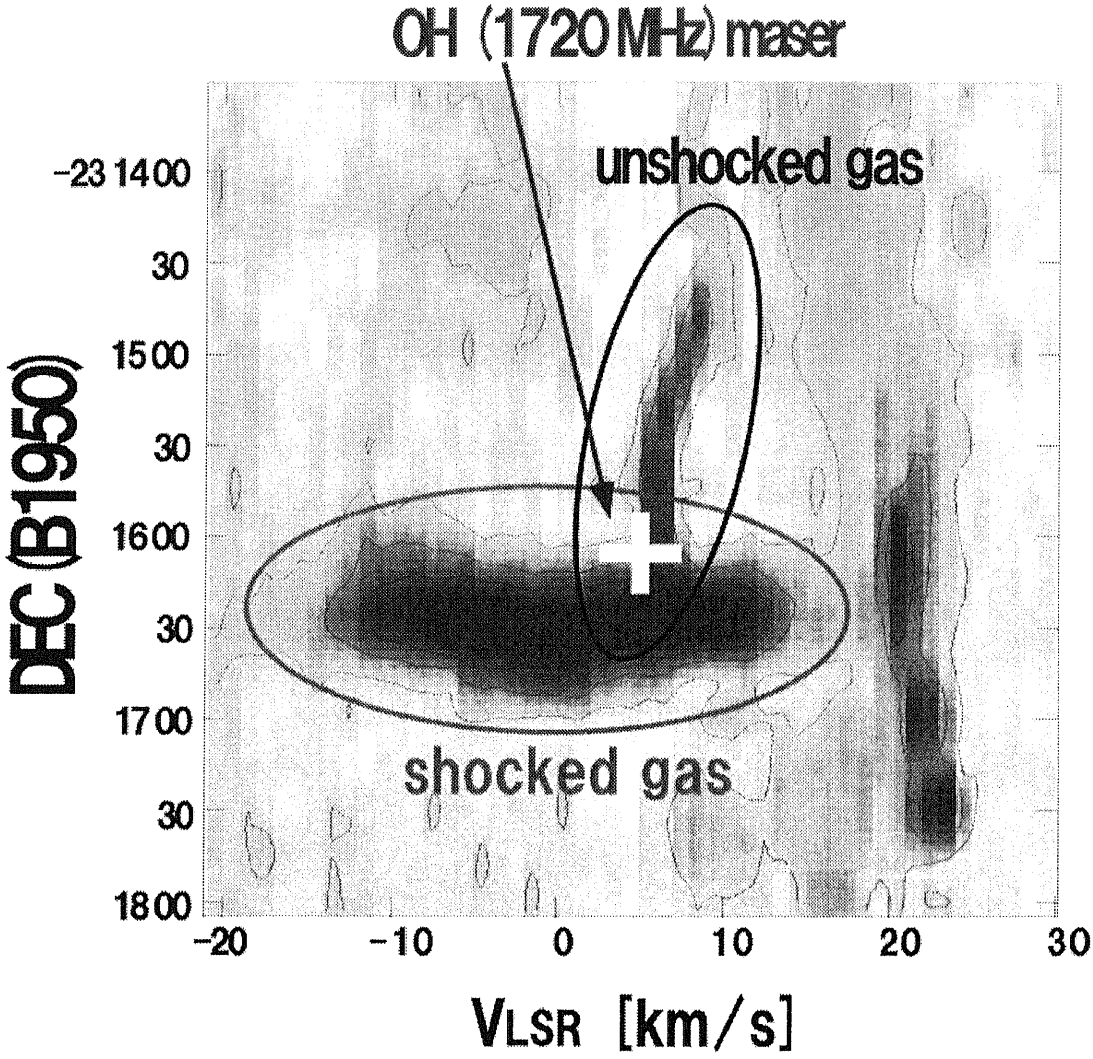

Fig. 2.5.— Position–velocity (P–V) diagram of the CO (J=3–2) emission from the molecular cloud near SNR W28 along RA(B1950) = $17^{h}58^{m}08^{s}.2$. The contour interval is 2.6 K. The white cross marks the OH (1720 MHz) maser observed by Claussen et al. (1997). A feature with a linewidth of $\Delta V \sim 30$ km s^{-1}, which is located at DEC(B1950) = $-23°16'30''$ corresponds to the shocked gas. The filamentary feature perpendicular to the broad emission at $V_{\rm LSR} = 7$ km s^{-1} in the north–side is shown the unshocked gas. From this figure, it is clear that the shock front is located at DEC(B1950) = $-23°16'15''$ and the OH (1720 MHz) maser spot is located at the shock front. The velocity of the OH (1720 MHz) maser is close to that of unshocked gas.

2.5 Conclusion

We observed SNR W28 and γ Cygni SNR, which are EGRET gamma–ray sources, in submillimeter–wave CO (J=3–2) emission. The shocked molecular gas was clearly detected in SNR W28, but not in γ Cygni SNR. For SNR W28, the shocked gas is filamentary, and surrounds the center of the supernova explosion. The unshocked gas is displaced by 0.4 – 1.0 pc outward with respect to the shocked gas. The spatial relationship between the shocked and unshocked gas has been clarified for the first time for the interaction between SNR and the molecular cloud. The shocked molecular gas is located in the EGRET error circle, and our observations are consistent with a hypothesis that the interaction of the SNR with the molecular cloud can be the origin of gamma–rays. The structure of the shock region is rather simple and "edge–on".

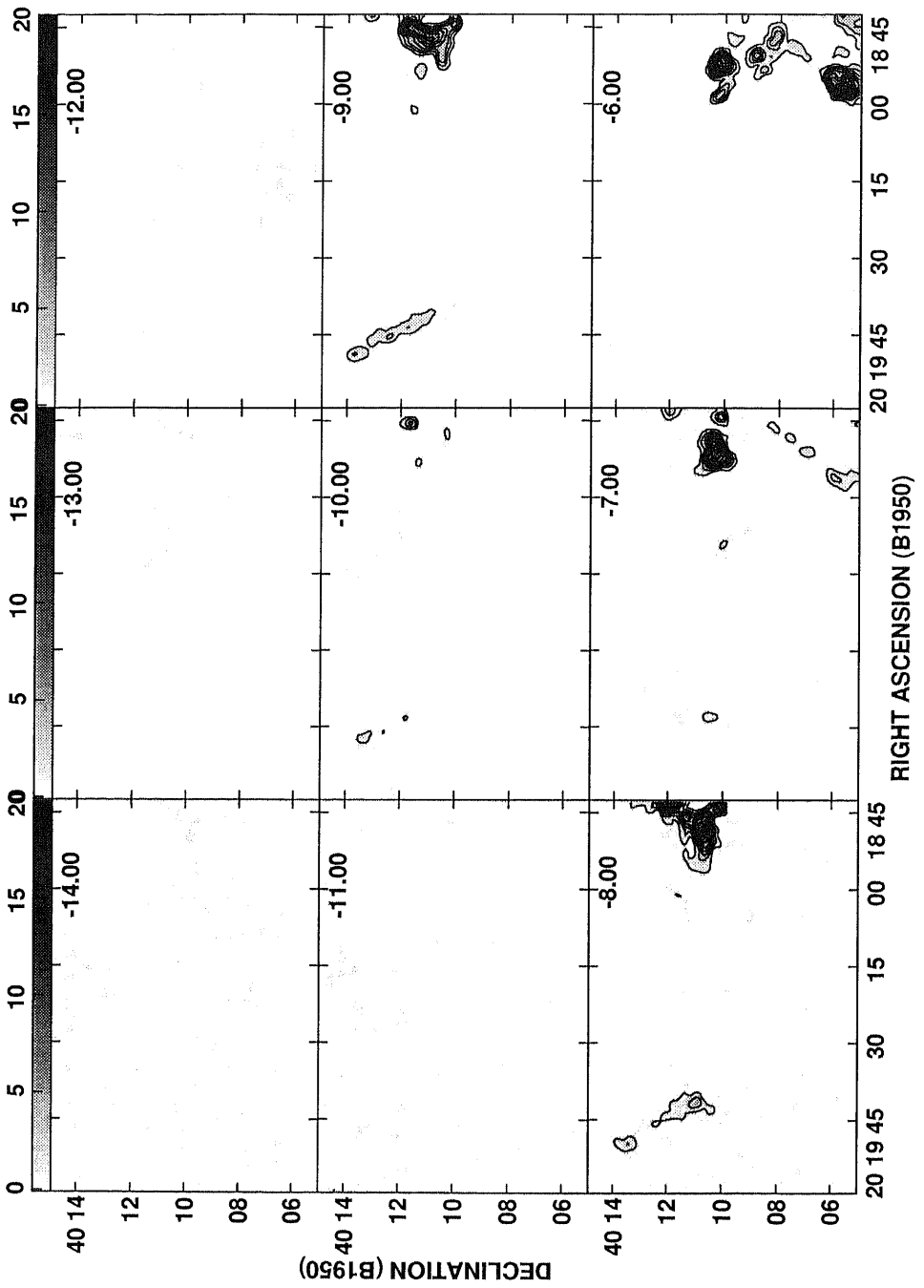

Fig. 2.6.— Part I of the channel maps of the integrated CO (J=3–2) emission at 2 km s^{-1} velocity intervals toward γ Cygni SNR. The center velocity is labeled at the upper right corner. The contour interval is 2.9 K km s^{-1} starting from 1.47 K km s^{-1}.

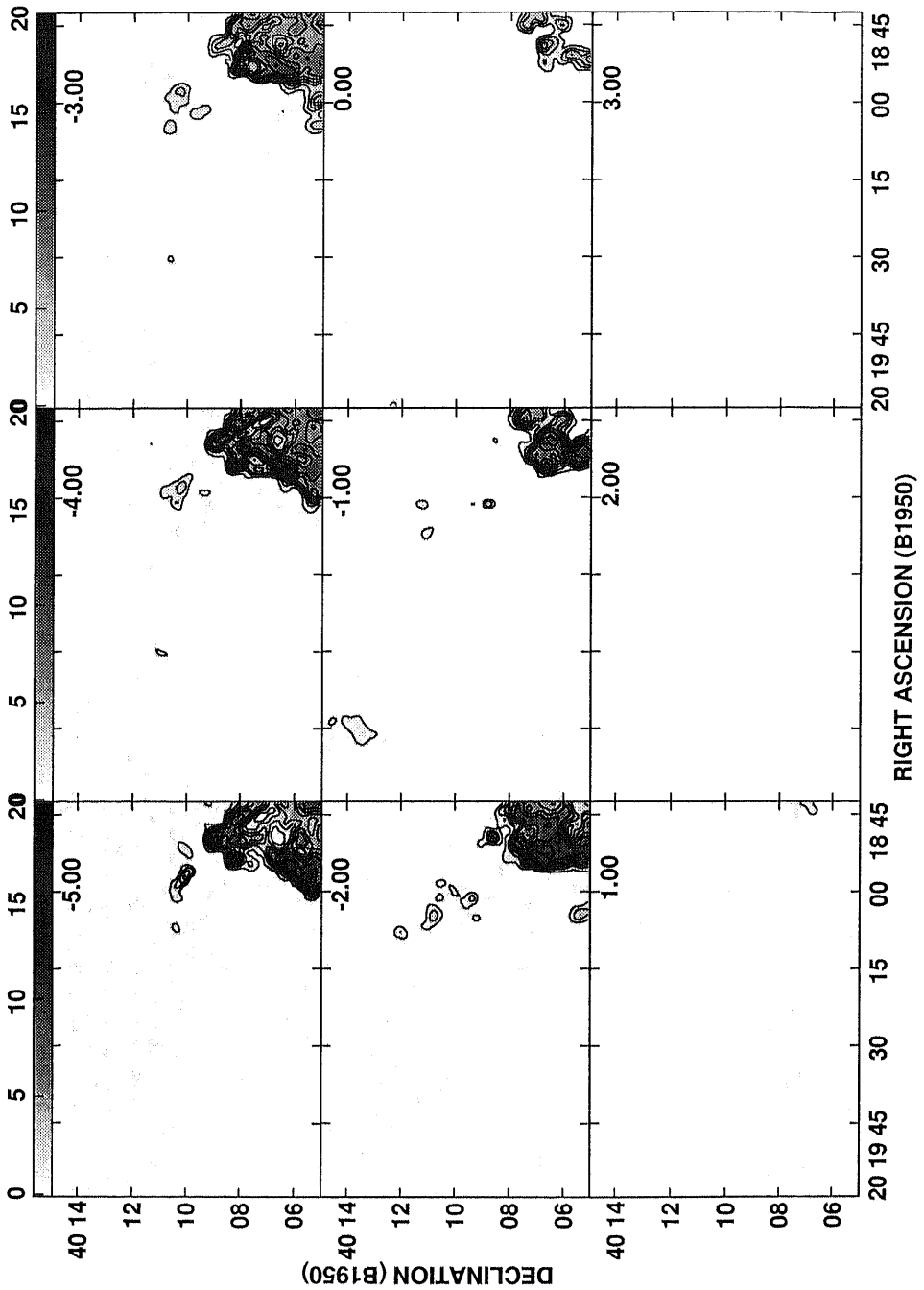

Fig. 2.7.— Part II of the channel maps of the integrated CO (J=3–2) emission toward γ Cygni SNR.

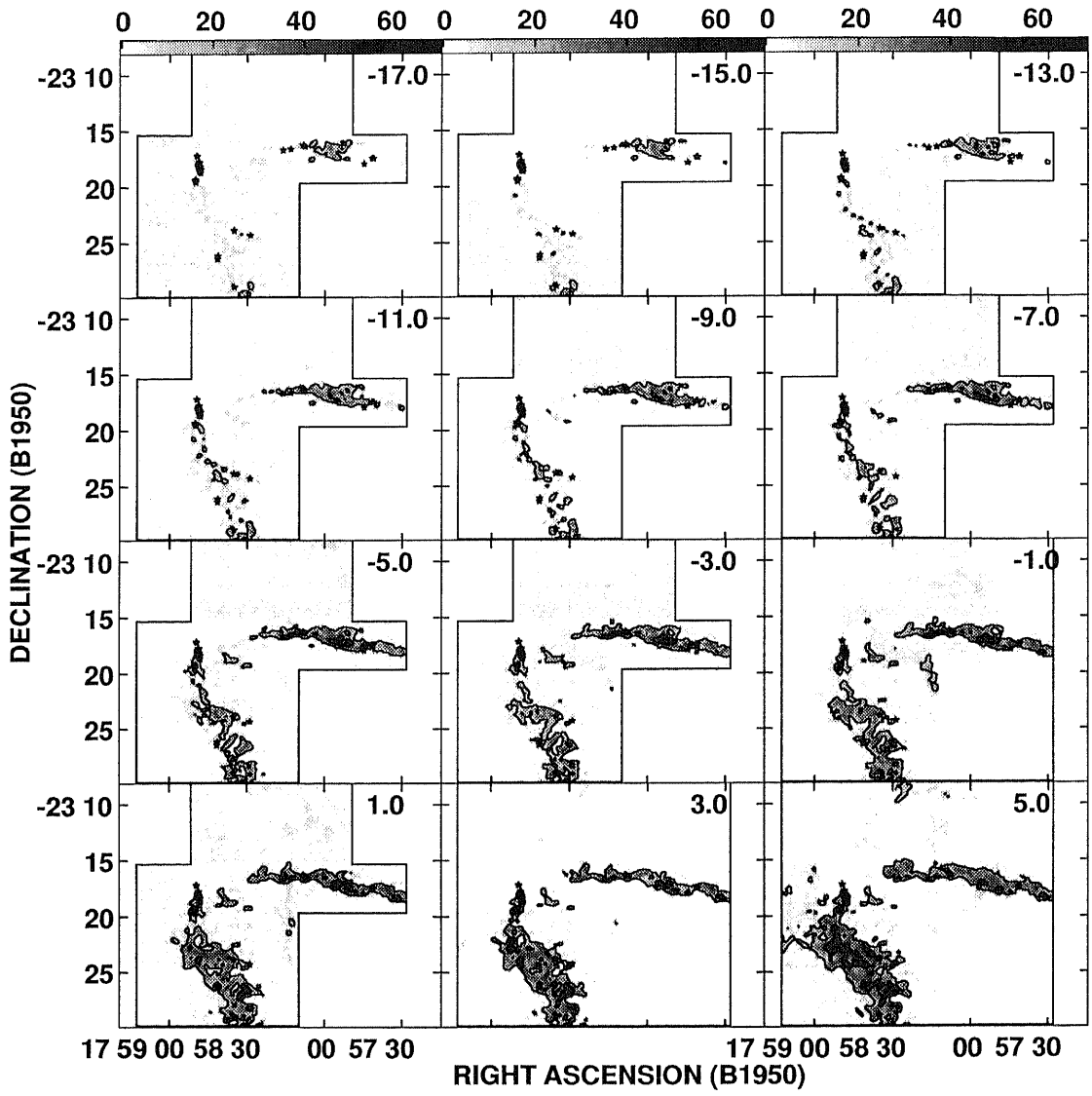

Fig. 2.8.— Part I of the channel maps of the integrated CO (J=3–2) emission at 2 km s^{-1} velocity intervals toward SNR W28. The center velocity is labeled at the upper right corner. The contour interval is 30.48 K km s^{-1} starting from 10.67 K km s^{-1}.

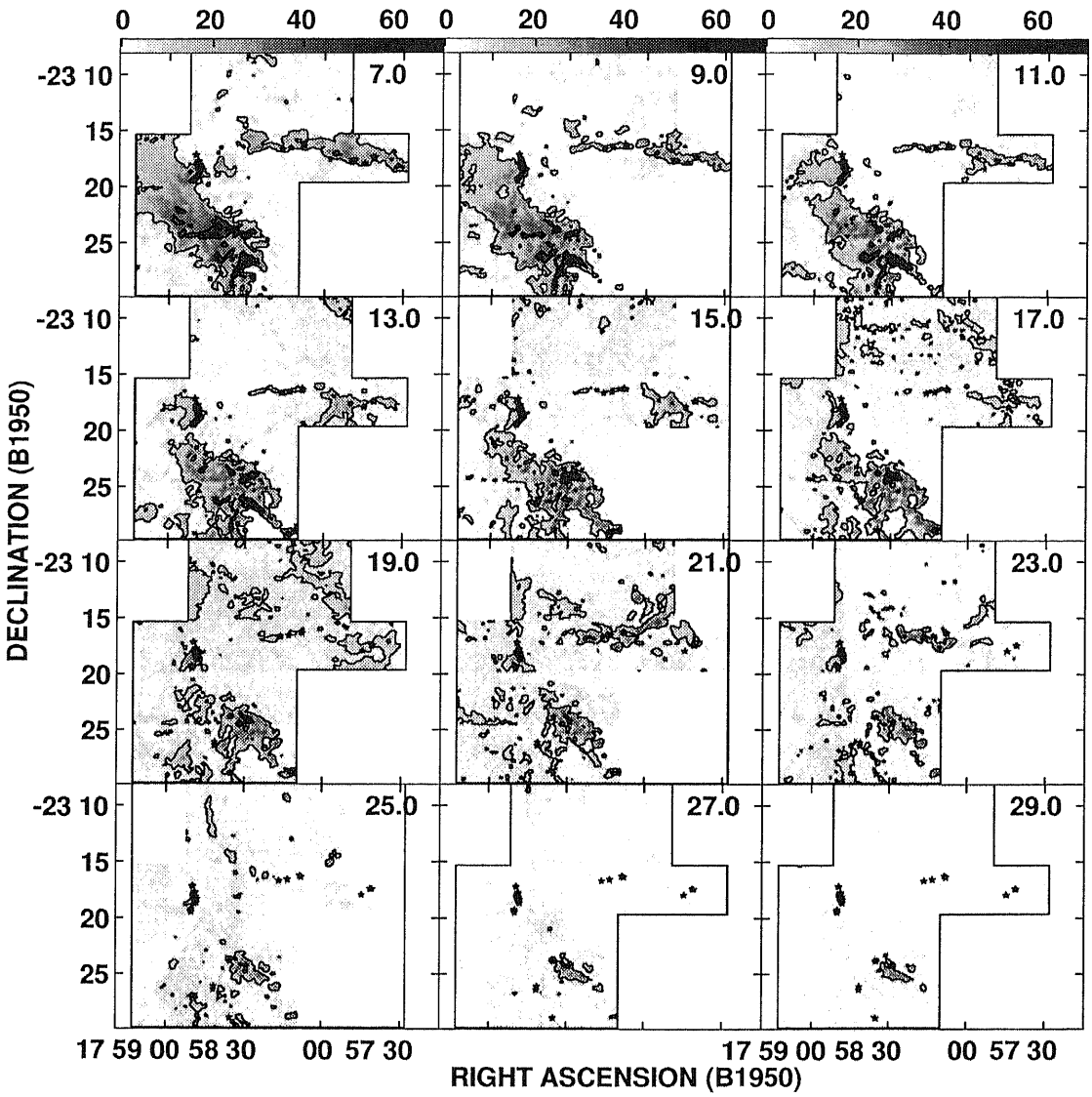

Fig. 2.9.— Part II of the channel maps of the integrated CO (J=3–2) emission toward SNR W28.

References

Arikawa, Y., Tatematsu, K., Sekimoto, Y., Takahashi, T. 1999, PASJ, 51, L7

Armandroff, T.E. & Herbst, W. 1981, A&A, 86, 1923

Clark, D.H. & Caswell, J.L. 1976, MNRAS, 174, 267

Claussen, M.J., Frail, D.A., Goss, W.M., Gaume, R.A. 1997, ApJ, 489, 143

Clemens, D.P. 1985, ApJ, 295, 422

DeNoyer, L.K. 1979, ApJ, 232, L165

DeNoyer, L.K. 1983, ApJ, 264, 141

Esposito, J.A., Hunter, S.D., Kanbach, G., Sreekumar, P. 1996, ApJ, 461, 820

Frail, D.A., Kulkarni, S.R., Vasisht, G. 1993, Nature, 365, 136

Frail, D.A., Goss, W.M., Slysh, V.I. 1994, ApJ, 424, L111

Frail, D.A., Goss, W.M., Reynoso, ,E.M., Giacani, E.B., Green, A.J., Otrupcek, R. 1996, AJ, 111, 1651

Fukui, Y., Tatematsu, K. 1988, in IAU Colloquium 101, Supernova Remnants and Interstellar Medium, ed R.S. Roger, T.L. Landecker (Cambridge University Press, Cambidge) p261

Goudis, C. 1976, Ap&SS, 40, 91

Green, A.J., Frail, D.A., Goss, W.M., Otrupcek, R. 1997, AJ, 114, 2058

Green, D.A. 1998, A Catalogue of Galactic Supernova Remnants (1998 September version) (Mullard Radio Astronomy Observatory, Cambridge)

Higgs, L.A., Landecker, T.L. & Roger, R.S. 1977, AJ, 82, 718

Lockett, P., Gautheir, E., Elitzur, M. 1999, ApJ, 511, 235

Lozinskaya, T.A, 1974, SvA, 17, 449

Lozinskaya, T.A. 1981, SvAL, 7, 17

Ladecker, T., Roger, R., & Higgs, L., 1980, A&AS, 39, 133

Pollock, A.M.T. 1985, A&A, 150, 339

Reach, W.T. & Rho, J. 1999, ApJ, 511, 836

Sturner, S.J. & Dermer, C.D. 1995, A&A, 293, L17

Tatematsu, K., Nakano, M., Yoshida, A., Wiramihardja, S.D., Kogure, T. 1985, PASJ, 37, 345

Tatematsu, K., Fukui, Y., Nakano, M., Kogure, T., Ogawa, H., Kawabata, K. 1987, A&A, 184, 279

Tatematsu, K., Fukui, Y., Iwata, T., Seward, F.D., Nakano, M. 1990a, ApJ, 351, 157

Tatematsu, K., Fukui, Y., Landecker, T.L., Roger, R.S. 1990b, A&A, 237, 189

White, G.J., Rainey, R., Hayashi, S.S., Kaifu, N. 1987, A&A, 173, 337

White, G.J. 1994, A&A 283, L25

Wilner, D.J., Reynolds, S.P., Moffett, D.A. 1998, AJ, 115, 247

Wootten, H.A. 1981, ApJ, 245, 105

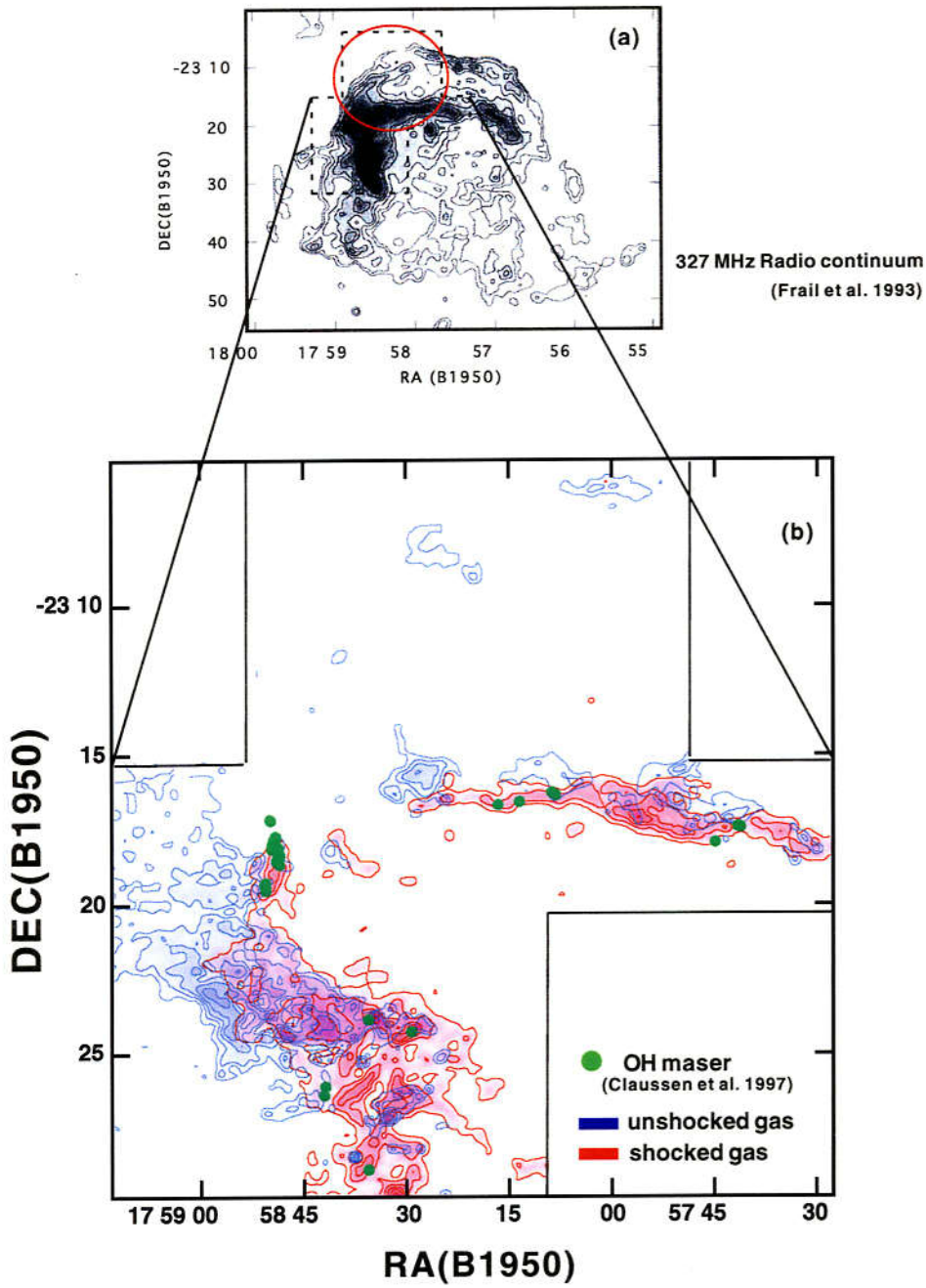

Fig. 2.10.— (a) Radio continuum map of the SNR W28 at 327 MHz reproduced from Frail et al. (1993). The red oval is the EGRET error circle (Esposito et al. 1996). The dashed line represents the boundary of the observed region. (b) The integrated intensity map of the CO (J=3–2) emission near the SNR W28. The blue contour and halftone map represents the distribution of the unshocked gas ($V_{\rm LSR}$ = 4 km s^{-1} to 9 km s^{-1}), and the red contour and halftone map represents that of the shocked gas ($V_{\rm LSR}$ = -40 km s^{-1} to 40 km s^{-1}). The contour interval is 20.7 K km s^{-1} and 129.3 K km s^{-1} levels for unshocked gas and shocked gas, respectively. The green filled circles are the OH (1720 MHz) maser spots by Claussen et al. (1997).

Chapter 3

CO (J=1–0) observations toward SNR W28

Abstract

We observed SNR W28 in millimeter-wave CO (J=1–0) line (115 GHz ; 2.6 mm) in order to obtain the distribution of the cold gas and to estimate the physical properties of the molecular gas by using the 45 m *Nobeyama Radio Observatory* (NRO). The distribution of CO (J=1–0) globally resembles that of CO (J=3–2). It is found that the line intensity of CO (J=1–0) emission is stronger than that of CO (J=3–2) emission in the narrow component, while the CO (J=3–2) emission is stronger than CO (J=1–0) emission in the broad component. From calculations of large velocity gradient (LVG) models, the kinetic temperature is $T_{\rm kin} \lesssim 20$ K, and the density is $n({\rm H_2}) \lesssim 10^3$ cm^{-3} for the narrow component, while $T_{\rm kin} \gtrsim 60$ K, $n({\rm H_2}) \gtrsim 10^4$ cm^{-3} for the broad component. The narrow component seems to be emitted from ambient gas ("the unshocked gas"), and the broad component seems to be emitted from the warm, dense gas ("the shocked gas"). The total mass of the unshocked gas is estimated to be $M_{\rm unshocked} = 4 \times 10^3\ M_\odot$, and that of the shocked gas is $M_{\rm shocked} = 2 \times 10^3\ M_\odot$. This means that about 30 % (in mass) of the molecular cloud has been shock-accelerated by the SNR (here we ignored dissociated CO). The total kinetic energy deposited in the shocked molecular gas is 3×10^{48} erg, which is corresponds 0.3 % of the energy of the supernova explosion.

3.1 Introduction

As described in Chapter 2, we observed the molecular cloud toward SNR W28 in high-resolution submillimeter-wave CO (J=3–2) line (345 GHz ; 0.9 mm), and successfully detected the unshocked and shocked gas, which suggest the interaction of SNR with the molecular cloud. The distribution of the unshocked and shocked gas is clearly resolved. The shocked gas is filamentary, and surrounds the center of the supernova explosion. The unshocked gas is displaced by 0.4 – 1.0 pc outward with respect to the shocked gas. The spatial relationship between shocked and unshocked gas has been clarified for the first time for the interaction between SNR and the molecular clouds. In this chapter, we discuss the detailed physical parameters (temperature, density, mass, and energy) of the molecular cloud which accompanies SNR W28.

To estimate the physical parameters, we observed the millimeter-wave CO (J=1–0) line, whose energy level differs from submillimeter-wave CO (J=3–2) line. By observing multiple molecular transitions of the same molecule, the physical parameters are deduced from the model calculation of the excitation (the large velocity gradient (LVG) model). Seta et al. (1998) observed in CO (J=2–1) emission toward the molecular cloud toward SNR W44 by using the University of Tokyo-Nobeyama 60 cm Survey Telescope (VST1), and found that the CO (J=2–1) / CO (J=1–0) line intensity ratio is high in the broad component (wing emission) due to the interaction of SNR W44 with the giant molecular cloud (GMC). The estimated kinetic temperature is $T_{\rm kin} \sim 40 - 80$ K, and the density is $n({\rm H_2}) \gtrsim 10^3$ cm^{-3}. For IC 443, van Dishoeck et al. (1993) derived from the the CO (J=3–2) and CO (J=2–1) data the kinetic temperature to be $T_{\rm kin} \sim 10 - 20$ K, and the density to be $n({\rm H_2}) \sim 3 \times 10^3 - 10^4$ cm^{-3} in the quiescent preshocked gas. The shocked gas has at least two components : lower density component ($T_{\rm kin} \sim 80$ K and $n({\rm H_2}) \sim 10^5$ cm^{-3}) and higher density component ($T_{\rm kin} \sim 200$ K and $n({\rm H_2}) \sim 3 \times 10^6$ cm^{-3}).

3.2 Observations

The CO (J=1–0) data at millimeter-wave (f=115.217 GHz, λ= 2.6mm) were obtained using the 45 m telescope of the Nobeyama Radio Observatory (NRO) in 1998

TABLE 3.1

Parameters of the observed CO line

line	CO (J=3–2)	CO (J=1–0)
Wave-length	0.9 mm (submillimeter-wave)	2.6 mm (millimeter-wave)
Frequency	345.796 GHz	115.217GHz
Telescope	JCMT 15 m[a]	NRO 45 m[b]
Site	Mauna Kea, Hawaii	Nobeyama, Japan
Elevation	4092 m	1350 m
Beam size	13 arcsec	15 arcsec
Date	1997 July	1998 March and April

Note.— [a] http://www.jach.hawaii.edu/JACpublic/JCMT

[b] http://www.nro.nao.ac.jp

March and April. The telescope has a beam size of $\sim$ 15″, which is close to the beam size ($\sim$ 13″) of 15 m JCMT telescope. We can estimate the physical parameters rather accurately by using telescopes with similar beam sizes. The main-beam efficiency is $\eta_{\rm mb} \sim 46$ %. We used the 4-element focal-plane SIS receiver with a beam separation of 34″ (Sunada et al. 1995). The grid spacing were 34″. The mapping data of CO (J=3–2) and CO (J=1–0) data is convolved to 48″, when we compare CO (J=1–0) data with CO (J=3–2) data. The SSB system noise temperature was 300 – 400 K. The 2048 channel acousto-optical spectrometers (AOSs) with a spectral resolution of 40 kHz (0.1 km s^{-1}) were used as the receiver backend. The total integration time was typically 40 s per each position. Observations were made in the position-switching mode. The telescope pointing was checked every 90 to 120 min by observing the SiO maser emission from VX Sgr. We calibrated the data using the standard chopper-wheel method. The map reference center is the EGRET position of RA(B1950) = $17^{\rm h}58^{\rm m}20^{\rm s}.28$, DEC(B1950) = $-23°12'28''.98$ (Esposito et al. 1996), and the observed region is $25' \times 25'$, which covers the observed region (Figure 2.1) in CO (J=3–2) emission. In this chapter, we report the line intensity in terms of the

main-beam brightness temperature $T_{\rm mb} = T_{\rm A}^*/\eta_{\rm mb}$ (Kutner & Ulich 1981), when we compare the CO (J=1–0) data with the CO (J=3–2) data in a consistent manner. Otherwise, the intensity is reported in terms of $T_{\rm A}*$. The parameters of the JCMT 15 m telescope and the NRO 45 m telescope are summarized in Table 3.1.

3.3 Results

Figure 3.1 shows the integrated intensity map of the CO (J=1–0) emission toward SNR W28 with typical profiles at selected positions. The integration was made between $V_{\rm LSR}$ = −30 km s^{-1} and 40 km s^{-1}. In Figures 3.8 and 3.9, the channel maps at 2 km s^{-1} velocity intervals are shown, and the channel center velocity is labeled at the upper right corner of each panel. In order to compare with the CO (J=3–2) emission, the integrated intensity map of CO (J=1–0) and CO (J=3–2) emission convolved to 48″ resolution are shown in Figures 3.2 and 3.3, respectively. The convolved channel maps are shown in Figures 3.10 through 3.13. Figure 3.4 shows the CO (J=3–2) / CO (J=1–0) integrated intensity ratio map, and the contour interval is 0.2. Figures 3.14 and 3.15 show the channel maps of the CO (J=3–2) / CO (J=1–0) integrated intensity ratio.

The distribution of CO (J=1–0) is globally similar to that of CO (J=3–2) and that of the radio continuum (synchrotron emission). However, close inspection shows that the distribution of CO (J=1–0) seems to slightly offsetted outward to the north-east from the center of supernova explosion. From the ratio map, it is clear that the inner (close to the supernova explosion) part of the filament has a higher ratio than the outer part. Moreover, the filament structure is less remarkable in CO (J=1–0) map than in CO (J=3–2) map.

It is clear from Figure 3.1 that the CO (J=1–0) line profile drastically changes from place to place as well as CO (J=3–2) emission. The line profile of CO (J=1–0) also consists of the narrow and broad components. Figure 3.5 shows typical examples of the obtained CO (J=1–0) and CO (J=3–2) spectra obtained towards four positions in W28 SNR. In (a), the broad emission is observed a blue-shifted wing emission with respect to the unshocked gas at $\sim$ 7 km s^{-1}. In (c), we see red-shifted wing emission. In (b) and (d), the wing emission extends on both sides. It is clear that the intensity of the

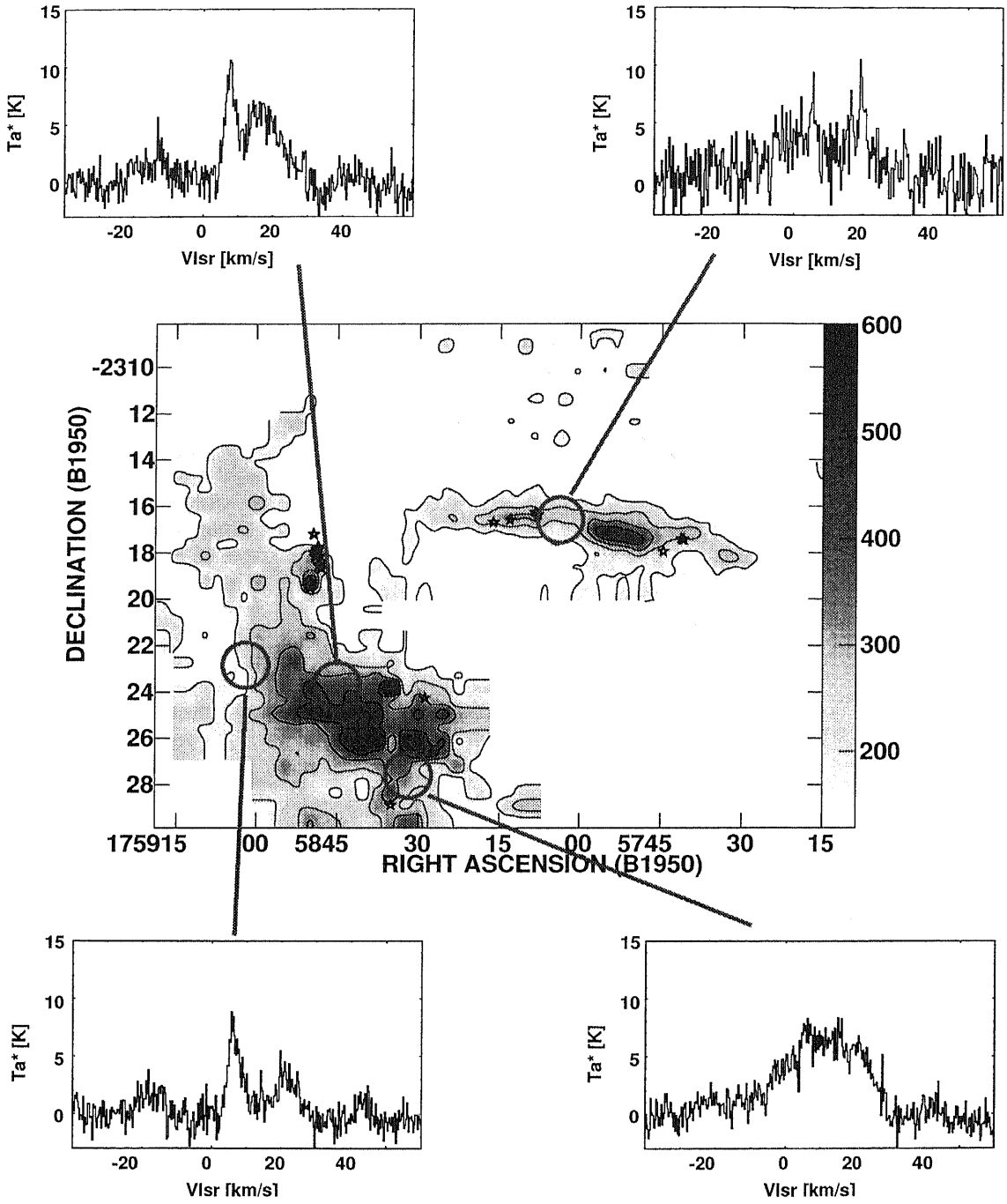

Fig. 3.1.— Typical profile examples of the CO (J=1–0) emission toward SNR W28. The velocity scale in each spectrum runs from $V_{\rm LSR}$ = −40 km s^{-1} to 60 km s^{-1} and the temperature scale from T_A* = −3 to 15 K. Center: Integrated intensity map of the CO (J=1–0) emission toward SNR W28. The integration was made between $V_{\rm LSR}$ = −30 km s^{-1} and 40 km s^{-1}. The contour interval is 85 K km s^{-1}.

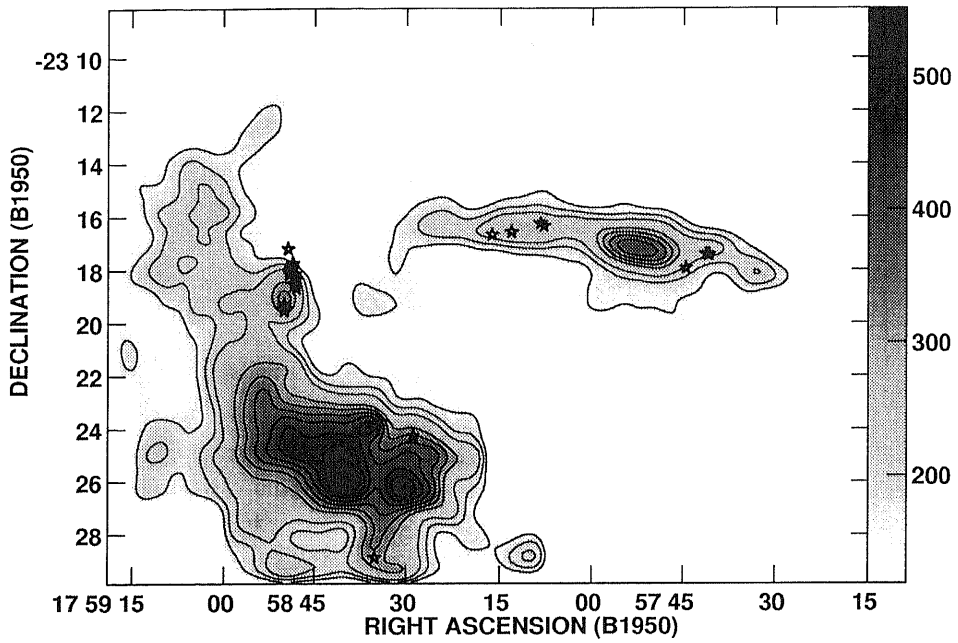

Fig. 3.2.— Integrated intensity map of the CO (J=1–0) emission. The integration was made between $V_{\rm LSR}$ = −30 km s^{-1} and 40 km s^{-1}. The contour interval is 32.8 K km s^{-1} starting from 164 K km s^{-1}. The resolution of CO (J=1–0) and CO (J=3–2) is made equal to 48″.

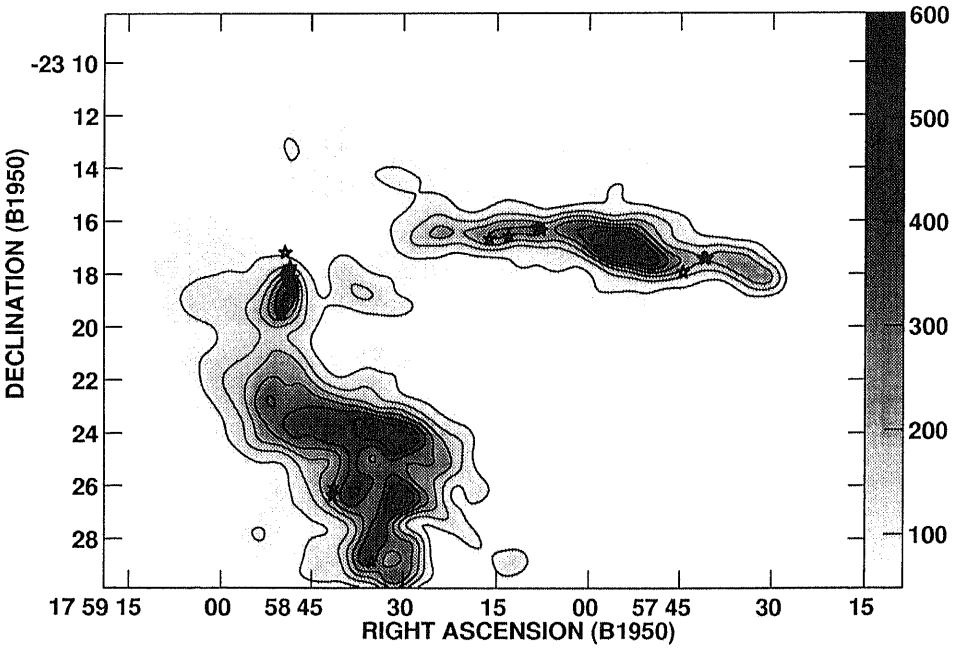

Fig. 3.3.— Integrated intensity map of the CO (J=3–2) emission. The integration was made between $V_{\rm LSR}$ = −30 km s^{-1} and 40 km s^{-1}. The contour interval is 64.4 K km s^{-1} starting from 92 K km s^{-1}. The resolution of CO (J=1–0) and CO (J=3–2) is made equal to 48″.

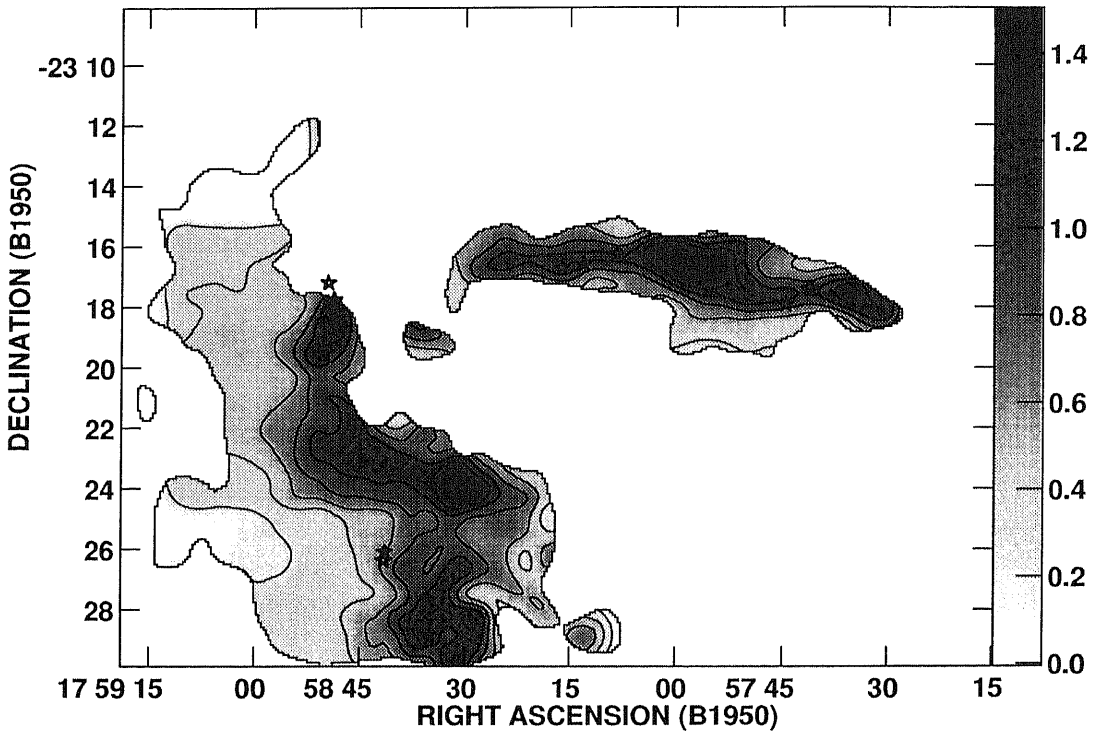

Fig. 3.4.— CO (J=3–2)/ CO (J=1–0) integrated intensity ratio map toward W28. The contour interval is 0.2. The stars mark the OH (1720 MHz) maser spots by Claussen et al. (1997)

broad components is stronger in CO (J=3–2) than in CO (J=1–0), while the intensity of the narrow components at $V_{\rm LSR}$ = 7 km s^{-1} tends to be stronger in CO (J=1–0) than in CO (J=3–2).

It is Figures 3.14 and 3.15 clearly show that the ratio is high in the wing component. In order to examine the CO (J=3–2) / CO (J=1–0) line peak intensity ratio of the narrow and broad components, the data were randomly chosen in several positions of observed region. The CO (J=3–2) / CO (J=1–0) line peak intensity ratio is 0.4 – 0.7 in the narrow component of $V_{\rm LSR}$ = 7 km s^{-1} from the unshocked gas, while the ratio is 2.3 – 2.8 in the broad component from the shocked gas. This might suggest that the shocked gas is warmer and denser than the unshocked gas.

3.4 Analyses

3.4.1 Temperature and density

From the observed line intensities, we estimate the density and kinetic temperature of the molecular cloud associated with SNR W28. The CO (J=3–2) / CO (J=1–0) line peak intensity ratio is 0.4 – 0.7 in the narrow components, while 2.3 – 2.8 in the broad components. We ran large–velocity gradient (LVG) models (Goldreich & Kwan 1974; Scoville & Solomon 1974) to constrain the physical condition by using line peak intensity ratio. In this model, it is approximated that the molecular cloud has the velocity gradient, and that the radiated photon will be observed without absorption in the different place, because different portion along the line of sight has different radial velocity. The method of the excitation calculation is explained in Appendix C. We assume the collision partner of CO is only the hydrogen molecule (H_2), and rate coefficients are taken from Flower et al. (1985). Figure 3.6 shows the intensity ratio of CO (J=3–2) to CO (J=1–0) (solid lines) and the line intensity of CO (J=3–2) line (broken lines) as a function of CO fractional abundance per unit velocity gradient and molecular hydrogen density for fixed values of the kinetic temperature. Figure 3.7 show the intensity ratio of CO (J=3–2) to CO (J=1–0) (solid lines) and the line intensity of CO (J=3–2) line (broken lines) as a function of kinetic temperature and molecular hydrogen density for fixed values of the CO fractional abundance per unit

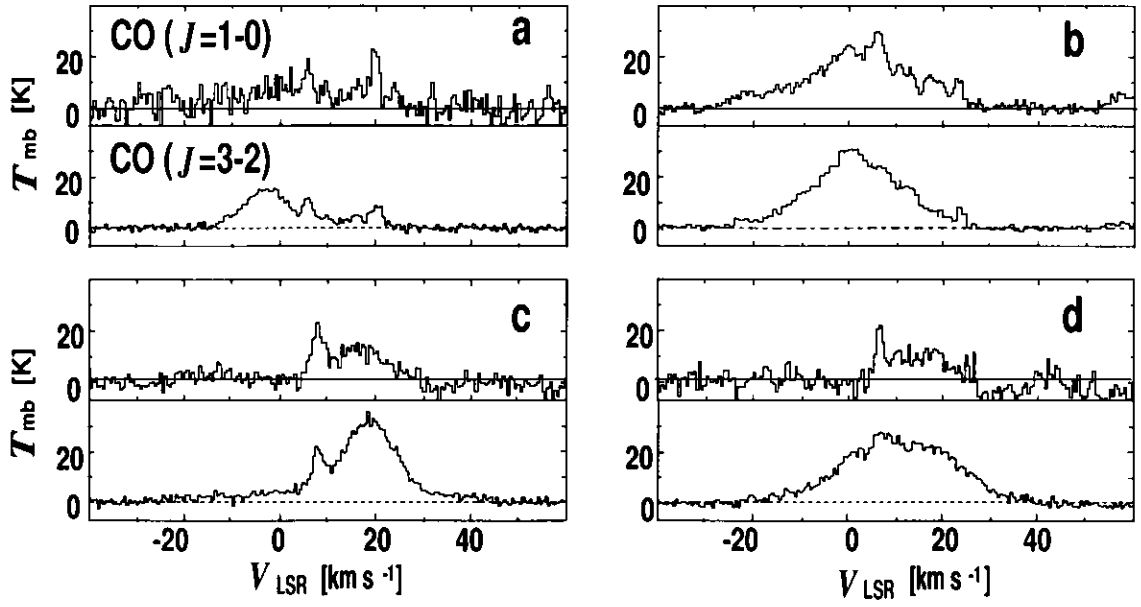

Fig. 3.5.— Examples of CO (J=1–0) and CO (J=3–2) spectra obtained towards four positions in SNR W28. The intensity of the broad component ($\Delta V \geq 20$ km s^{-1}) is stronger in CO (J=3–2) than in CO (J=1–0), while the intensity of the narrow component ($\Delta V \sim 2 - 3$ km s^{-1}) tends to be stronger in CO (J=1–0) than in CO (J=3–2). (**a**) RA(B1950) = $17^{h}58^{m}12^{s}.9$, DEC(B1950) = $-23°16'10''$; (**b**) RA(B1950) = $17^{h}57^{m}55^{s}.6$, DEC(B1950) = $-23°17'01''$; (**c**) RA(B1950) = $17^{h}58^{m}32^{s}.6$, DEC(B1950) = $-23°24'23''$; (**d**) RA(B1950) = $17^{h}58^{m}32^{s}.6$, DEC(B1950) = $-23°23'49''$.

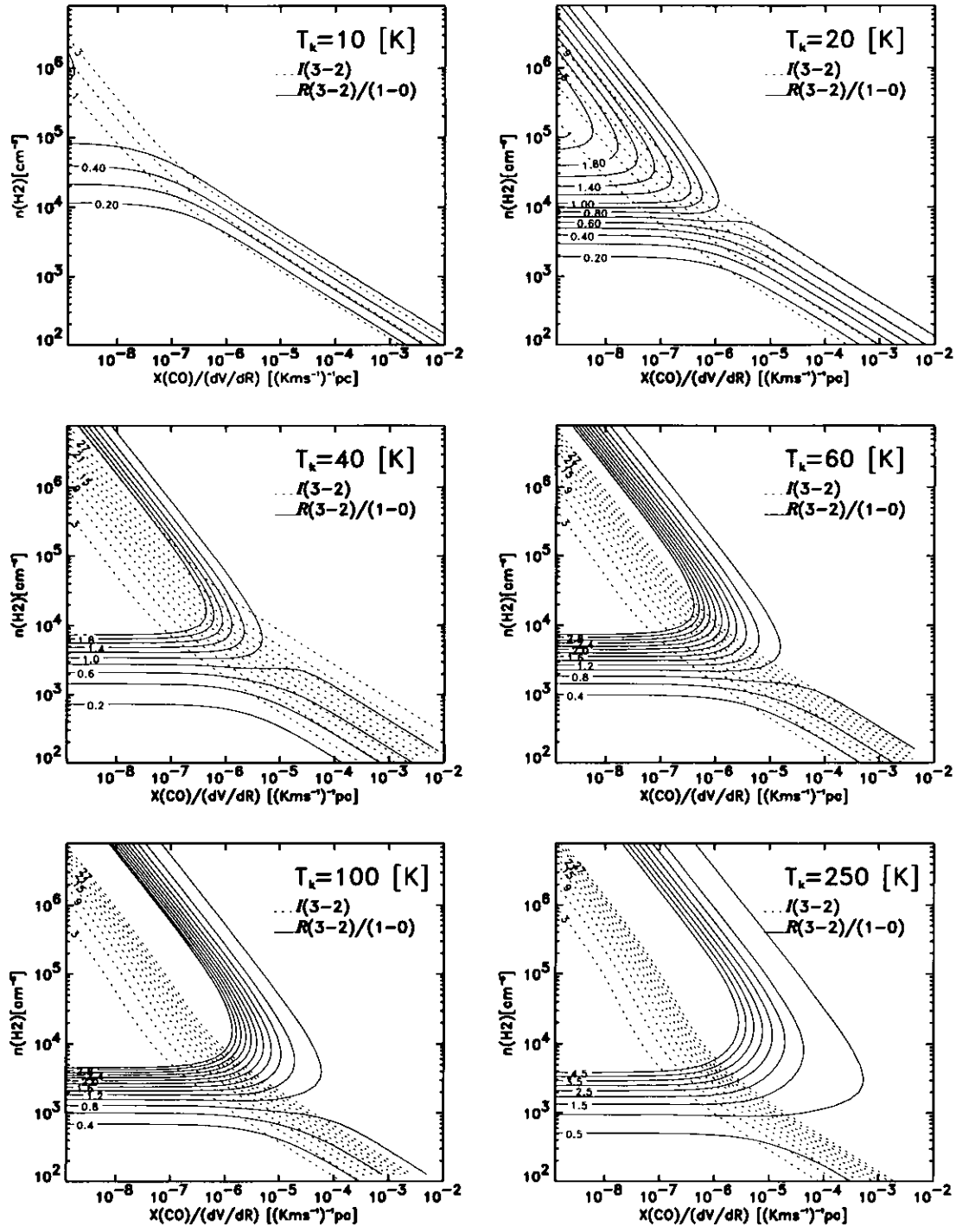

Fig. 3.6.— Results of the LVG calculations for the intensity ratio of CO (J=3–2) to CO (J=1–0) (solid lines) and the line intensity of CO (J=3–2) line (broken lines) as a function of CO fractional abundance per unit velocity gradient and molecular hydrogen density for fixed values of the kinetic temperature.

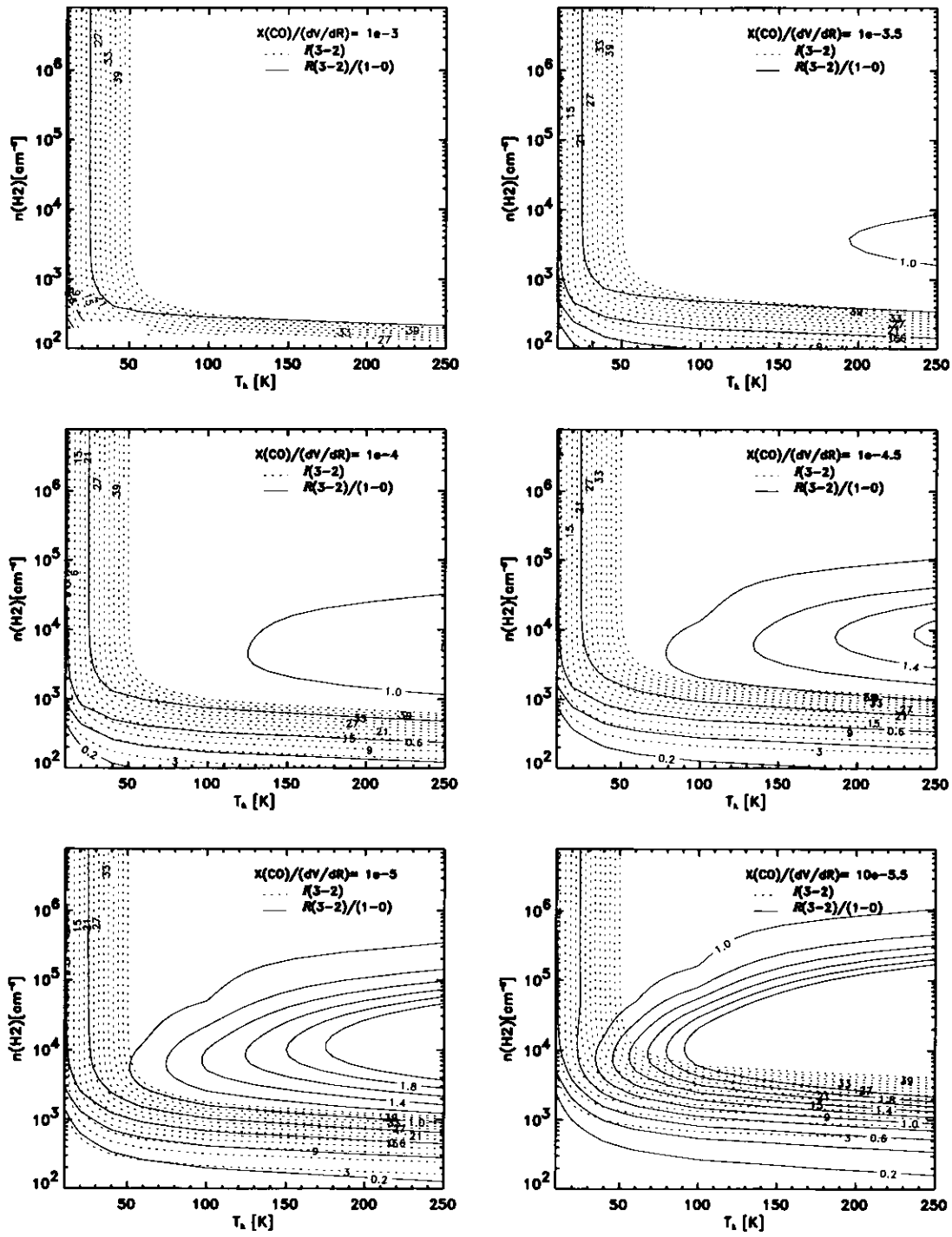

Fig. 3.7.— Results of the LVG calculations for the intensity ratio of CO (J=3–2) to CO (J=1–0) (solid lines) and the line intensity of CO (J=3–2) line (broken lines) as a function of kinetic temperature and molecular hydrogen density for fixed values of the CO fractional abundance per unit velocity gradient.

velocity gradient.

From these results, in unshocked gas, we found to have a kinetic temperature of $T_{\rm kin} \lesssim 20$ K and a density of $n({\rm H_2}) \lesssim 10^3$ cm^{-3}. For the quiescent unshocked gas which acompanies IC 443, van Dishoeck et al. (1993) calculated the kinetic temperature to be $T_{\rm kin} \sim 10 - 20$ K, and the density to be $n({\rm H_2}) \sim 3 \times 10^3 - 10^4$ cm^{-3} from the CO (J=3–2) and CO (J=2–1) data. Our parameters are similar to the parameters of the ambient gas near IC 443.

In the shocked gas, we found to have a kinetic temperature $T_{\rm kin} \gtrsim 60$ K and a density $n({\rm H_2}) \gtrsim 10^4$ cm^{-3}. It is shown that the wing component is dense and warm. In the shocked gas which accompanies W44, Seta et al. (1998) estimated from the CO (J=2–1) and CO (J=1–0) data that the kinetic temperature is $T_{\rm Kin} \sim 40 - 80$ K, and that the density is $n({\rm H_2}) \gtrsim 10^3$ cm^{-3}. In the CO shocked gas associated with IC 443, van Dishoeck et al. (1993) calculated the kinetic temperature to be $T_{\rm kin} \sim 80$ K, and the density to be $n({\rm H_2}) \sim 10^5$ cm^{-3}. Our parameters of shocked gas are similar to those of other interacting SNRs.

3.4.2 Mass

We estimated from the CO data the mass of the unshocked and shocked gas which accompanies W28.

For the unshocked gas, since it is optically thick, the LTE (local thermal equilibrium) method which assumes optically thin emission cannot estimate the mass. Then, we estimated the mass by using a conversion factor for the CO (J=1–0) integrated intensity :

$$N({\rm H_2}) \,/\, I_{\rm CO(J=1-0)} = 2.3 \times 10^{20} {\rm cm^{-2}\ K\ km\ s^{-1}}$$

(Bloemen 1989).

The east cloud has $M_{\rm unshocked(east)} = 3.4 \times 10^3$ M$_\odot$, and the north cloud has $M_{\rm unshocked(north)} = 7.1 \times 10^2$ M$_\odot$. The east cloud observed by Wootten (1981) is reported to have a mass of $M_{\rm unshocked} = 3.3 \times 10^3$ M$_\odot$, and it is almost equal to our value. The total mass of the unshocked gas is estimated to be $M_{\rm unshocked} = 4.1 \times 10^3$ M$_\odot$.

For the shocked gas, we used the LTE method. We cannot use the conversion factor, since the physical properties of the shocked gas are very different from usual

cloud. In the LTE method, the column density of CO can be expressed as

$$N(\mathrm{CO}) = \frac{3k^2}{8\pi^3 h}\ \frac{1}{\mu^2 B\nu J}\ T_{\mathrm{ex}}\ e^{\frac{hB(J+1)J}{kT_{\mathrm{ex}}}} \int T_{\mathrm{R}}^{*}(v)dv\ \frac{\tau}{1-e^{-\tau}}$$

We estimated the kinetic temperature of the shocked gas to be $T_{\mathrm{kin}} \gtrsim 60$ K from a LVG analysis. In IC 443 and W44, the excitation temperature was estimated to be $T_{\mathrm{ex}} = 80$ K and the line opacity to be of order unity (cf. van Dishoeck et al. (1993); Seta et al. (1998)). We used this T_{ex} and opacity for the LTE calculation. We assume [CO] / [H_2] = 1×10^{-4}. The east cloud has a mass of $M_{\mathrm{shocked(east)}} = 2.2 \times 10^3$ $M_\odot$, and the north cloud has a mass of $M_{\mathrm{shocked(north)}} = 5.5 \times 10^2$ $M_\odot$. Then, the total mass of the shocked gas is $M_{\mathrm{shocked}} = 2.7 \times 10^3$ $M_\odot$. About 30 % (in mass) of the molecular cloud has been shock-accelerated by the SNR (here we ignored dissociated CO).

3.4.3 Energy

The velocity width is typically $\Delta V \sim 10$ km s^{-1} in the north cloud, and typically $\Delta V \sim 20$ km s^{-1} in the east cloud. Thus, the total kinetic energy deposited in the shocked molecular gas is 3×10^{48} erg. The total energy of the supernova explosion is of order 10^{51} erg, and the above value corresponds 0.3 % of the energy of the supernova explosion. In IC 443, Dickman et al. (1992) estimated that the molecular gas has a kinetic energy of $(3 - 13) \times 10^{48}$ erg in CO (J=1–0) and HCO^+. In W44, Seta et al. (1998) estimated that the molecular gas has a kinetic energy of $\sim 4 \times 10^{48}$ erg in CO (J=2–1) and CO (J=1–0). It is found that the three SNRs have similar values of the kinetic energy deposited in the molecular cloud.

3.5 Conclusion

We observed SNR W28 and in CO (J=1–0) millimeter-wave emission, and deduced the physical condition of the molecular cloud which accompanies W28. The distribution of CO (J=1–0) toward SNR W28 globally resembles that of CO (J=3–2). From calculations of large velocity gradient (LVG) models, we found that the kinetic temperature is $T_{\mathrm{kin}} \lesssim 20$ K and the density is $n(H_2) \lesssim 10^3$ cm^{-3} in the unshocked gas, while $T_{\mathrm{kin}} \gtrsim 60$ K and $n(H_2) \gtrsim 10^4$ cm^{-3} in the shocked gas. The total mass of

TABLE 3.2

Parameters of the unshocked and shocked gas

Line width	narrow	broad
	2 – 3 km s^{-1}	$\gtrsim$20 km s^{-1}
CO (J=1–0)	strong	weak
CO (J=3–2)	weak	strong
3–2/1–0 ratio	0.4 – 0.7	2.3 – 2.8
Temperature	$\lesssim$20 K	$\gtrsim$60 K
Density $n(H_2)$	$\lesssim 10^3$ cm^{-3}	$\gtrsim 10^4$ cm^{-3}
Mass	4×10^3 $M_\odot$	2×10^3 $M_\odot$

the unshocked gas is estimated to be $M_{\rm unshocked}$= 4 × 10^3 $M_\odot$, and that of the shocked gas is $M_{\rm shocked}$= 2 × 10^3 $M_\odot$. This means that about 30 % (in mass) of the molecular cloud has been shock-accelerated by the SNR (here we ignored dissociated CO). The total kinetic energy deposited in the shocked molecular gas is 3 × 10^{48} erg, which is corresponds 0.3 % of the energy of the supernova explosion. Table 3.2 summarizes the physical parameters of the unshocked and shocked gas.

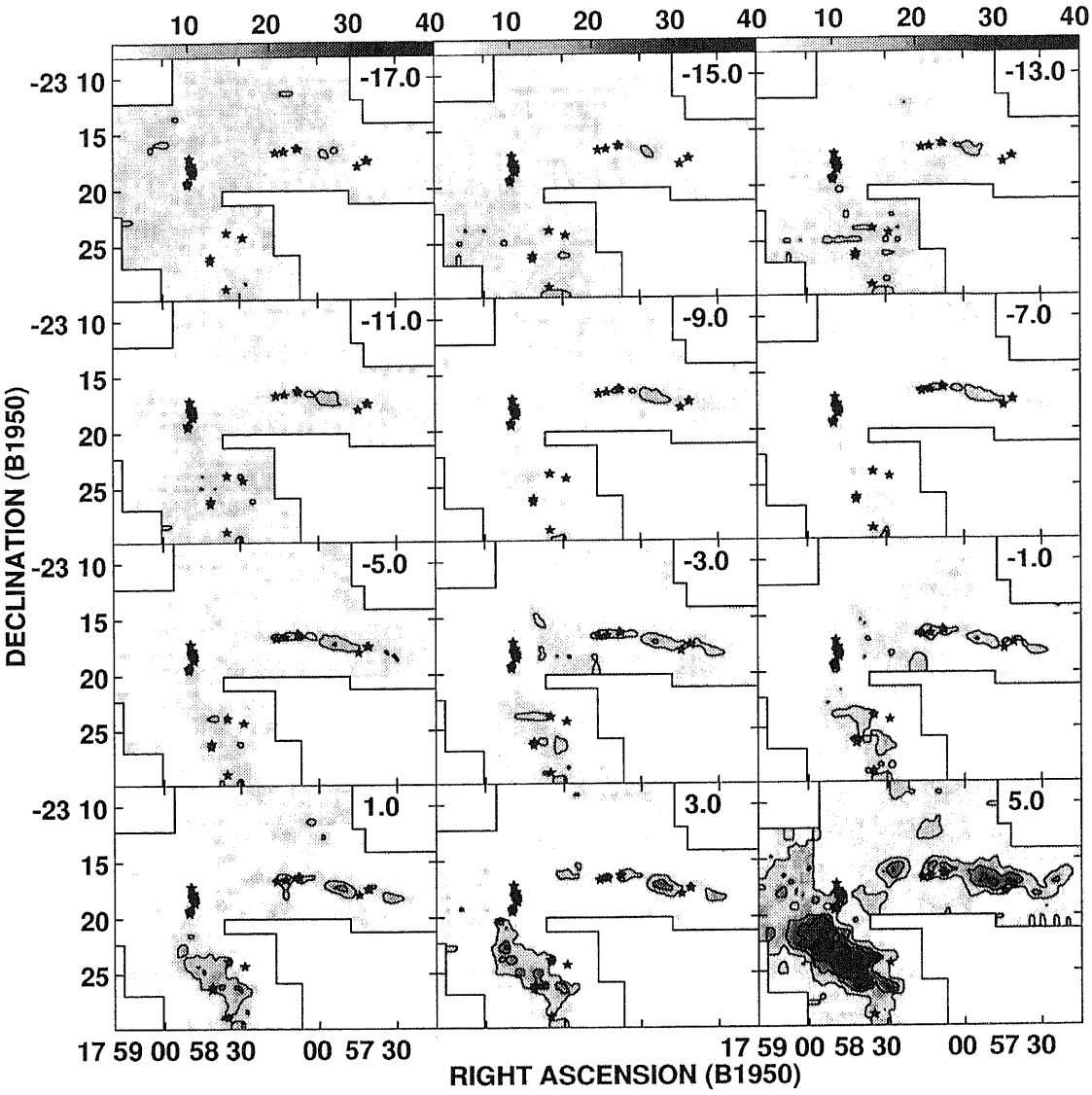

Fig. 3.8.— Part I of teh channel maps of the integrated CO (J=1–0) emission at 2 km s^{-1} velocity intervals toward W28. The center velocity is labeled at the upper right corner. The contour interval is 8.47 K km s^{-1}.

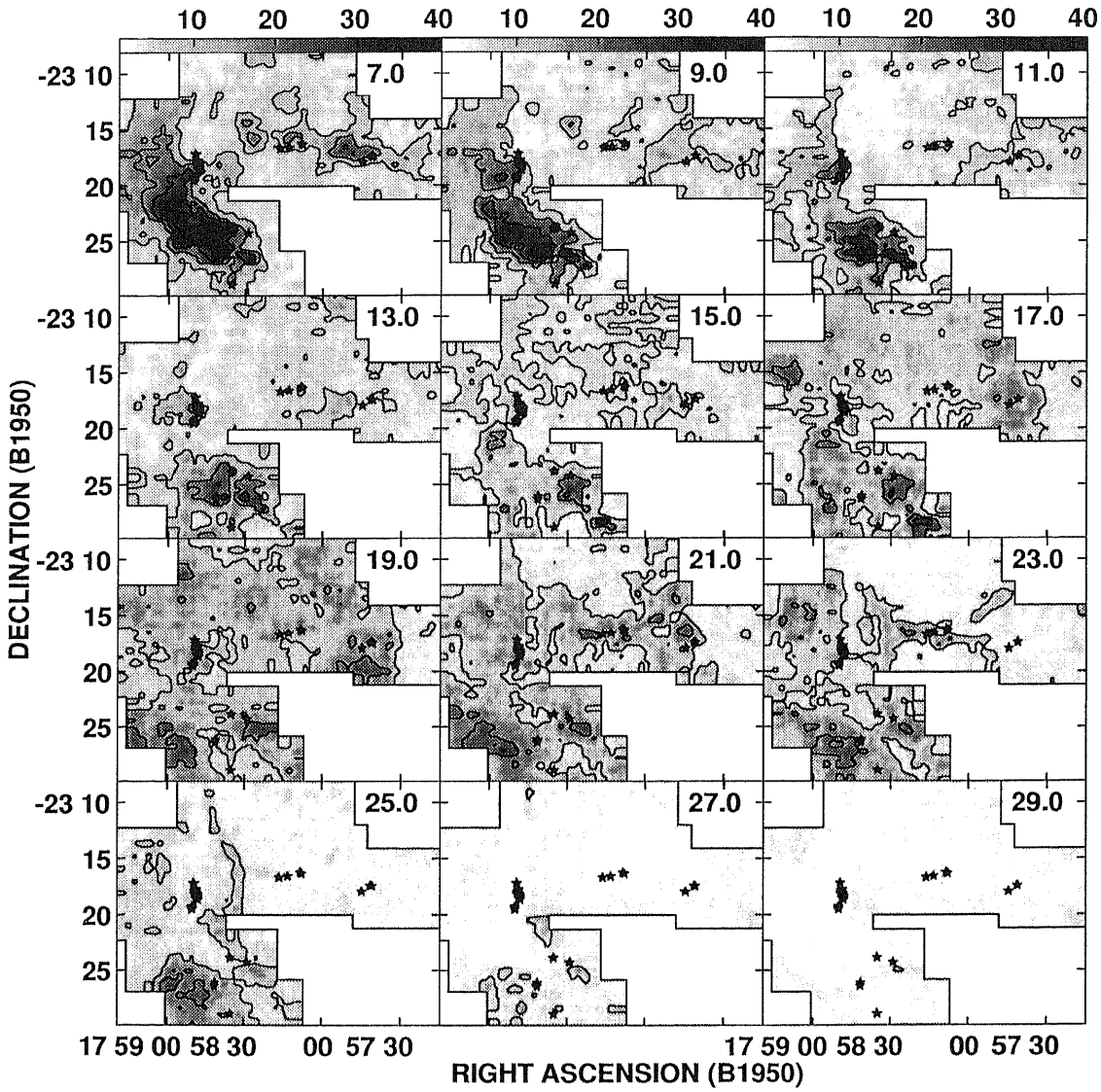

Fig. 3.9.— Part II of Channel maps of the integrated CO (J=1–0) emission in toward W28.

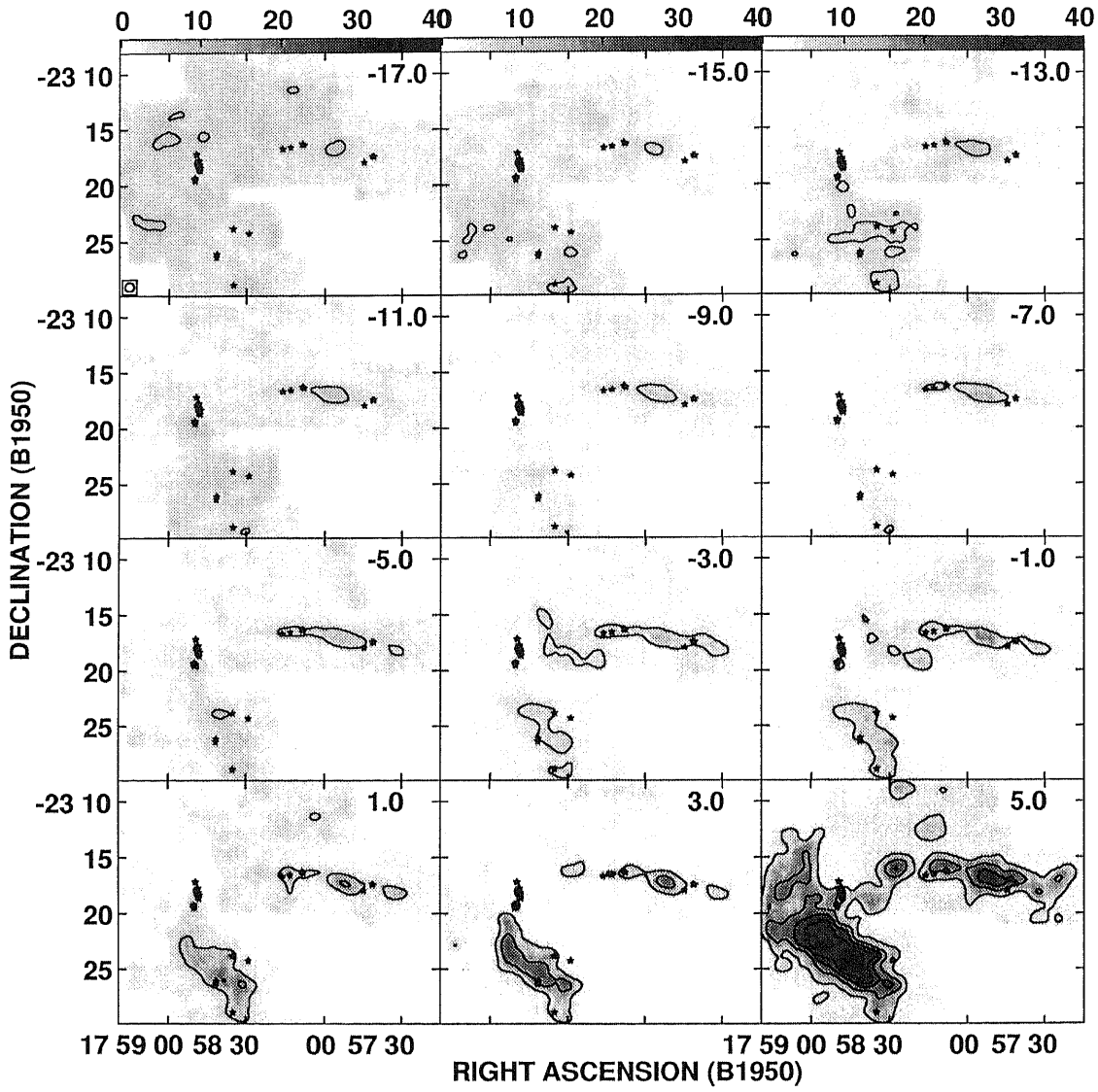

Fig. 3.10.— Part I of the channel maps of the integrated CO (J=1–0) emission at 2 km s^{-1} velocity intervals toward W28. The center velocity is labeled at the upper right corner. The contour interval is 6.86 K km s^{-1}. The resolution of CO (J=1–0) and CO (J=3–2) is made equal to 48″.

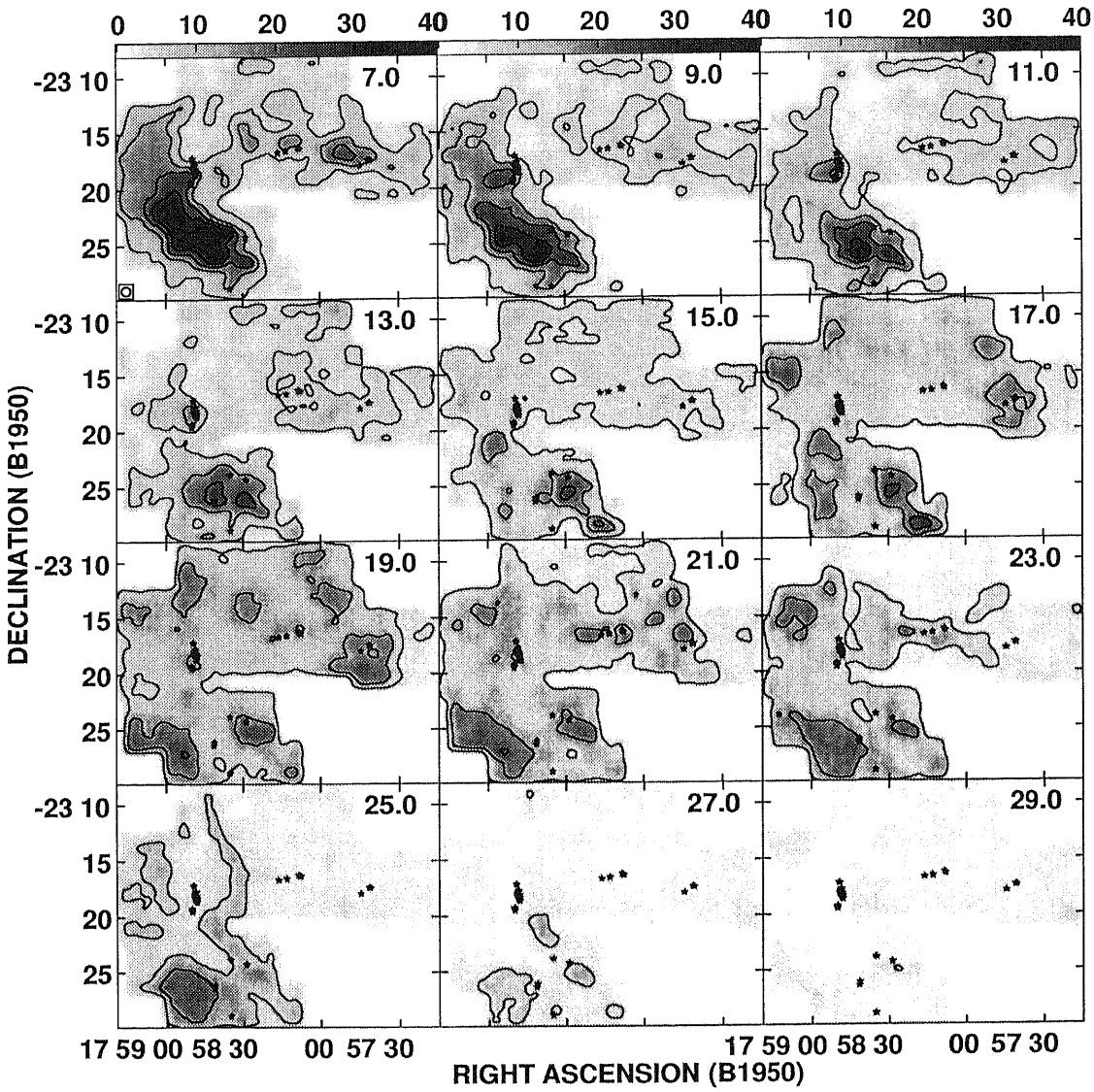

Fig. 3.11.— Part II of the channel maps of the integrated CO (J=1–0) emission toward W28.

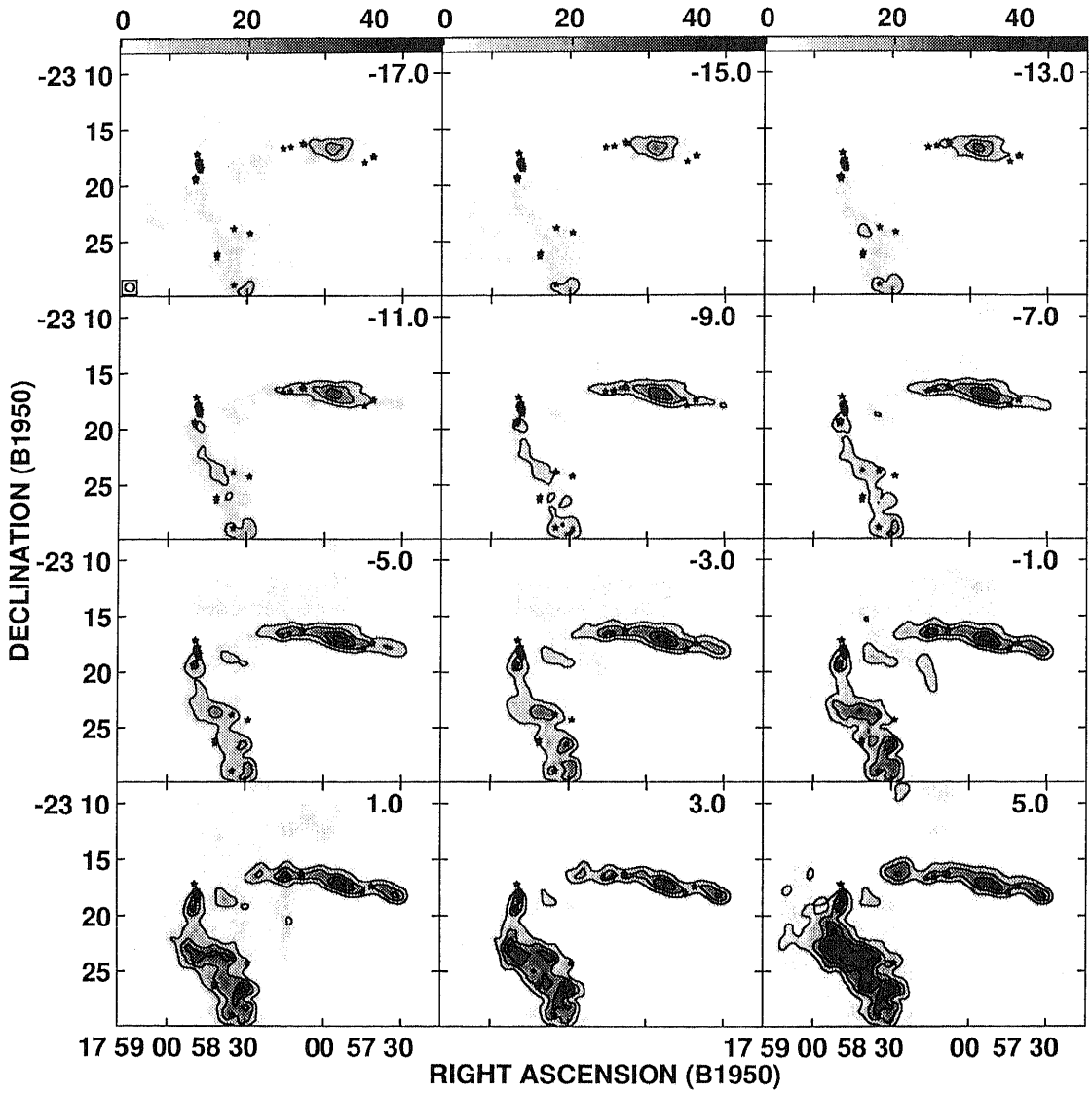

Fig. 3.12.— Part I of the channel maps of the integrated CO (J=3–2) emission at 2 km s^{-1} velocity intervals toward W28. The center velocity is labeled at the upper right corner. The contour interval is 9.65 K km s^{-1} starting from 6.76 K km s^{-1} by. The resolution of CO (J=1–0) and CO (J=3–2) is made equal to 48″.

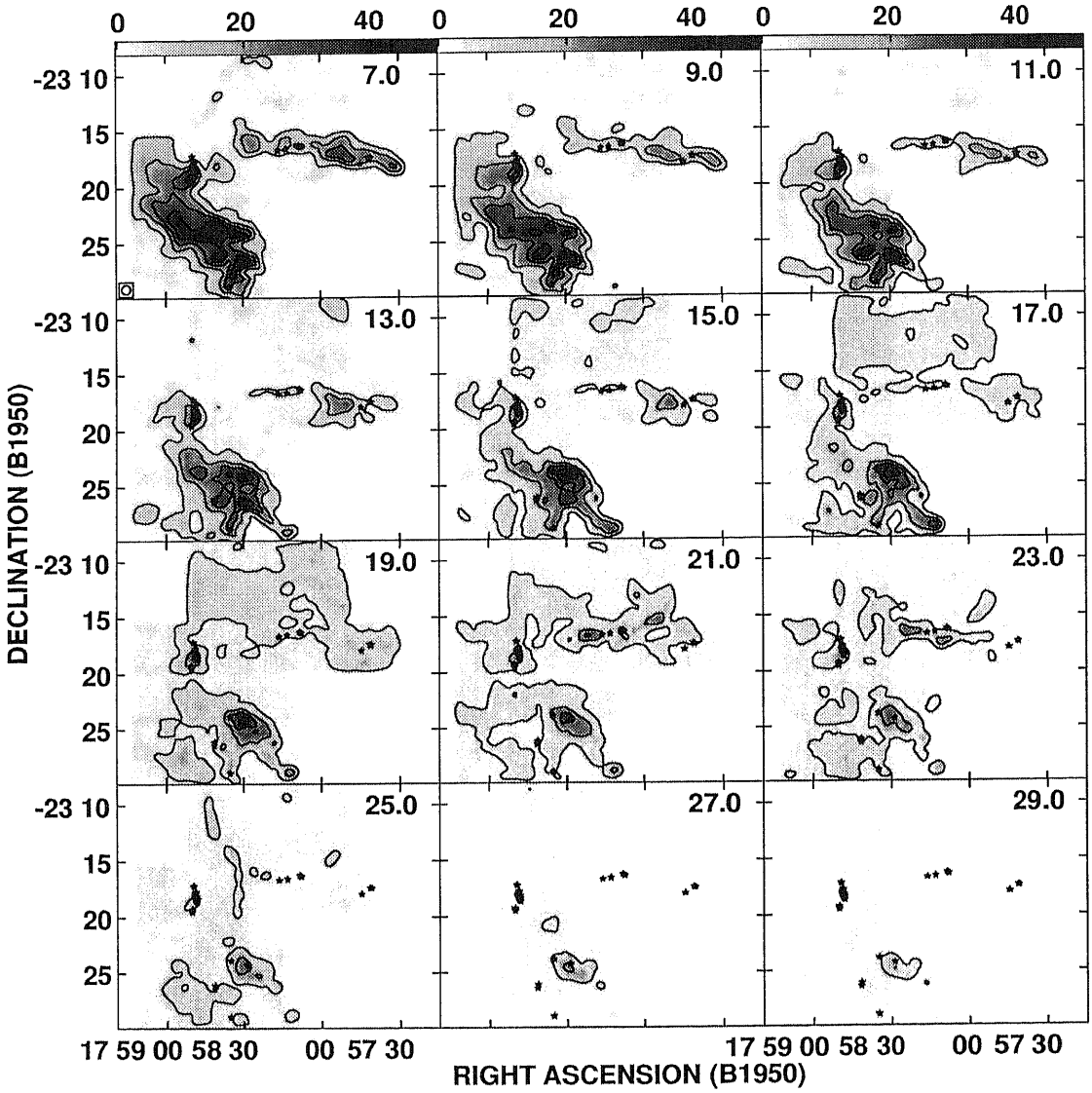

Fig. 3.13.— Part II of the channel maps of the integrated CO (J=3–2) emission toward SNR W28.

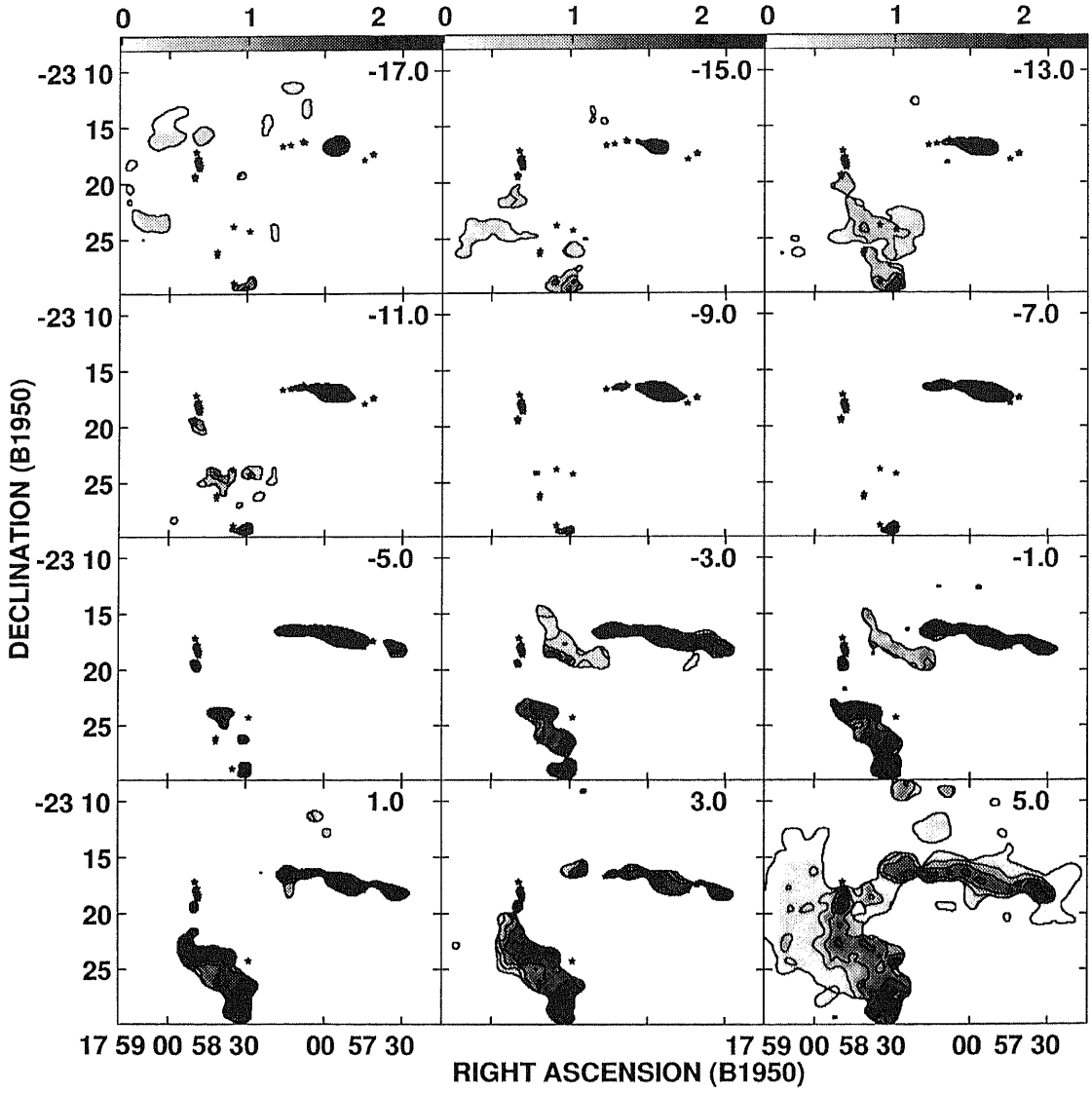

Fig. 3.14.— Part I of the channel maps of the CO (J=3–2)/ CO (J=1–0) integrated intensity ratio at 2 km s^{-1} velocity intervals. The center of the velocity is labeled at the upper right corner of each panel. The contour interval is 0.5.

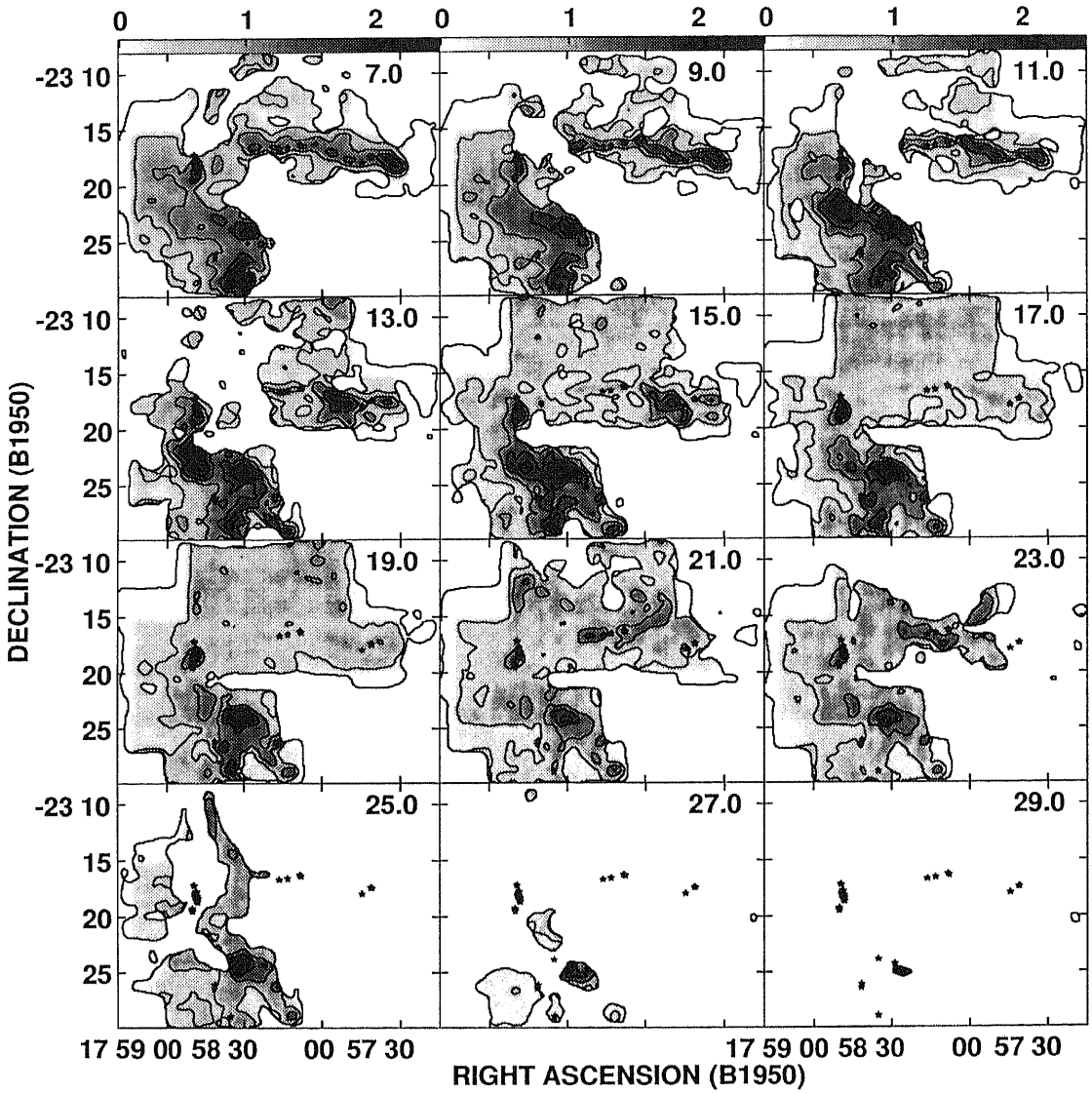

Fig. 3.15.— Part II of the channel maps of the CO (J=3–2)/ C10 integrated intensity ratio.

References

Arikawa, Y., Tatematsu, K., Sekimoto, Y., Takahashi, T. 1999, PASJ, 51, L7

Bloemen, H. 1989, ARA&A 27, 469

Claussen, M.J., Frail, D.A., Goss, W.M., Gaume, R.A. 1997, ApJ, 489, 143

Dickman, R.L., Snell, R.L., Ziurys, L.M., & Huang, Y.–L. 1992, ApJ, 400, 203

Esposito, J.A., Hunter, S.D., Kanbach, G., Sreekumar, P. 1996, ApJ, 461, 820

Flower, D.R. & Launary, J., 1985, MNRAS 214, 271

Goldreich, P., Kwan, J. 1974, ApJ, 189, 441

Kutner, M.L., Ulich, B.L. 1981, ApJ, 250, 341

Scoville, N.Z., Solomon, P.M. 1974, ApJ, 187, L67

Seta, M., Hasegawa, T., Dame, T.M., Sakamoto, S., Oka, T., Handa, T., Hayashi, M., Morino, J., Sorai, K., Usuda, K.S. 1998, ApJ, 505, 286

Sunada, K., Noguchi, T., Tsuboi, M., Inatani, J. 1995, in ASP Conf. Ser. 75, Multi–feed Systems for Radio Telescopes, ed P.T. Emerson, J.M. Payne (ASP, San Francisco) p230

van Dishoeck, E.F., Jansen, D.J., Phillips, T.G. 1993, A&A, 279, 541

Wootten, H.A. 1981, ApJ, 245, 105

Chapter 4

Large–scale CI ($^3P_1$–$^3P_0$) and CO(J=3–2) Observations toward IC 443, W28, W44, and W51

Abstract

We report mapping observations of CO (J=3–2) emission at 345.796 GHz (0.9 mm) and CI ($^3P_1$–$^3P_0$) emission at 492.161 GHz (0.6mm) toward four SNRs, IC 443, W28, W44, and W51, using Mt. Fuji submillimeter-wave telescope. It has been suggested that the abundance of neutral atomic carbon (CI) enhances due to the interaction between SNR and the molecular cloud. However, such enhancement has been reported for only one SNR, IC 443. We wonder whether this phenomenon is universal in the SNR–cloud interaction or not. We found that the distribution of the CI ($^3P_1$–$^3P_0$) emission toward W28, W44, and W51 complex region are similar to that of the CO (J=3–2) emission. In IC 443, the CI ($^3P_1$–$^3P_0$) emission was not detected. It is clear that the OH (1720 MHz) maser spots, which trace the SNR–cloud interaction are located at the edge of clumps in all 4 SNRs. In the shock region interacting of SNR with the molecular cloud, the CI ($^3P_1$–$^3P_0$)/CO (J=3–2) ratio tends to be high. On the other hand, in unrelated molecular clouds with SNR, the ratio is low. This result might imply that the interaction of SNR with the molecular cloud enhances the CI abundance.

TABLE 4.1

Summary of the Observed SNRs

Source	Distance [k pc]	Age [year]	Radius[e] [arcmin]	Size [pc / arcmin]
IC 443	1.5	5×10^4	45	0.44
W28	1.8	6×10^4	42	0.52
W44	2.9	4×10^5	35 × 27	0.84
W51C	6.0	3×10^4	30	1.75

4.1 Introduction

The interaction between supernova remnant (SNR) and the molecular cloud is a good "laboratory" for astrochemistry. It has been suggested that the abundance of neutral atomic carbon (CI) enhances due to the interaction between IC 443 and the molecular cloud (Phillips et al. 1993, White 1994). By observing ^{13}CO (J=2–1) and CI ($^3P_1$–$^3P_0$), Phillips et al. (1993) found that the abundance ratio of CI to CO in the broad line component (shocked gas) is > 0.5, and that in the narrow component (unshocked gas close to the shock front) is > 2 in IC 443. They have concluded that predominantly atomic region may mark the radiative precursor of the shock. White (1994) found that the CI/CO abundance ratio is $\sim$ 1.3 – 2.9 in shocked gas toward IC 443 C, and suggested that enhanced cosmic ray flux density increases the CI/CO ratio. However, the enhancement of CI abundance has been reported only for IC443. As it was described in chapter 1, IC 443 has been the unique example of the interaction between SNR and the molecular cloud (e.g. DeNoyer 1979, Burton et al. 1988, White et al. 1987) for two decades. It is not clear whether the CI enhancement is a universal phenomenon in the molecular cloud which interacts with SNRs.

In this chapter, we report the observations of CI ($^3P_1$–$^3P_0$) emission toward four SNRs in order to confirm whether the CI abundance enhances in other interacting SNR. For a comparison, we observed CO (J=3–2) submillimeter-wave line. The targets are W28 (see Chapter 2 and 3), IC443, W44 (Wootten 1979, Seta et al. 1998), and W51 (Koo & Moon 1997a, 1997b), for which the interaction has been reported.

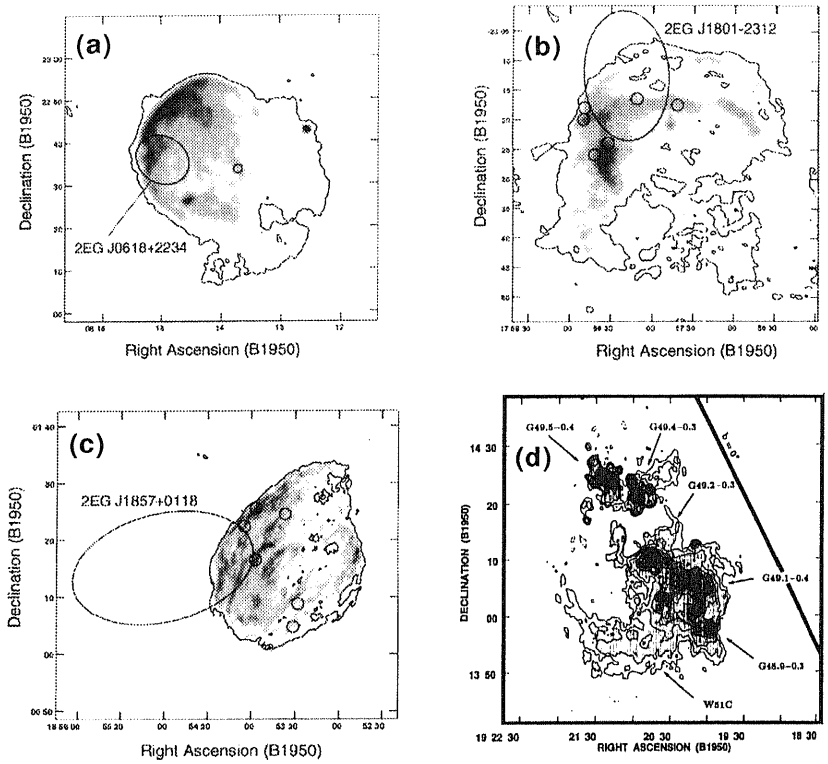

Fig. 4.1.— (a) A 333 MHz radio continuum image of the SNR IC 443: (b) A 327 MHz radio continuum image of the SNR W28: (c) A 1444 MHz radio continuum image of the SNR W44: (d) A 21 cm radio continuum image of the W51 complex region. In (a),(b), and (c),Large ellipses are the EGRET error circles, smaller circles are the regions of OH (1720 MHz) maser. (Claussen et al. 1999 in (a),(b), and (c), Koo & Moon 1997 in (d).

The basic parameters of the four SNRs are summarized in Table 4.1, and Figure 4.1 shows a radio continuum images of the four SNRs (Claussen et al. 1999 for W28, W44, and IC 443; Koo & Moon 1997 for W51). From all these four SNRs, OH (1720 MHz) maser spots, which trace the interaction between SNR and the molecular cloud were detected (Green et al. 1997, Claussen et al. 1997). The small circles of Figure 4.1 show the OH (1720 MHz) maser spot positions. Besides, from three SNRs (W28, W44, and IC 443), the gamma-ray emission detected with the EGRET detector (Esposito et al. 1996). The large ovals of Figure 4.1 show the EGRET positions in W28, W44, and IC 443.

TABLE 4.2

Observational summary.

Source	Positions RA (B1950)	DEC (B1950)	V_{LSR} [km s^{-1}]	Numbers of Spectra	Area [arcmin]
IC 443	06 13 42.2	+22 33 43	−10	182	$40' \times 40'$
W28	17 58 49.5	−23 17 10	7	160	$50' \times 30'$
W44	18 53 54.6	+01 25 19	45	374	$60' \times 50'$
W51C	19 20 35.9	+14 09 54	70	700	$80' \times 80'$

Note.— Units of right ascension are hours, minutes, and seconds, and units of declination are degrees, arcminutes, and arcseconds.

The map centers are the positions of the OH (1720 MHz) maser (Claussen et al. 1997 for IC 443, W28, and W44, Green et al. 1997 for W51).

First, we discuss the distribution of CI ($^3P_1$–$^3P_0$) emission and CO (J=3–2) emission. Second, we discuss whether the relative abundance of CI is enhanced in these SNRs.

4.2 Observations

The data of CO (J=3–2) at 345.796 GHz and CI ($^3P_1$–$^3P_0$) at 492.161 GHz toward the four SNRs, IC 443, W28, W44, and W51C, were obtained by using Mt. Fuji submillimeter-wave telescope at the summit of Mt. Fuji (Appendix A), from 1998 December to 1999 March. The telescope has a half power beam width of $\sim$ 3′.0 and 2′.2 at CO (J=3–2) and CI ($^3P_1$–$^3P_0$), respectively. The pointing of telescope was checked by the continuum observations of the sun and the moon, and the pointing accuracy is estimated to be 20″ (rms). We used 345 GHz/492 GHz dual band SIS (Superconductor–Insulator–Superconductor) mixer receivers. The system noise temperature was typically 500 K (DSB) and 1500 K (SSB) for 345 GHz and 492 GHz, respectively. The backend is a 1024-channel acousto-optical spectrometer (AOS) with a total bandwidth of 700 MHz. CO (J=3–2) and CI ($^3P_1$–$^3P_0$) were observed simultaneously. The mapping observations were made at grid spacings of 3′. We employed

the position switching mode. We calibrated the data using the standard chopper wheel method. We report the line intensity in terms of the main-beam brightness temperature $T_{\rm mb} = T_{\rm A}^{*}/\eta_{\rm mb}$ (Kutner & Ulich 1981).

Table 4.2 lists of the observational parameters. The map centers are the positions of the OH (1720 MHz) masers (Claussen et al. 1997 for IC 443, W28, and W44; Green et al. 1997 for W51). Except for IC 443, the total integration time is typically 120 s for CO (J=3–2) and 480 s for CI ($^3P_1$–$^3P_0$) for each position, and the resultant rms noise temperature is about 0.1 K and 0.2 K, respectively. In the observations of IC 443, the integration time is typically 120 s for CO (J=3–2) and 90 s for CI ($^3P_1$–$^3P_0$) for each position, and the resultant rms noise temperature is about 0.1 K and 0.7 K, respectively.

4.3 Results

4.3.1 IC443 (G189.1+0.3)

We mapped an area of 40′ × 40′ covering the north-eastern side of IC 443, where the interaction with molecular cloud takes place. The number of the observed positions is 182. The profile maps of the CO (J=3–2) at 345 GHz and CI ($^3P_1$–$^3P_0$) at 492 GHz emission are shown in Figures 4.12 and 4.13, respectively. The integrated intensity maps of the CO (J=3–2) and CI ($^3P_1$–$^3P_0$) emission are shown in Figure 4.5. The integration was made between $V_{\rm LSR} = -50$ km s^{-1} and 20 km s^{-1}. The channel maps of the integrated intensity CO (J=3–2) and CI ($^3P_1$–$^3P_0$) emission at 2 km s^{-1} velocity intervals are shown in Figures 4.20 through 4.23, and the channel center velocity is labeled at the top right corner of each panel. The stars marked on Figure 4.5, 4.20, 4.21, 4.22, and 4.23 are 6 OH (1720 MHz) maser spots, which were detected by Claussen et al. (1997). The CI ($^3P_1$–$^3P_0$) emission could not be detected in IC 443. This can be due to shorter integration time.

In the CO (J=3–2) line, we successfully detected broad profile (wing) from the shock-accelerated molecular gas. The maximum linewidth of the broad component was found in clump G (designated by Huang et al. 1986), and the line width (FWHM) was $\Delta V \sim 22$ km s^{-1} there. In addition, we observed a narrow self-absorption at a velocity

$V_{\rm LSR}$ = −5 km s^{-1}. Such line profile was also detected in other lines (White et al. 1987, van Dishoeck et al. 1993; Tauber et al. 1994) at the same position. From the integrated intensity map, it is proven that the distribution of CO (J=3–2) gas is ω-shaped like the distributions of the IRAS 60 μm and 100μm. The cloud has been divided into clumps, A, B, C, D, E, and F (see Figure 1.2: van Dishoeck et al. 1992), and we detected CO (J=3–2) from all of them. It is found that the position of OH (1720 MHz) maser spots are located at edge of clump G in the side of the supernova blast center.

4.3.2 W28 (G6.4–0.1)

As it was described in Chapters 1 and 2, we detected a broad CO (J=3–2) line emission (maximum linewidth reaches ΔV ~ 70 km s^{-1} at full width half maximum), and found that the distribution of the shocked gas is similar to that of the radio-continuum emission, that the unshocked gas is displaced by 0.4 – 1.0 pc outward with respect to the shocked gas.

We mapped an area of 50′ × 30′ covering north-eastern side of W28, where is observed by chapter 2 and 3. The number of the observed positions is 182. The profile maps of the CO (J=3–2) at 345 GHz and CI ($^3P_1$–$^3P_0$) at 492 GHz emission are shown in Figures 4.14 and 4.15, respectively. The integrated intensity maps of the CO (J=3–2) and CI ($^3P_1$–$^3P_0$) emission are shown in Figure 4.6. The integration were made between $V_{\rm LSR}$ = −30 km s^{-1} and 40 km s^{-1}. Figure 4.7 shows CI ($^3P_1$–$^3P_0$)/ CO (J=3–2) integrated intensity ratio map. The channel maps of the integrated intensity CO (J=3–2) and CI ($^3P_1$–$^3P_0$) emission at 2 km s^{-1} velocity intervals are shown in Figures 4.24 through 4.27. The channel maps of the CI ($^3P_1$–$^3P_0$)/ CO (J=3–2) integrated intensity ratio at 2 km s^{-1} velocity intervals are shown in Figures 4.28 and 4.29. The stars in Figures 4.6, and Figures 4.24 through 4.29 are 41 OH (1720 MHz) maser spots which were detected by Claussen et al. (1997).

As it is clear from Figure 4.14, the broad wing emission was observed in the CO (J=3–2) emission. At RA(B1950) = $17^{\rm h}58^{\rm m}36^{\rm s}.4$, DEC(B1950) = −23°26′10″, the linewidth is the broadest, ΔV ~ 23 km s^{-1}. The peak intensity is also the strongest at the same position, and the main beam brightness temperature is $T_{\rm mb}$ = 11.6 K. Due to a larger beam size, $T_{\rm mb}$ is lower than from the high-resolution observations (13″) by

using JCMT (see Chapter 2). The broad emission, which as detected in CO (J=3–2) emission, was not detected in the CI ($^3P_1$–$^3P_0$) emission. The strongest CI ($^3P_1$–$^3P_0$) emission was observed at RA(B1950) = $17^h58^m49^s.5$, DEC(B1950) = $-23°23'10''$, and the peak temperature is T_{mb} = 9.8 K and the linewidth is $\Delta V \sim 4 - 5$ km s^{-1} there. The peak velocity is V_{LSR} = 6.5 km s^{-1}, which is close to the systemic velocity of SNR W28 ($V_{sys} \sim 7$ km s^{-1}.)

The distribution of CI ($^3P_1$–$^3P_0$) emission is very similar to that of the CO (J=3–2) emission and to the 327 MHz radio continuum emission (Frail et al. 1994). The distribution of gas can be divided into two clumps: the north and east clouds (Chapters 2 and 3). The OH (1720 MHz) maser spots tend to be located along the edge of the clumps rather than at the center of the clumps.

4.3.3 W44 (G34.7–0.4)

SNR W44 is a well known SNR in the inner Galaxy. Wootten (1997) observed a velocity gradient and broad linewidth of ^{12}CO (J=1–0) and ^{13}CO (J=1–0), and suggested that the interstellar medium has been compressed and heated by the remnant. Seta et al. (1998) indicated that the CO (J=2–1) / CO (J=1–0) intensity ratio is extremely high (>3) in the high-velocity line wing emission within clouds overlapping with the SNR, and suggested that there exists dense (N(H_2) $\sim 10^5$ cm^{-3}) and warm ($\sim$ 80 K) gas.

We mapped an area of 60′ × 50′ covering "cloud 3" designated by Seta et al. (1998). The number of the observed positions is 372. The profile maps of the CO (J=3–2) at 345 GHz and CI ($^3P_1$–$^3P_0$) at 492 GHz emission are shown in Figures 4.16 and 4.17, respectively. The integrated intensity maps of the CO (J=3–2) and CI ($^3P_1$–$^3P_0$) emission are shown in Figure 4.8. The integration were made between V_{LSR} = 30 km s^{-1} and 60 km s^{-1}. Figure 4.9 shows CI ($^3P_1$–$^3P_0$)/ CO (J=3–2) integrated intensity ratio map. The channel maps of the CO (J=3–2) and CI ($^3P_1$–$^3P_0$) emission at 2 km s^{-1} velocity intervals are shown in Figures 4.30 through 4.33. The channel maps of the CI ($^3P_1$–$^3P_0$)/ CO (J=3–2) integrated intensity ratio at 2 km s^{-1} velocity intervals are shown in Figures 4.34 and 4.35. The stars in Figure 4.8, and Figure 4.30 through 4.35 are 28 OH (1720 MHz) maser spots which were detected by Claussen et al. (1997).

In SNR W44, the distribution of CI ($^3P_1$–$^3P_0$) emission is generally similar to that of the CO (J=3–2) emission. Many velocity components exist, and CI ($^3P_1$–$^3P_0$) and CO (J=3–2) profiles usually resemble each other. At RA(B1950) = $18^h55^m30^s.0$, DEC(B1950) = 01°33′33″, the intensity is the strongest (T_{mb} = 15 K in CO (J=3–2) , T_{mb} = 9 K in CI ($^3P_1$–$^3P_0$)), and the linewidth is ΔV $\sim$ 5.5 km s^{-1} and 4.9 km s^{-1} in CO (J=3–2) and CI ($^3P_1$–$^3P_0$), respectively. It should be noted that the velocity of this cloud is V_{LSR} = 34 km s^{-1}, which differs from the systemic velocity of SNR W44 (V_{sys} $\sim$ 42 km s^{-1}). Moreover, the distribution is largely different from the radio continuum distribution of SNR W44. Therefore, this cloud is suggested to be an unrelated cloud. The molecular cloud associated with W44 is located at the edge of the northeastern side of SNR, with a size of 1° × 30′ , and is called "cloud 3" by Seta et al. (1998). This cloud can be divided into three clumps. In CI ($^3P_1$–$^3P_0$) emission, the clump near SNR is the strongest, the peak intensity is T_{mb}(CI) = 5.3 K, and the linewidth is ΔV $\sim$ 4.8 km s^{-1}. In CO (J=3–2) emission, since various velocity components overlap, it is difficult to separate then. The peak intensity is $\sim$ T_{mb}(CO) = 4.4 K.

Some OH (1720 MHz) maser spots are located at the edge of the clumps ("OH E", "F", and "D", which were designated by Claussen et al. (1997)), but some are located outside clouds ("OH B" and "C").

4.3.4 W51 (G49.2–0.7)

The W51 complex region is very complicated, and it consists of "W51A", "W51B", and "W51C". It is one of the massive star forming regions in our Galaxy. There exist five compact HII regions. One group of the HII regions, G49.4–0.3 and G49.5–0.4, is called W51A, and another group, G48.9–0.3, G49.1–0.4, and G49.2–0.4, is called W51B. W51C has a nonthermal spectrum and is suggested to be a composite-type supernova remnant. Koo & Moon (1997a, b) suggested that SNR W51C interacts with the molecular cloud (W51B) from HI 21 cm observations, and CO (J=2–1), CO (J=1–0), ^{13}CO (J=1–0), and HCO$^+$ (J=1–0) observations.

We mapped an area of 80′ × 80′ covering the whole W51 complex region, including W51A, W51B, and W51C (SNR). The number of the observed positions is 700 points. The profile maps of the CO (J=3–2) at 345 GHz and CI ($^3P_1$–$^3P_0$) at 492 GHz emission

are shown in Figures 4.18 and 4.19, respectively. The integrated intensity maps of the CO (J=3–2) and CI ($^3P_1$–$^3P_0$) emission are shown in Figure 4.10. The integration were made between V_{LSR} = 30 km s^{-1} and 80 km s^{-1}. Figure 4.11 shows CI ($^3P_1$–$^3P_0$)/ CO (J=3–2) integrated intensity ratio. The channel maps of the CO (J=3–2) and CI ($^3P_1$–$^3P_0$) emission at 2 km s^{-1} velocity intervals are shown in Figures 4.36 and 4.39. The channel maps of the CI ($^3P_1$–$^3P_0$)/ CO (J=3–2) integrated intensity ratio at 2 km s^{-1} velocity intervals are shown in Figures 4.40 and 4.41. The stars in Figures 4.10, and Figure 4.36 though 4.41 are two OH (1720 MHz) maser spots, which were detected by Green et al. (1997).

Globally, the distribution of the CI ($^3P_1$–$^3P_0$) emission is similar to that of the CO (J=3–2) emission. It is found from the channel map and the profiles that various velocity components exist. Two clumps have the systemic velocity of W51A HII region (V_{LSR} = 49 – 53 km s^{-1}). These two clumps correspond to compact HII regions G49.5–0.4 and G49.4–0.3, respectively. The main-beam brightness temperature at G49.5–0.4 is T_{mb}(CO) = 19.6 K and T_{mb}(CI) = 9.6 K, which is brightest in the whole W51 complex region. In V_{LSR} = 59 – 65 km s^{-1}, the cloud extends to the northwest from the radio-continuum emission of the SNR. According to Carpenter & Sanders (1998), this cloud is called "theW51 giant molecular cloud ". The intensity of this cloud component is weaker than those of other velocity components. In the velocity of OH (1720 MHz) maser spots (V_{LSR} = 67 – 73 km s^{-1}), the distribution of cloud becomes narrow in shape, extending from northeast to southwest. This distribution of this component connects W51A and W51B. There are three clumps in this filamentary cloud. One corresponds to W51A (we call here this clump "W51A (HII region)"), and the other two correspond to W51B. One of the latter clumps are associated with the non-thermal emission and the OH (1720 MHz) maser, which suggests the emission comes from an SNR interacting with a molecular cloud. Koo & Moon (1997a, b) pointed out the interaction between SNR and the molecular cloud in this region for the first time. We call here the clump associated with the OH (1720 MHz) maser "W51B (OH maser)", and call the other "W51B (HII region)". The OH (1720 MHz) maser is located at the edge of W51B (OH maser).

4.4 Discussion

4.4.1 Overall distribution of CI ($^3P_1$–$^3P_0$) and CO (J=3–2)

For the three SNRs (W28, W44, and W51), CI ($^3P_1$–$^3P_0$) emission is very extended, and the distribution of CI ($^3P_1$–$^3P_0$) emission is very similar to that of the CO (J=3–2) emission. CI forms when CO is dissociated by ultraviolet photons (UV–radiation). Therefore, CI exists in the relatively thin layer near the surface of the molecular cloud at $A_v \sim 3 - 8$ (e.g. Keene et al. 1986). Homogeneous photo-dissociation region (PDR) models (e.g. Tielens and Hollenbach 1985), cannot explain CI inside the molecular cloud. The observational results shows that the molecular cloud consists of a numerous small clumps and that the UV–radiation penetrates throughout the molecular cloud (e.g. Stutzki et al. 1988, Tauber & Goldsmith 1990, Meixner et al. 1992).

4.4.2 Comparison between the CI ($^3P_1$–$^3P_0$) and CO (J=3–2) spectra

In order to investigate whether the interaction of SNRs with the molecular cloud enhances the CI abundance, we compare line profiles between interacting region and a comparison region.

In W44, we compare three clumps : (1) the clump inside SNR (SNR inner), (2) that which is close to the edge at SNR (SNR edge), and (3) that which is unrelated to SNR (SNR outer). The upper panel of Figure 4.3 shows the integrated intensity map of the CI ($^3P_1$–$^3P_0$) emission of the SNR W44. The integration was made between V_{LSR} = 20 km s^{-1} and 60 km s^{-1}. The top-side of the lower panels shows the line profiles of the composite spectrum averaged over each clump. The red lines show CO (J=3–2) spectra, and the green line show CI ($^3P_1$–$^3P_0$) spectra. The bottom-side of the lower panels represents the intensity ratio of CI ($^3P_1$–$^3P_0$) to CO (J=3–2) for each clump. The line parameters toward W44 are summarized in Table 4.3. The CI ($^3P_1$–$^3P_0$)/CO (J=3–2) intensity ratio in the clump which is unrelated to SNR is $\lesssim$ 0.6, while the ratio in the clumps which is related to SNR are $\gtrsim$0.8. The CI ($^3P_1$–$^3P_0$) / CO (J=3–2) ratio in the interacting region is larger than values observed in the region unrelated to SNR.

TABLE 4.3

Line parameters of CI and CO(3–2) toward W44

Position	T_{mb} K		ΔV km s^{-1}		V_{LSR} km s^{-1}		$\frac{T_{mb}(CI)}{T_{mb}(CO)}$
	CI	CO	CI	CO	CI	CO	
SNR inner	2.5	2.9	6.4	11.9	45.7	46.4	0.9
SNR edge	2.4	2.6	6.0	10.1	45.7	45.6	0.9
SNR outer	2.6	4.1	5.8	8.2	47.4	47.2	0.6

TABLE 4.4

Line parameters of CI and CO(3–2) toward W51

Position	T_{mb} K		ΔV km s^{-1}		V_{LSR} km s^{-1}		$\frac{T_{mb}(CI)}{T_{mb}(CO)}$
	CI	CO	CI	CO	CI	CO	
W51B(OH maser)	2.2	3.1	9.9	11.8	66.0	66.1	0.7
W51B(HII region)	1.5	4.7	7.0	8.5	66.0	66.1	0.3
W51A(HII region)	3.3	7.9	17.6	14.6	62.6	58.9	0.4

Second, we compare line profiles in W51 complex region. Figure 4.4 shows the line profiles of the composite spectrum averaged over each clump in W51. The line parameters toward W51 complex region are summarized in Table 4.4. The maximum linewidth of the broad component reaches $\Delta V \sim 40$ km s^{-1} (full width at zero intensity). The CI ($^3P_1$–$^3P_0$)/CO (J=3–2) intensity ratio in the W51A (HII region) and W51B (HII region) is $\sim$ 0.3 – 0.4, while the ratio in the W51B (OH maser) is $\gtrsim$0.7. The CI ($^3P_1$–$^3P_0$)/ CO (J=3–2) ratio in the interacting region is larger than values observed in the HII region. It is also found that the ratio tends to be high in the middle of the CO profile, in spectrum.

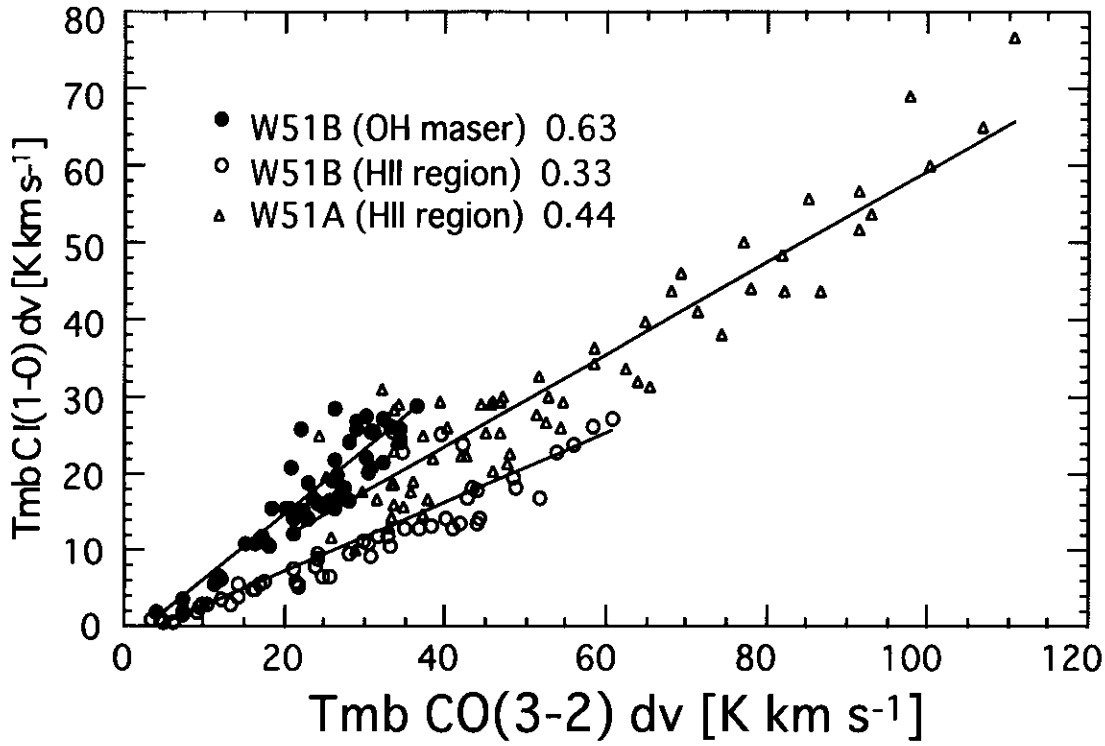

Fig. 4.2.— The CI ($^3P_1$–$^3P_0$)integrated intensities plotted against th e CO (J=3–2) integrated intensities in the velocity of OH (1720 MHz) maser at $V_{\rm LSR}$ = 65 – 72 km s^{-1}. The thick solid lines denote linear fits to the data.

4.4.3 Comparison between the CI ($^3P_1$–$^3P_0$) and CO (J=3–2) intensity ratio

For W51 complex region, we also compare the CI ($^3P_1$–$^3P_0$) and CO (J=3–2) integrated intensity at each position. It is clear from Figure 4.2 that W51B (OH maser) has larger CI ($^3P_1$–$^3P_0$)/ CO (J=3–2) intensity ratio than W51A (HII region) and W51B (HII region). The CI ($^3P_1$–$^3P_0$)/ CO (J=3–2) ratio is 0.63 at W51B (OH maser), while the ratio is 0.33 at W51A (HII region), and 0.44 at W51B (HII region). The ratio at W51A (HII region) and W51B (HII region) is close to values for HII regions such as the Orion Nebula (Ikeda et al. 1999) and DR21 (Saito et al. 1999) observed with the Mt. Fuji submillimeter wave telescope (0.2 – 0.45).

Now, we calculate the CI ($^3P_1$–$^3P_0$)/ CO (J=3–2) ratio at IC 443 which re-

ported the enhancement of CI abundance due to the SNR–cloud interaction. By using the data of CI ($^3P_1$–$^3P_0$) of White (1994) and the data of CO (J=3–2) of van Dishoeck et al.(1993), we estimated to be CI ($^3P_1$–$^3P_0$)/ CO (J=3–2) raio $\sim$ 0.67. This value is close to that interaction regions in our data. This result might imply that the interaction of SNR with the molecular cloud enhances the CI abundance.

4.4.4 Comparison between the CI ($^3P_1$–$^3P_0$) and CO (J=3–2) column densities

We compare the CI and CO column densities. We assume that both lines are optically thin, and use the LTE (local thermodynamical equilibrium) method. The optical depth is expressed as

$$\tau_\nu = -\ln\left\{1 - \frac{T_{\rm mb}}{f(J_\nu(T_{\rm ex}) - J_\nu(T_{\rm bg}))}\right\}$$

where J_ν is the effective radiation source temperature

$$J_\nu(T) = \frac{h\nu/k}{\exp(h\nu/kT) - 1}$$

and $T_{\rm bg}$ is the background radiation temperature. f is the beam filling factor. Since we have CO (J=3–2) data with the high spatial resolution obtained by using the JCMT 15 m telescope (see Chapter 2), we can estimate the beam filling factor of the shock region in the observations with the Mt. Fuji submillimeter-wave telescope by comparing the two data sets. The JCMT data shows $T_{\rm mb}$(CO) = 35 K, and the Mt. Fuji telescope data shows $T_{\rm mb}$(CO) = 11 K in the same region. Therefore, the beam filling factor is estimated to be $f \sim 0.3$.

The total beam-averaged column densitity of CI can be expressed as

$$N({\rm CI}) = \frac{8\pi k\nu^2}{3hc^3 A_{10} 3\exp(-h\nu_{10}/kT_{\rm ex})} Z(T_{\rm ex}) \int T_{\rm mb}(v)dv \ {\rm cm}^{-2}$$

where A_{10} is the Einstein A cofficience (see Table 4.5) and Z($T_{\rm ex}$) is the ground state parition function for the CI as

$$Z(T_{\rm ex}) = 1 + 3\ e^{(-h\nu_{10}/kT_{\rm ex})} + 5\ e^{(-h\nu_{21}/kT_{\rm ex})}$$

TABLE 4.5

CI trandistion data

i	j	A_{ij} [s^{-1}]	ν_{ij} [GHz]
$^3P_1$	$^3P_0$	7.93×10^{-8}	492.1612
$^3P_2$	$^3P_1$	2.68×10^{-7}	809.3432

Note.— A coefficients are from Nussbaumer (1971)

The column density of CO can be expressed as

$$N(\mathrm{CO}) = \frac{3k^2}{8\pi^3 h} \frac{1}{\mu^2 B\nu J} T_{\mathrm{ex}} e^{\frac{hB(J+1)J}{kT_{\mathrm{ex}}}} \int T_{\mathrm{mb}} dv \frac{\tau}{1-e^{-\tau}} \ \mathrm{cm}^{-2}$$

We assume that the CI-emitting gas and the CO-emitting gas has the same excitation temperature. As it was used at Chapter 3, the gas kinetic temperature of the SNR-cloud interaction region is $T_{\mathrm{kin}} \sim 80$K. The excitation temperature of the gas associated with HII regions, W51A and W51B, are 100 K and 50 K, respectively (Jaffe et al. 1989; Koo et al. 1999). Besides, the integrated intensity used only the wing component of the broad emission.

For W44, the derived parameter are listed in Tables 4.6. the $N(\mathrm{CI})/N(\mathrm{CO})$ column density ratio is $\sim 1.3 - 1.7$ in the SNR-cloud interaction region of W44. The unrelated cloud with W44 (outside) cannot be estimated the column density of CO, since CO is optically thick in low excitation temperature. For W51 compex region, the derived parameter are listed in Tables 4.7. It is found that the $N(\mathrm{CI})/N(\mathrm{CO})$ column density ratio are $\sim 0.3 - 0.4$ in the W51A HII region and the W51B HII region. These value are similar to typical that in dense interstellar clouds (e.g. Phillips & Huggins 1981). On the other hand, the $N(\mathrm{CI})/N(\mathrm{CO})$ ratio is ~ 1.4 in the SNR-cloud interaction region of W51.

In the SNR-cloud interaction region, the $N(\mathrm{CI})/N(\mathrm{CO})$ ratio is over a factor of five higher than that in dense interstellar clouds. If our assumption is appropriate, this results are observational evidence of the enhancement of CI abundance in the the SNR-cloud interaction region following IC443. Since CO may be opaque, these values give the upper limit. In order to estimate the optical depth of CO, it is necessary

TABLE 4.6

Estimitaed parameters of CI and CO toward W44

Position	Tex K	τ(CI)	$\int T_{\rm mb}$(CI)dv K km^{-2}	$\int T_{\rm mb}$(CO)dv K km^{-2}	N(CI) 10^{17} cm^{-2}	N(CO) 10^{17} cm^{-2}	$\frac{N(\rm CI)}{N(\rm CO)}$
SNR inner	80	0.26	20.5	28.1	3.01	2.31	1.3
SNR edge	80	0.26	17.0	21.4	3.82	2.26	1.73
SNR outer	10	1.97	16.8	47.7	2.18	N/A	N/A

TABLE 4.7

Estimitaed parameters of CI and CO toward W51

Position	Tex K	τ(CI)	$\int T_{\rm mb}$(CI)dv K km^{-2}	$\int T_{\rm mb}$(CO)dv K km^{-2}	N(CI) 10^{17} cm^{-2}	N(CO) 10^{17} cm^{-2}	$\frac{N(\rm CI)}{N(\rm CO)}$
W51B(OH maser)	80	0.24	18.2	22.5	2.7	1.9	1.43
W51B(HII region)	50[b]	0.30	10.0	41.1	1.4	4.2	0.32
W51A(HII region)	100[a]	0.29	24.6	87.8	3.7	16.2	0.23

Note.— a : Jaffe et al. 1989, b : Koo et al. 1999)

to observe ^{13}CO and C^{18}O, which is optically thin. Moreover, it is also important to observe CI ($^3P_2$–$^3P_1$) emission in order to characterize the physical condition of the CI–emitting region.

4.5 Conclusion

We reported mapping observations of CO (J=3–2) at 345.796 GHz and CI ($^3P_1$–$^3P_0$) at 492.161 GHz toward the four SNRs, IC443, W28, W44, and W51, by using Mt. Fuji submillimeter–wave telescope. The CI ($^3P_1$–$^3P_0$) emission was not detected in IC 443. For the other three SNRs, CI ($^3P_1$–$^3P_0$) was detected, and its distribution is similar to that of the CO (J=3–2) emission. It is clear that the OH (1720 MHz) maser spots, which trace the interaction between SNR and the molecular cloud, are located

at the cloud edge. In the region where SNR interacts with the molecular cloud, the CI ($^3P_1$–$^3P_0$)/ CO (J=3–2) ratio is high, while the ratio in the other regions is low. This result might imply that the interaction of SNR with the molecular cloud enhances the CI abundance.

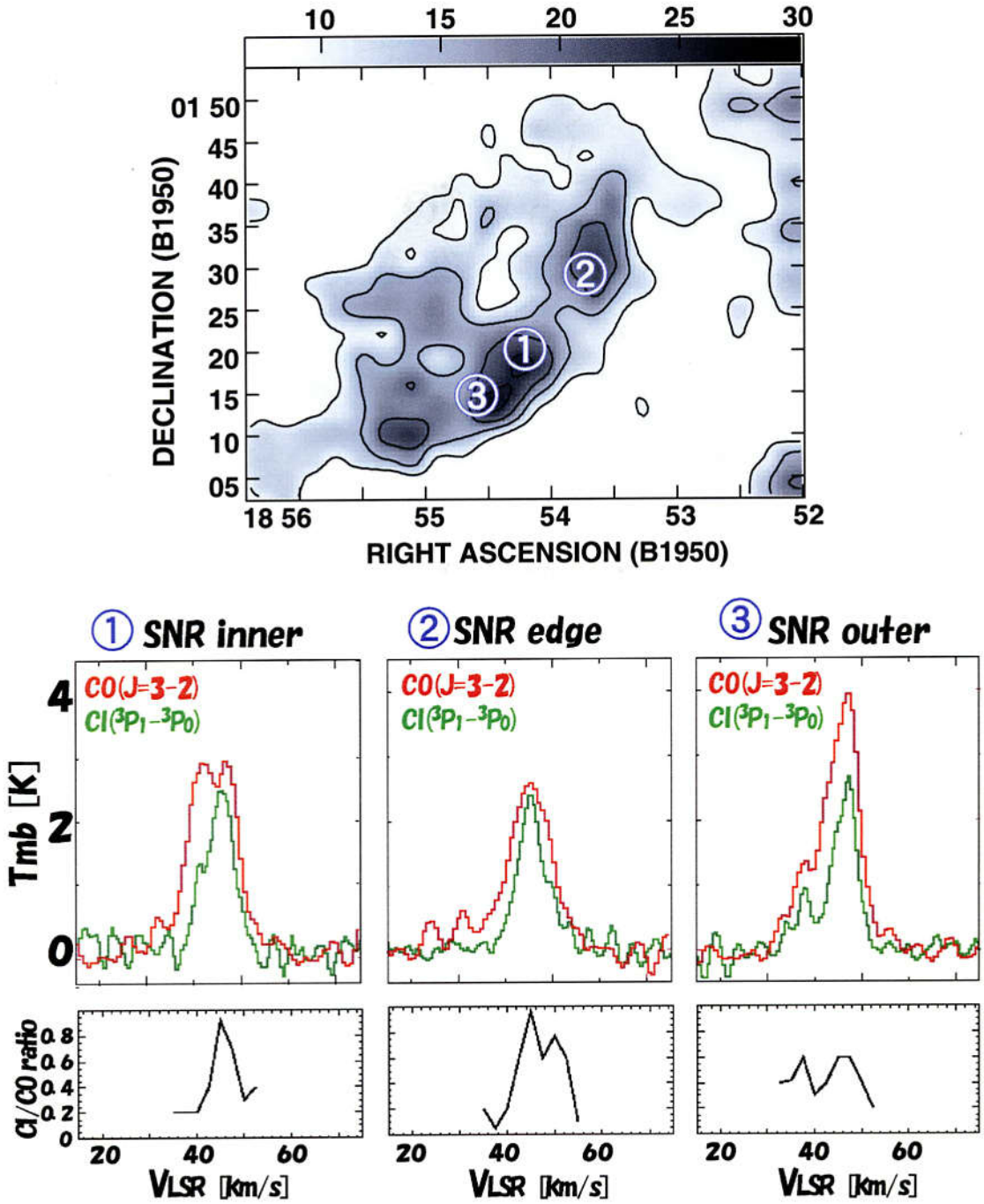

Fig. 4.3.— Upper panel : Integrated intensity map of the CI ($^3P_1$–$^3P_0$)emission of the SNR W44. The integration was made between $V_{\rm LSR}$ = 20 km s^{-1} and 60 km s^{-1}. Top–side of Lower panel : the line profiles of the composite spectrum averaged over each clump. Bottom–side of Lower panels : the intensity ratio of CI ($^3P_1$–$^3P_0$)to CO (J=3–2) for each clump.

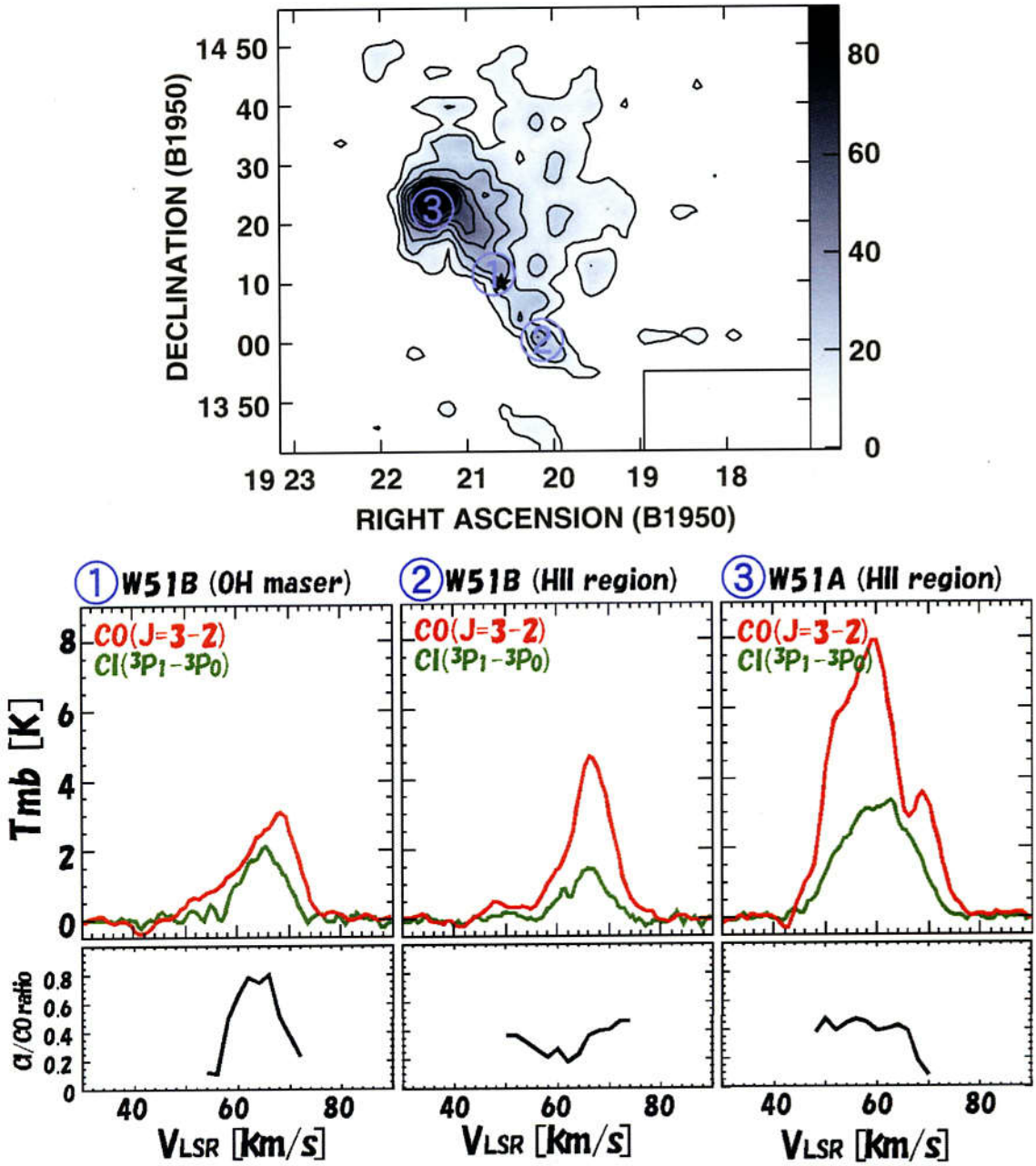

Fig. 4.4.— Upper panel : Integrated intensity map of the CI ($^3P_1$–$^3P_0$)emission of the W51 complex region. The integration was made between $V_{\rm LSR}$ = 30 km s^{-1} and 80 km s^{-1}. Top–side of Lower panel : the line profiles of the composite spectrum averaged over each clump. Bottom–side of Lower panels : the intensity ratio of CI ($^3P_1$–$^3P_0$)to CO (J=3–2) for each clump.

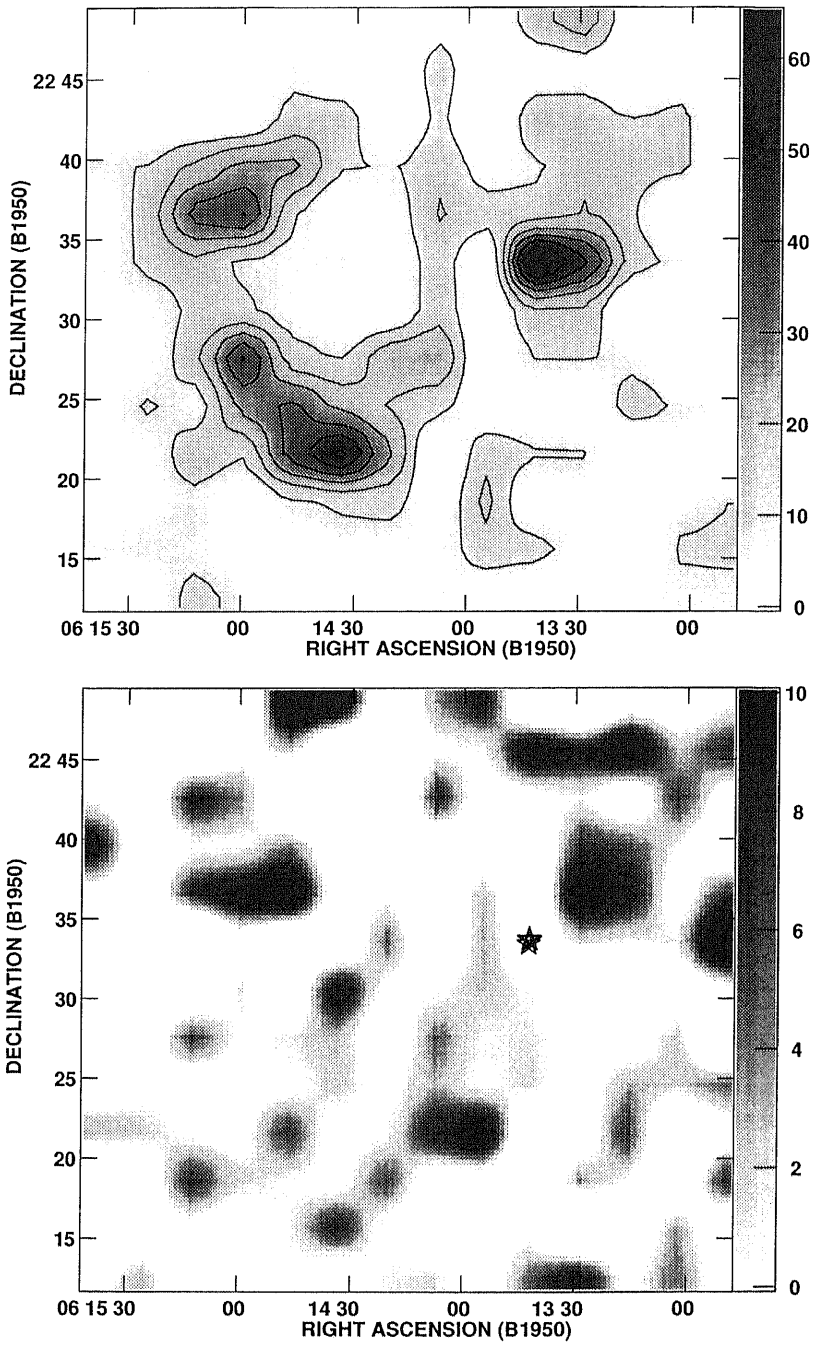

Fig. 4.5.— Upper panel: Integrated intensity map of the CO (J=3–2) emission at 345.796 GHz toward IC 443. The contour interval is 8.6 K km s^{-1}. Lower panel: Integrated intensity map of the CI ($^3P_1$–$^3P_0$)emission at 492.161 GHz toward IC 443. The integration was made between $V_{\rm LSR} = -50$ km s^{-1} and 20 km s^{-1}. The stars mark the OH (1720 MHz) maser spots by Claussen et al. (1997).

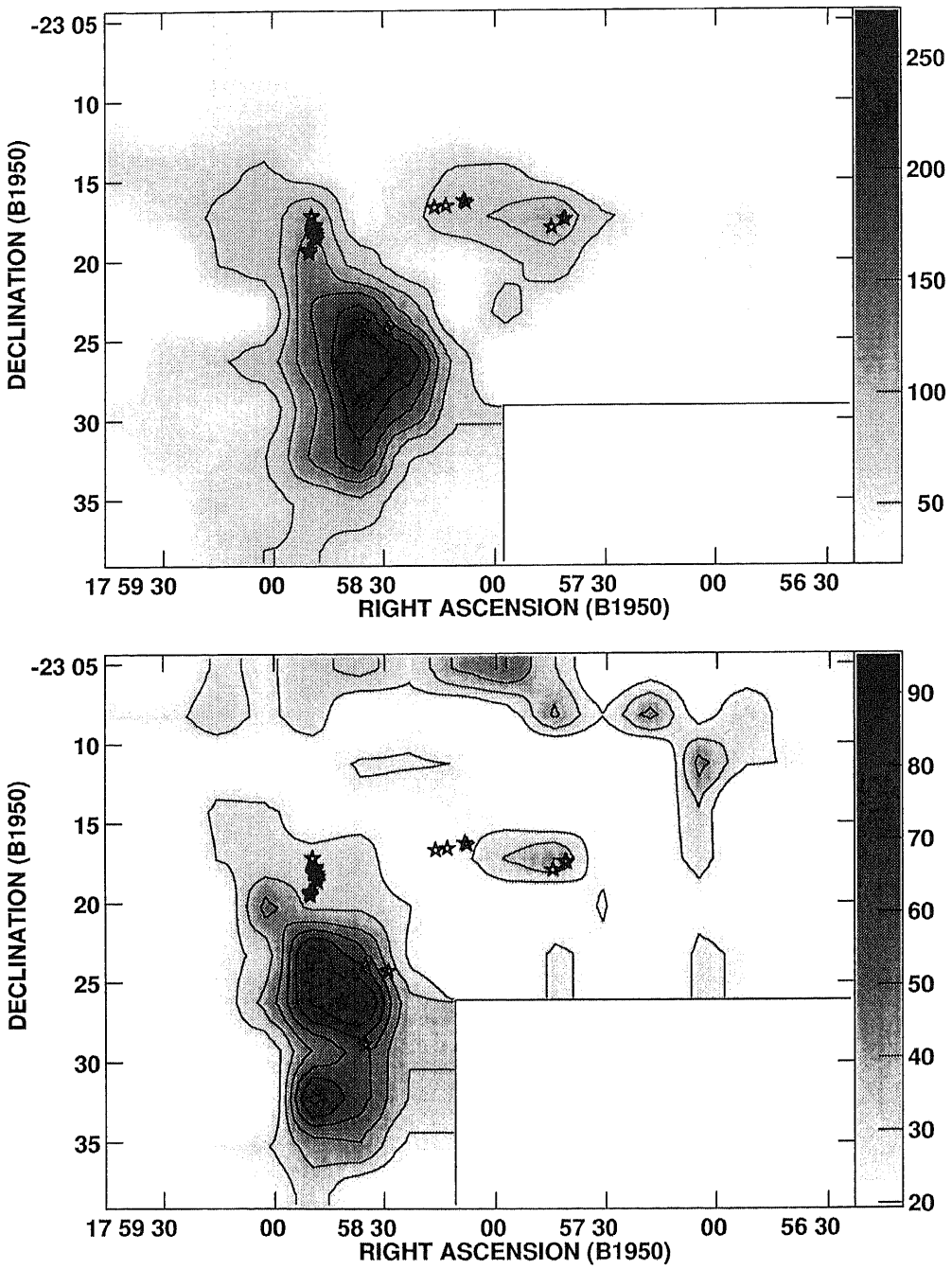

Fig. 4.6.— Upper panel: Integrated intensity map of the CO (J=3–2) emission at 345.796 GHz toward W28. The contour interval is 31 K km s^{-1} starting from 61 K km s^{-1}. Lower panel: Integrated intensity map of the CI ($^3P_1$–$^3P_0$)emission at 492.161 GHz toward W28. The contour interval is 9.7 K km s^{-1} starting from 29 K km s^{-1}. The integration was made between $V_{\rm LSR}$ = −30 km s^{-1} and 40 km s^{-1}. The stars mark the OH (1720 MHz) maser spots by Claussen et al. (1997).

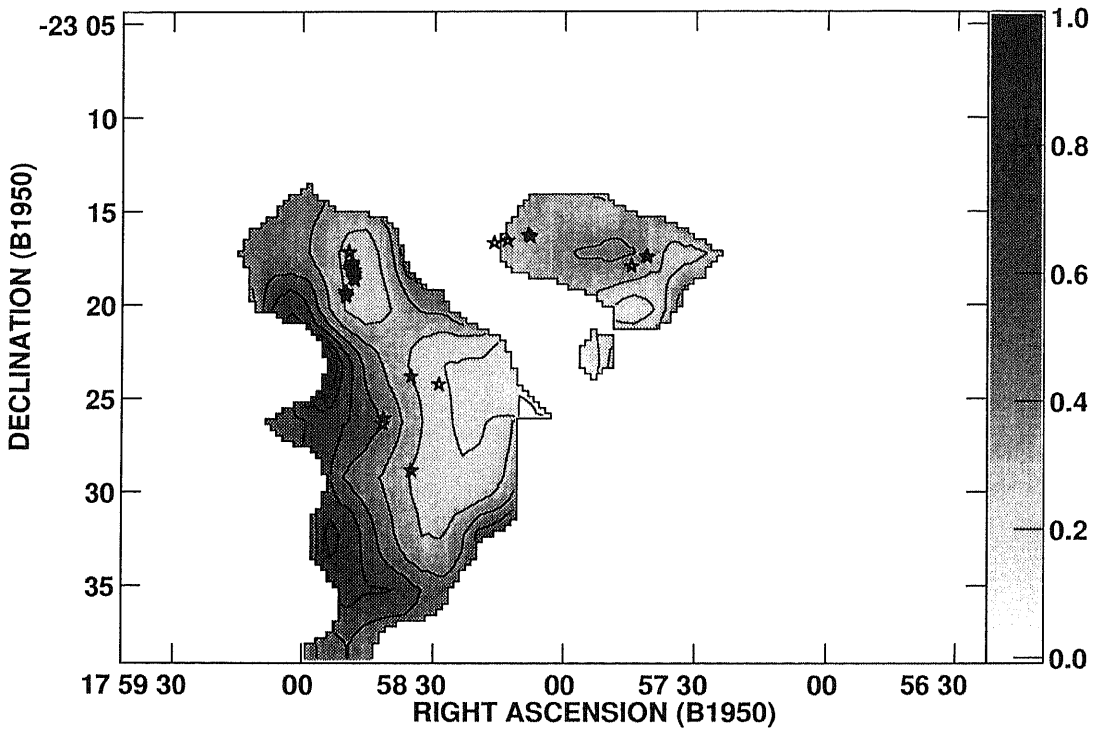

Fig. 4.7.— CI ($^3P_1$–$^3P_0$)/ CO (J=3–2) integrated intensity ratio map toward W28. The contour intervals are 0.1. The integration was made between $V_{\rm LSR}$ = −30 km s^{-1} and 40 km s^{-1}. The stars mark the OH (1720 MHz) maser spots by Claussen et al. (1997).

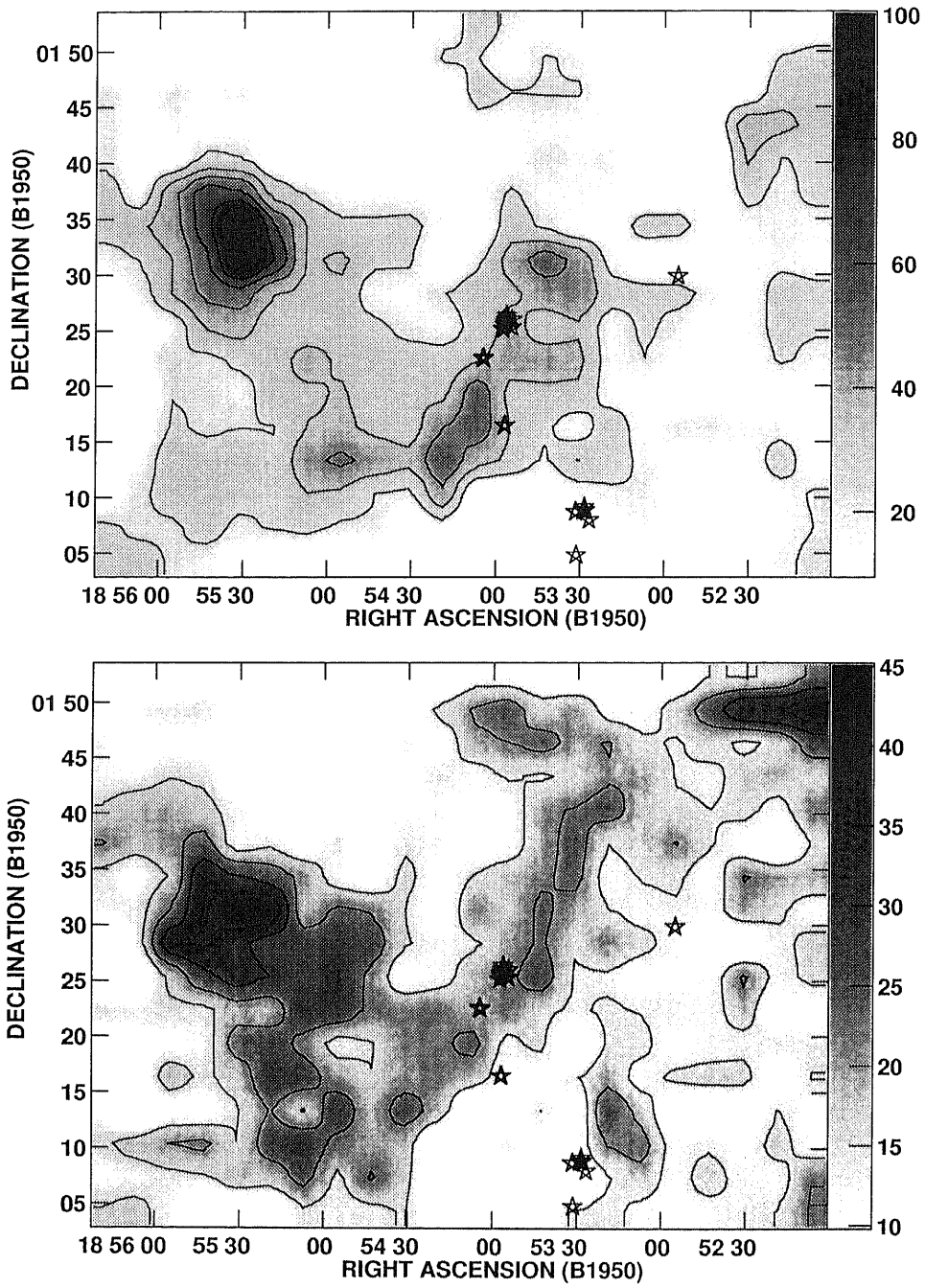

Fig. 4.8.— Upper panel: Integrated intensity map of the CO (J=3–2) emission at 345.796 GHz toward W44. The contour interval is 13 K km s^{-1} starting from 21.8 K km s^{-1}. Lower panel: Integrated intensity map of the CI ($^3P_1$–$^3P_0$) emission at 492.161 GHz toward W44. The contour interval is 7.7 K km s^{-1} starting from 15.4 K km s^{-1}. The integration was made between $V_{\rm LSR}$=20 km s^{-1} and 60 km s^{-1}. The stars mark the OH (1720 MHz) maser spots by Claussen et al. (1997).

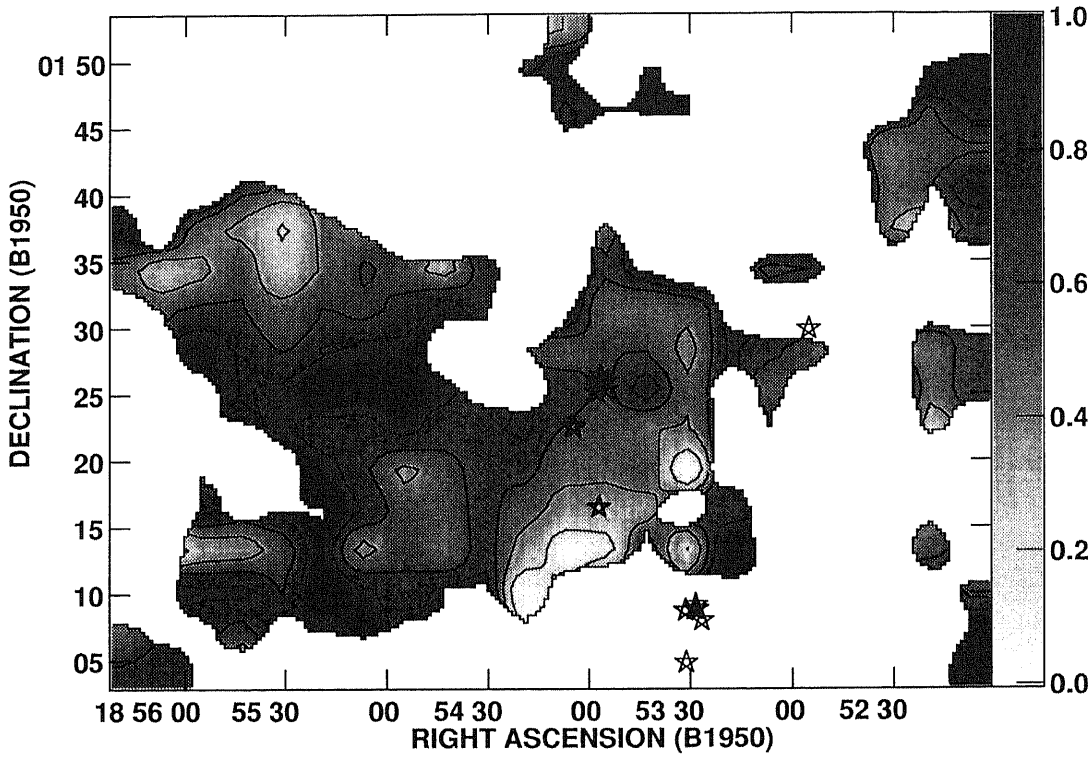

Fig. 4.9.— CI ($^3P_1$–$^3P_0$)/CO (J=3–2) integrated intensity ratio map toward W44. The contour interval is 0.2. The integration was made between $V_{\rm LSR}$=20 km s^{-1} and 60 km s^{-1}. The stars mark the OH (1720 MHz) maser spots by Claussen et al. (1997).

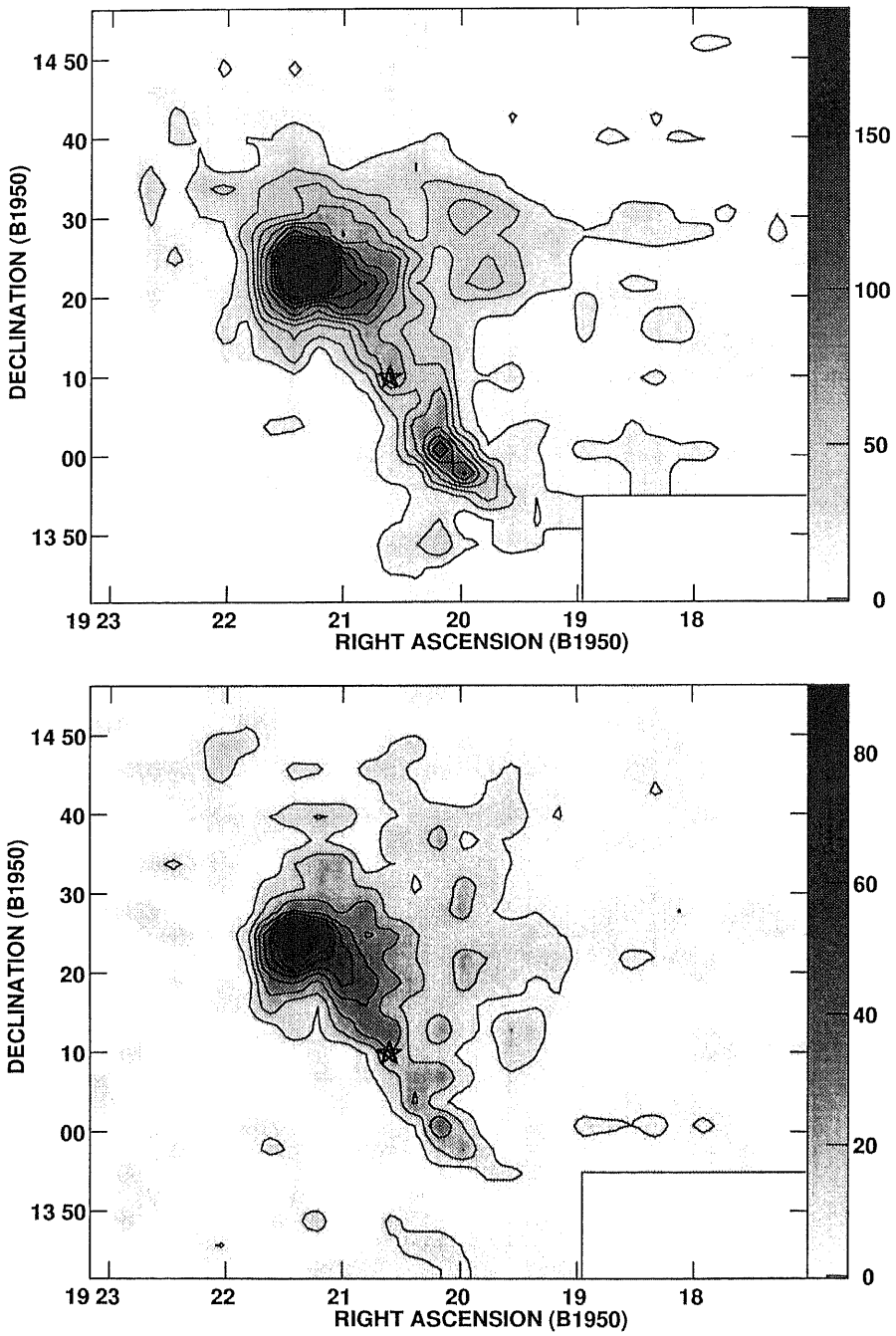

Fig. 4.10.— Upper panel: Integrated intensity map of the CO (J=3–2) emission at 345.796 GHz toward W51. The contour interval is 15.6 K km s^{-1}. Lower panel: Integrated intensity map of the CI ($^3P_1$–$^3P_0$) emission at 492.161 GHz toward W51. The contour interval is 11.0 K km s^{-1}. The integration was made between $V_{\rm LSR}$ =30 km s^{-1} and 80 km s^{-1}. The stars mark the OH (1720 MHz) maser spots by Green et al. (1997).

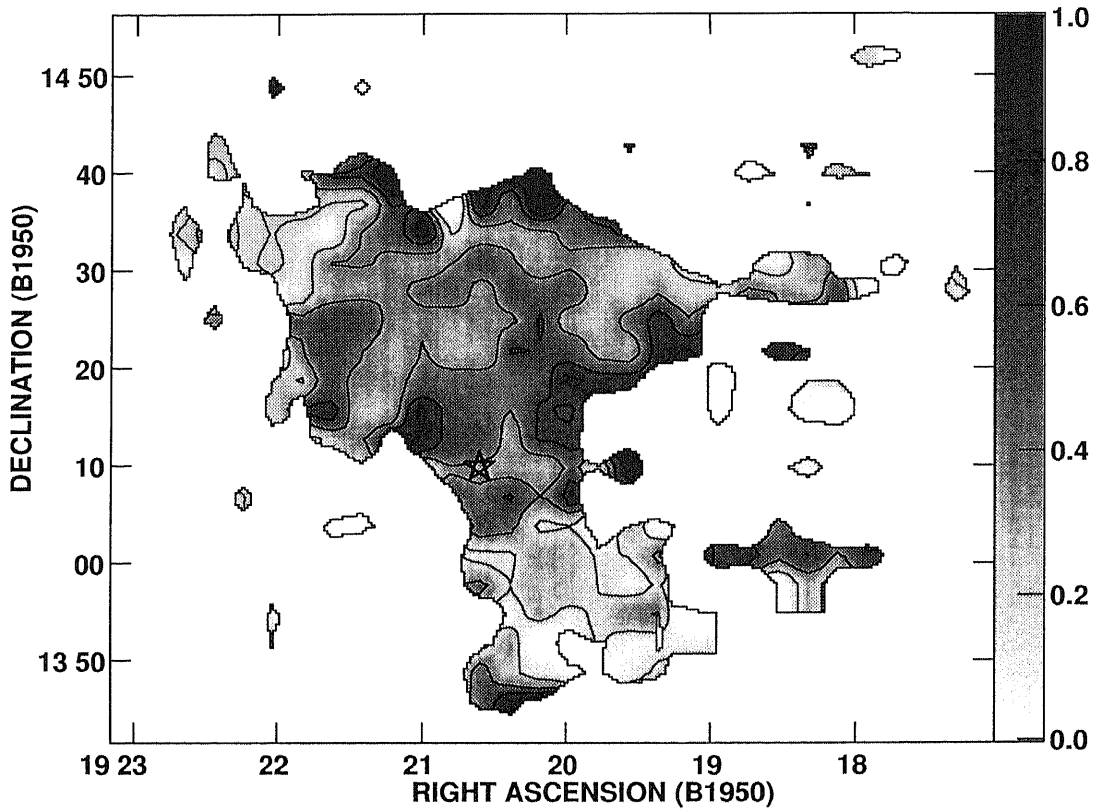

Fig. 4.11.— CI ($^3P_1$–$^3P_0$)/CO (J=3–2) integrated intensity ratio map toward W5 .The contour interval is 0.2. The integration was made between $V_{\rm LSR}$ =30 km s^{-1} and 80 km s^{-1}. The stars mark the OH (1720 MHz) maser spots by Green et al. (1997).

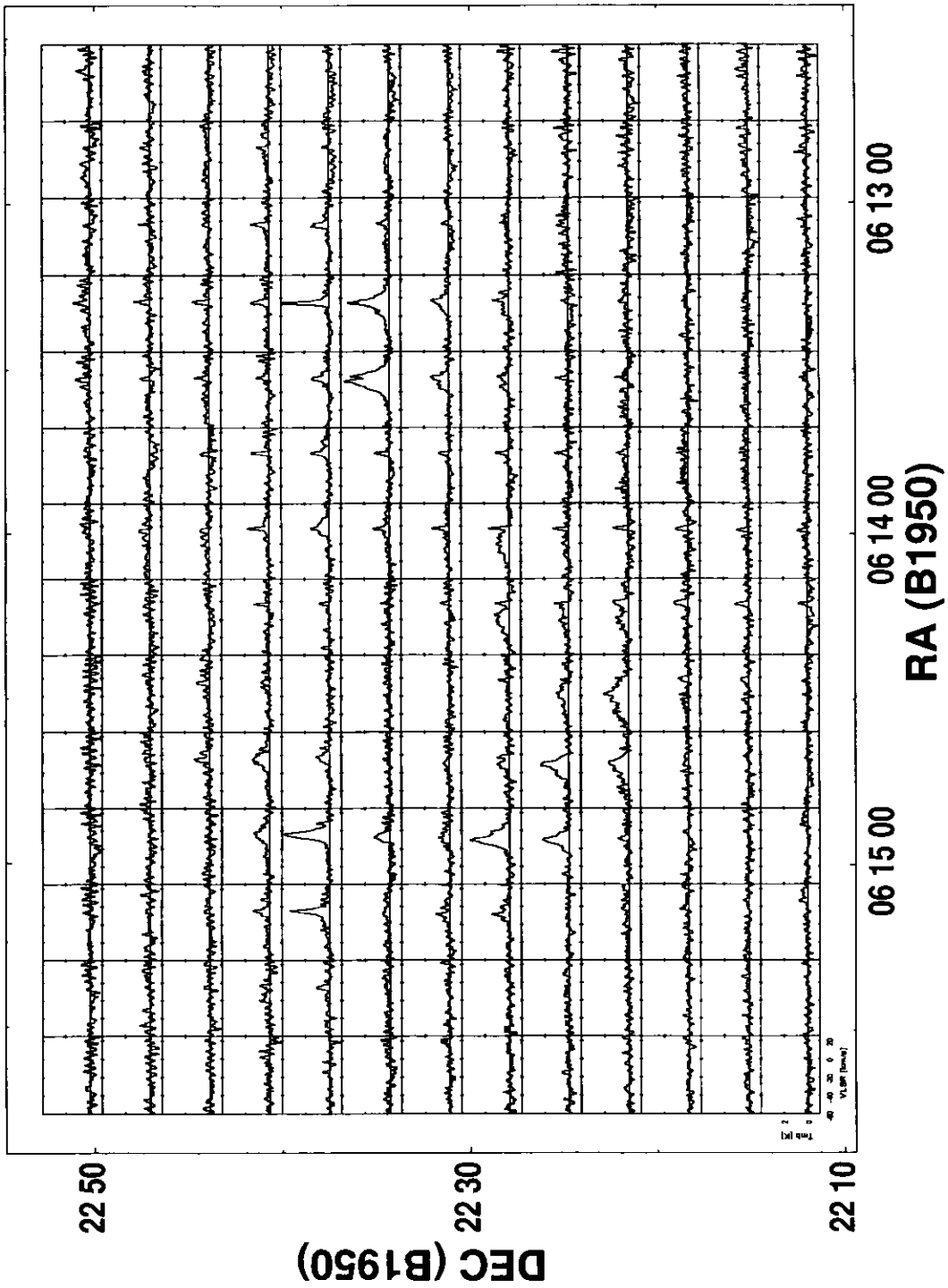

Fig. 4.12.— Profile map of the CO (J=3–2) emission toward IC 443. The velocity scale in each spectrum runs from $V_{\rm LSR}$ = −60 km s^{-1} to 25 km s^{-1} and the temperature scale from $T_{\rm mb}$ = −1 to 4 K.

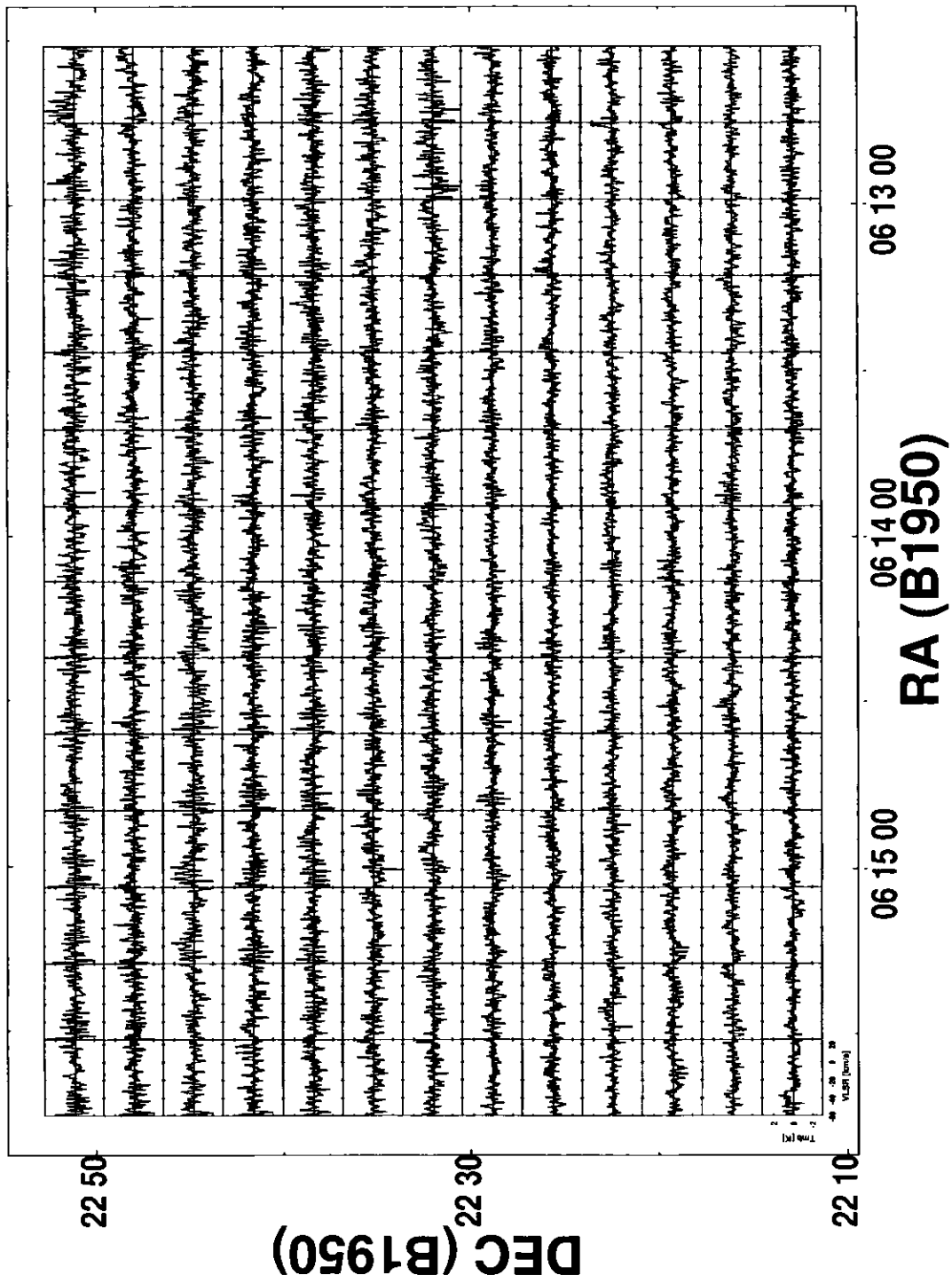

Fig. 4.13.— Profile map of the CI ($^3P_1$–$^3P_0$)emission toward IC 443. The velocity scale in each spectrum runs from $V_{\rm LSR}$ = −40 km s^{-1} to 25 km s^{-1} and the temperature scale from $T_{\rm mb}$ = −3 to 3 K.

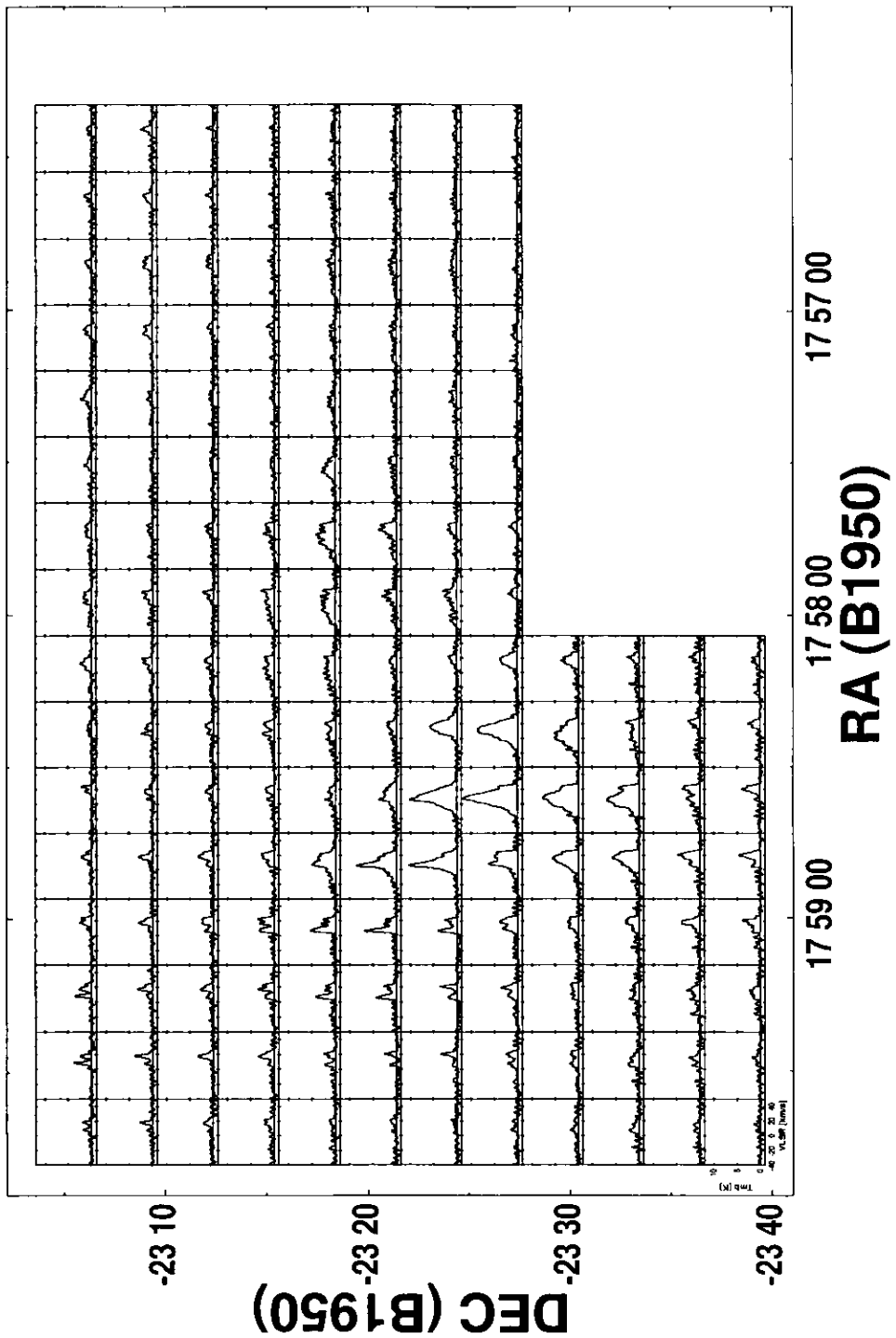

Fig. 4.14.— Profile map of the CO (J=3–2) emission toward W28 SNR. The velocity scale in each spectrum runs from $V_{\rm LSR}$ = −40 km s^{-1} to 50 km s^{-1} and the temperature scale from $T_{\rm mb}$ = −0.5 to 13 K.

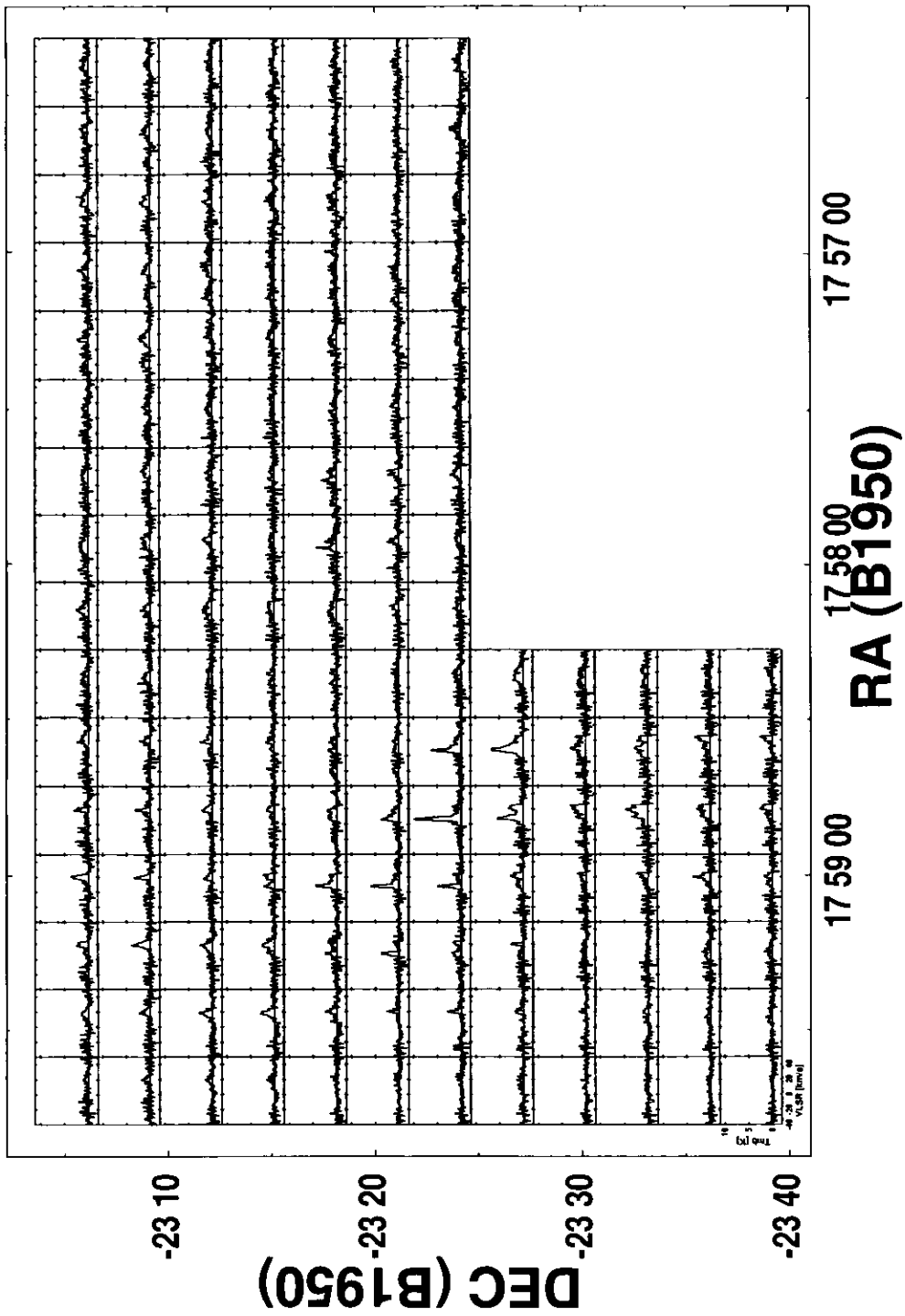

Fig. 4.15.— Profile map of the CI ($^3P_1$–$^3P_0$)emission toward W28. The velocity scale in each spectrum runs from $V_{\rm LSR} = -40$ km s^{-1} to 50 km s^{-1} and the temperature scale from $T_{\rm mb} = -2$ to 12 K.

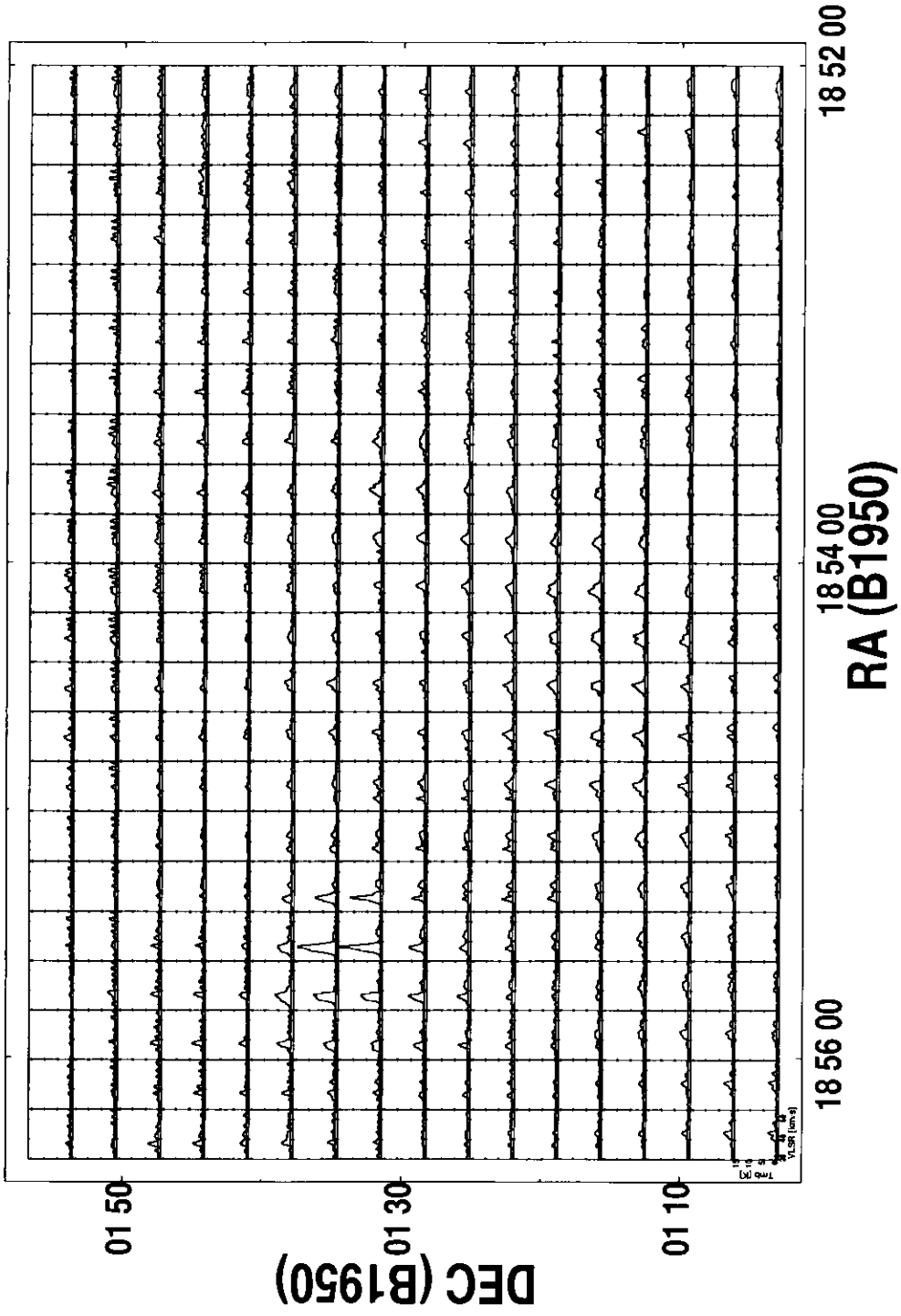

Fig. 4.16.— Profile map of the CO (J=3–2) emission toward W44. The velocity scale in each spectrum runs from $V_{\rm LSR}$ = 20 km s^{-1} to 70 km s^{-1} and the temperature scale from $T_{\rm mb}$ = −1 to 16 K.

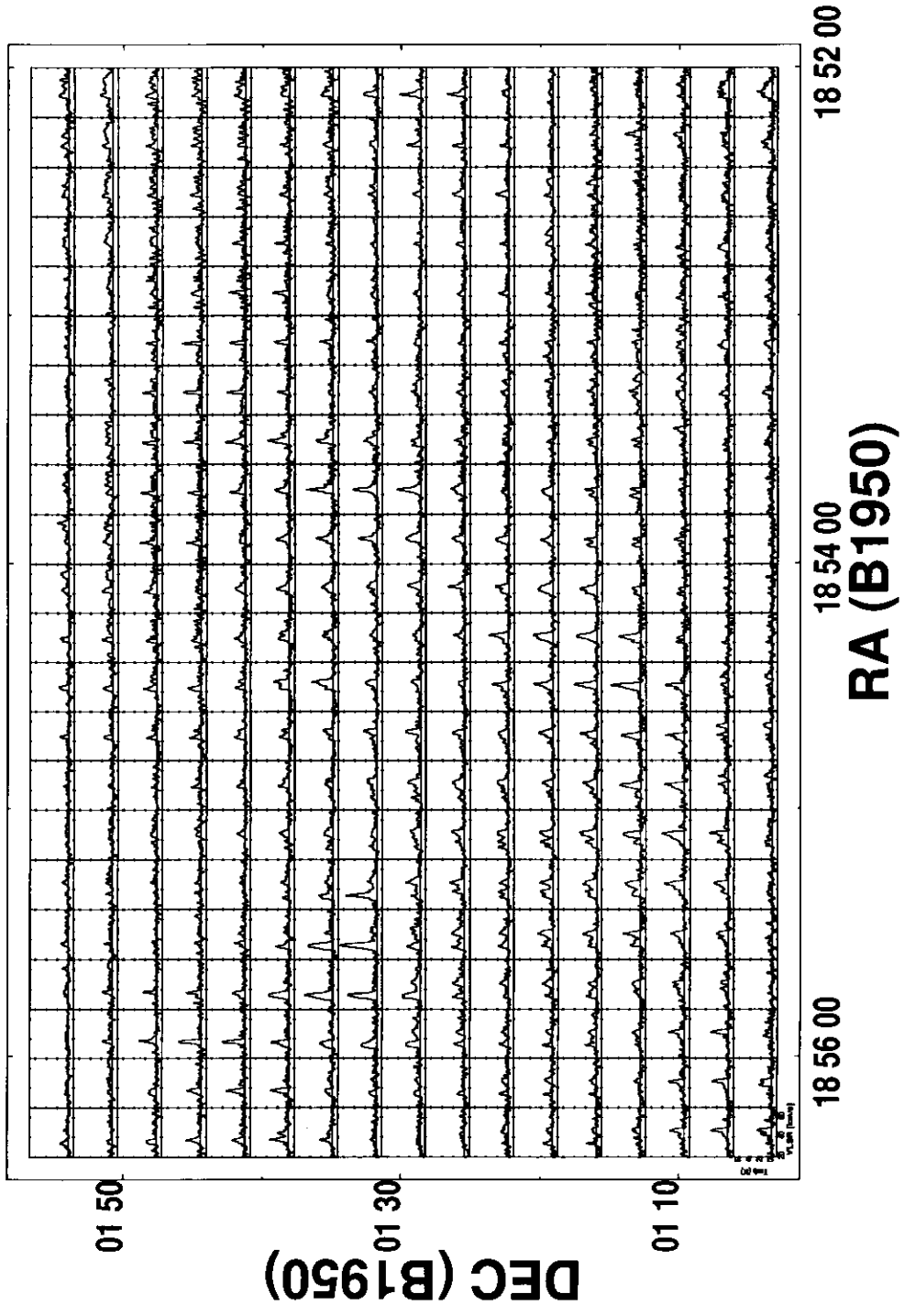

Fig. 4.17.— Profile map of the CI ($^3P_1$–$^3P_0$) emission toward W44. The velocity scale in each spectrum runs from $V_{\rm LSR}$ = 20 km s^{-1} to 70 km s^{-1} and the temperature scale from $T_{\rm mb}$ = −1 to 7 K.

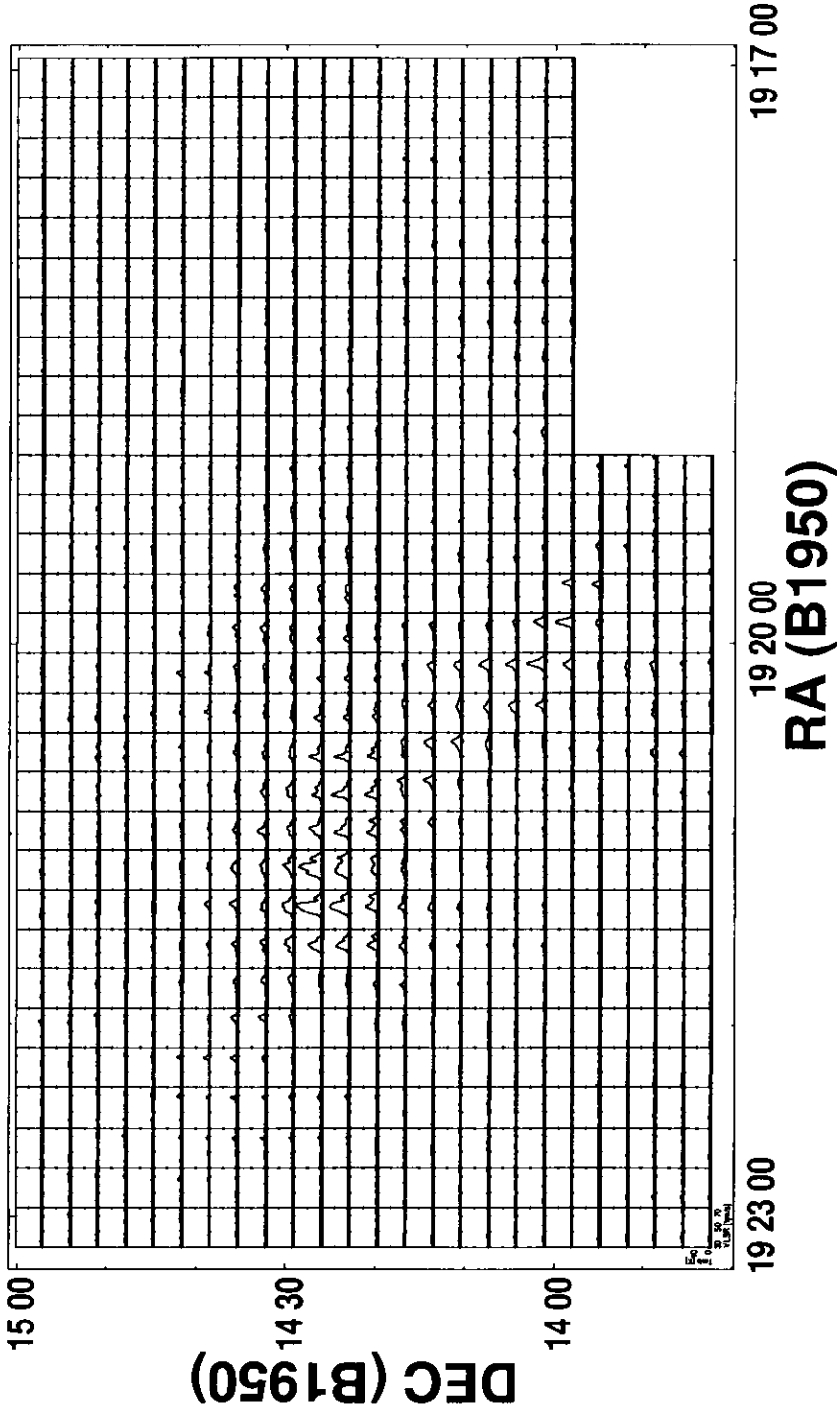

Fig. 4.18.— Profile map of the CO (J=3–2) emission toward W51. The velocity scale in each spectrum runs from $V_{\rm LSR}$ = 30 km s^{-1} to 80 km s^{-1} and the temperature scale from $T_{\rm mb}$ = −1 to 20 K.

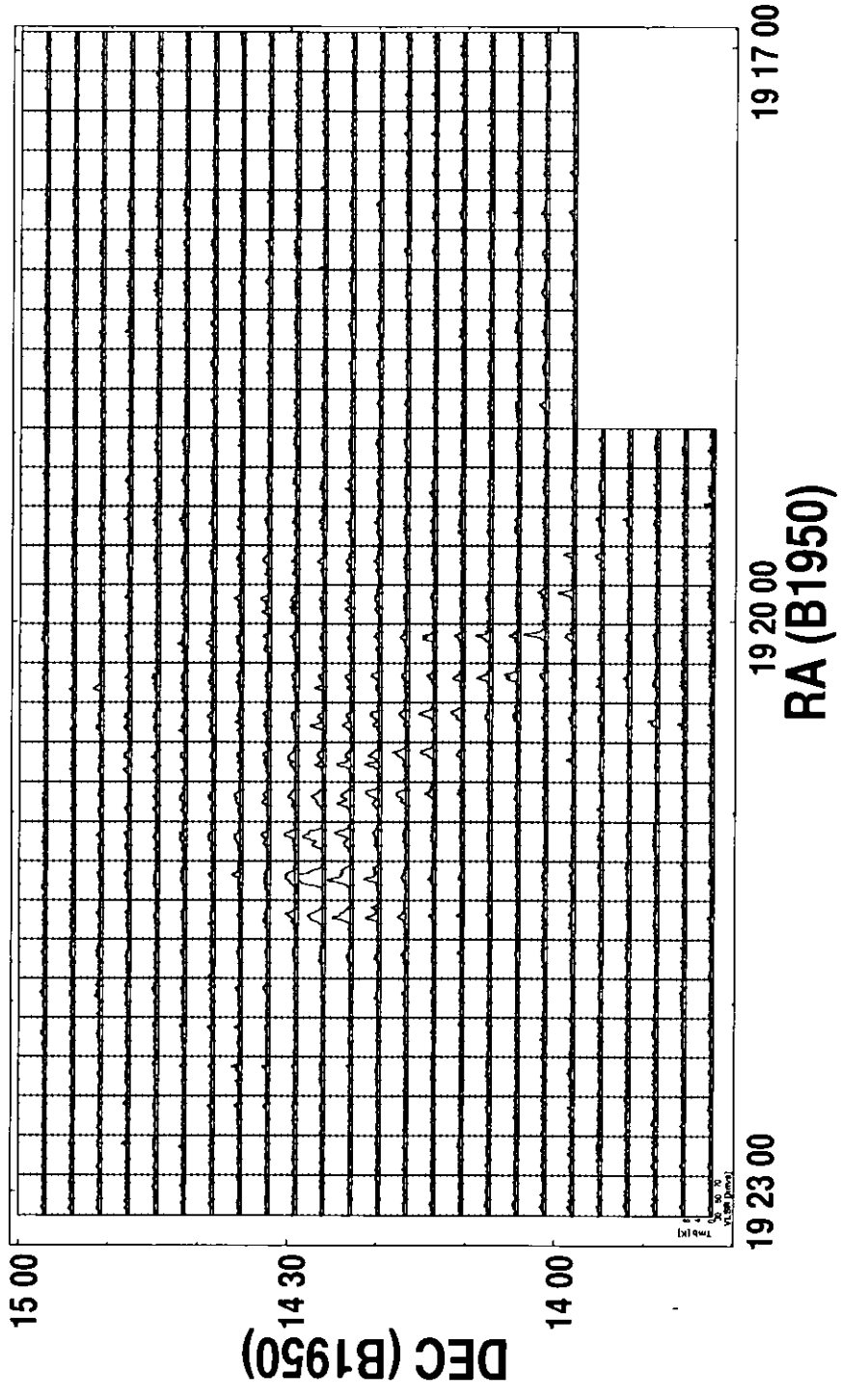

Fig. 4.19.— Profile map of the CI ($^3P_1$–$^3P_0$) emission toward W51. The velocity scale in each spectrum runs from $V_{\rm LSR}$ = 30 km s^{-1} to 80 km s^{-1} and the temperature scale from $T_{\rm mb}$ = −1 to 9 K.

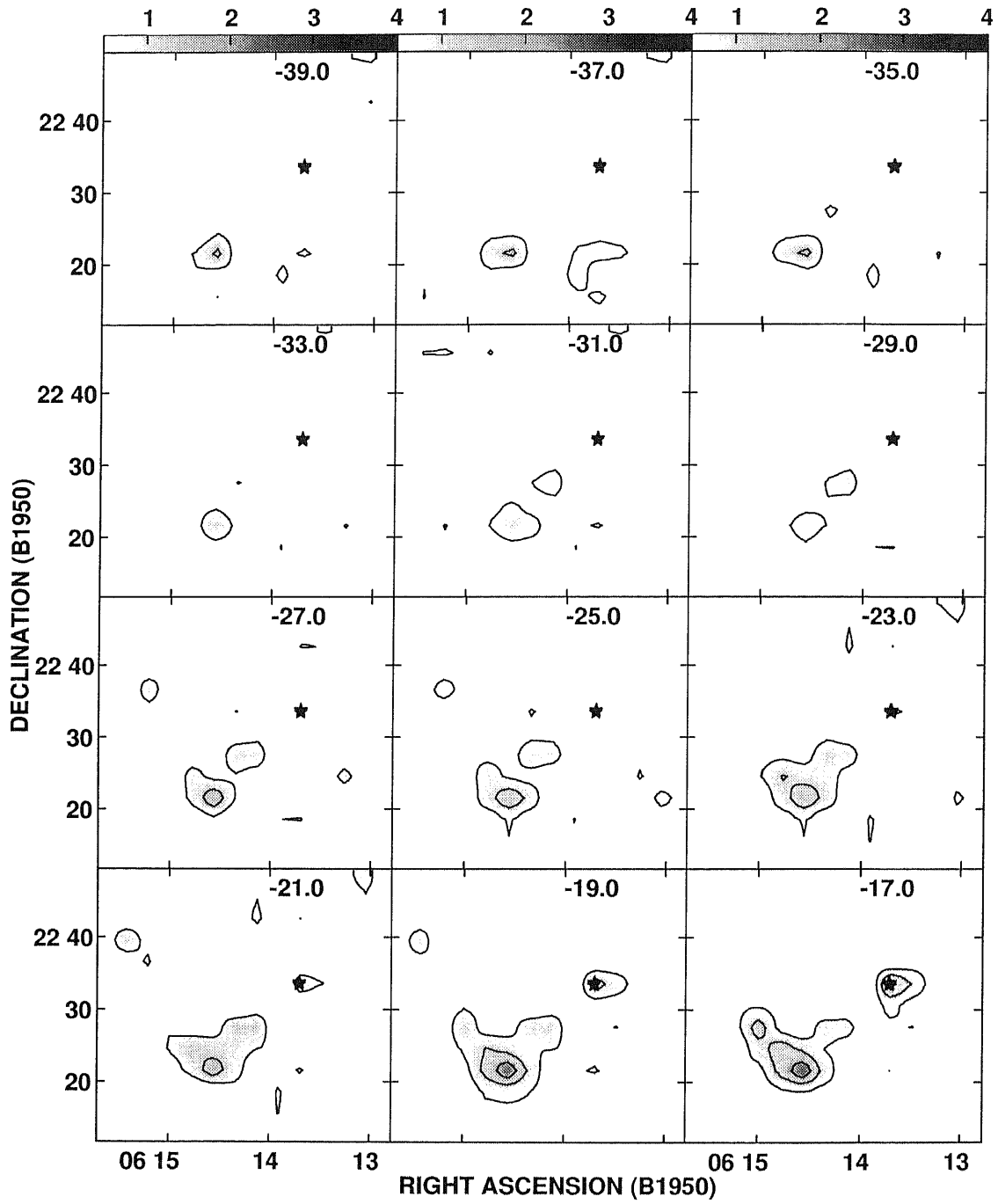

Fig. 4.20.— Part I of Channel maps of the integrated CO (J=3–2) emission at 2 km s^{-1} velocity intervals toward IC 443. The center velocity is labeled at the upper right corner. The contour interval is 0.56 K km s^{-1}.

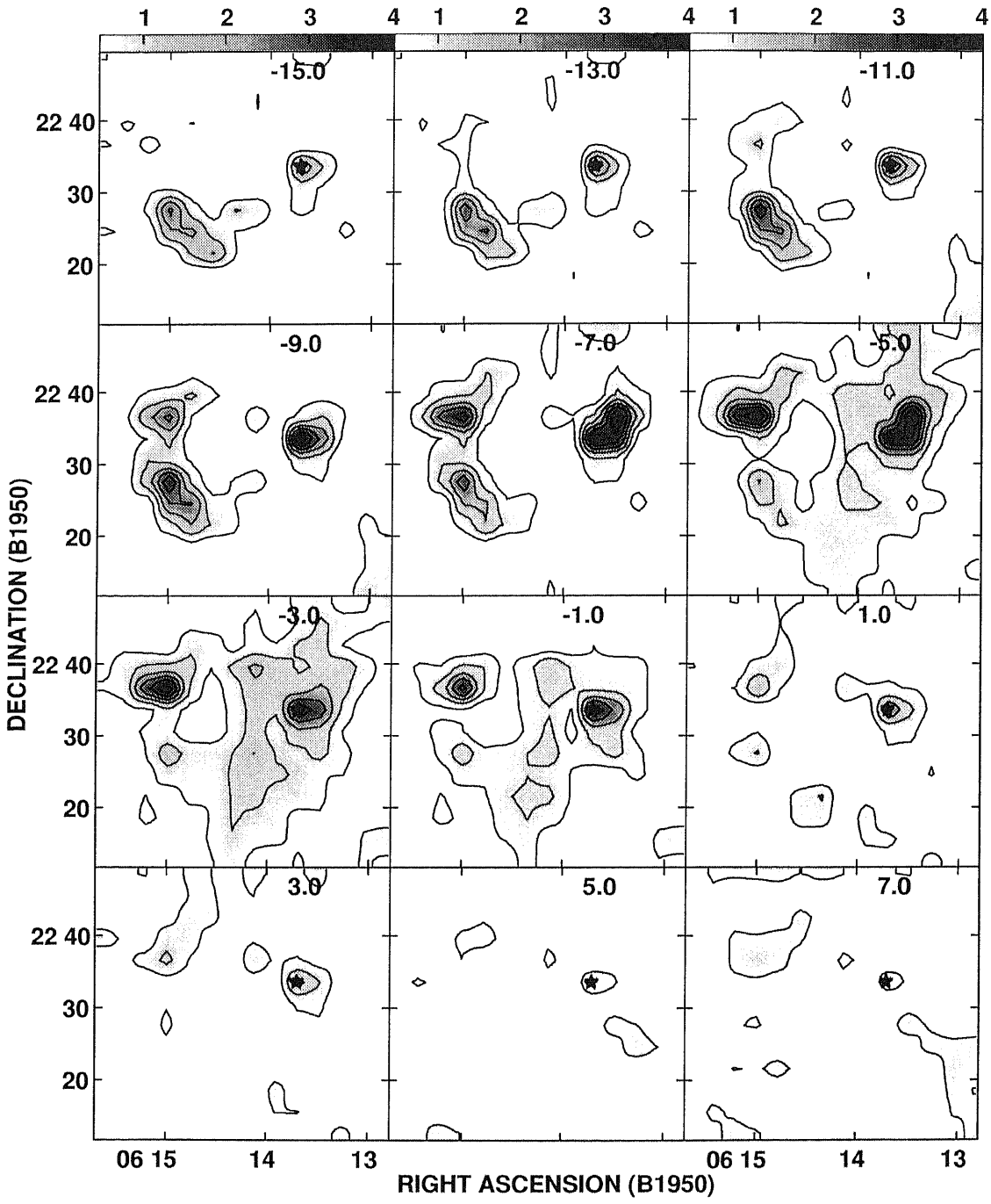

Fig. 4.21.— Part II of Channel maps of the integrated CO (J=3–2) emission toward IC 443.

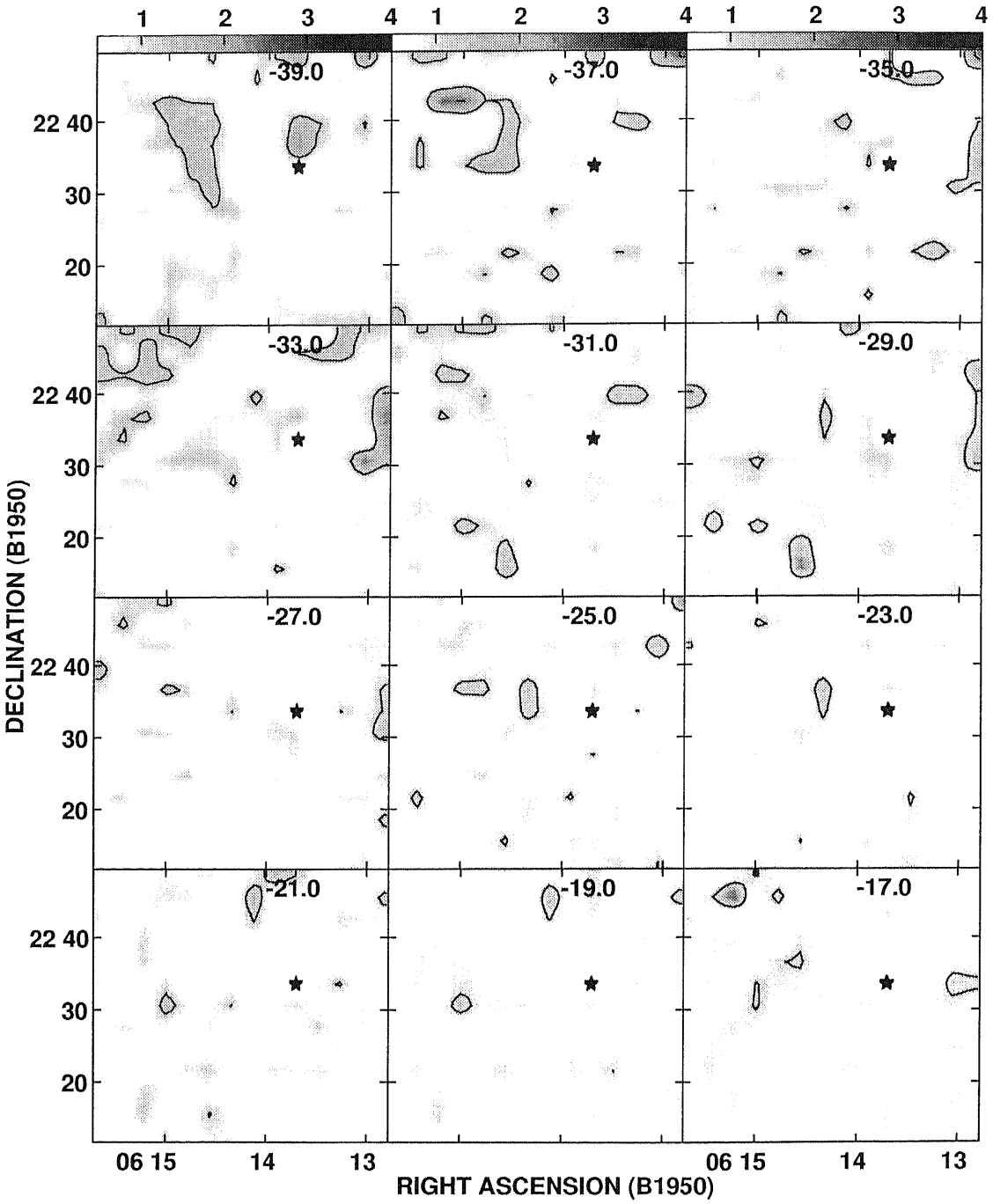

Fig. 4.22.— Part I of Channel maps of the integrated CI ($^3P_1$–$^3P_0$) emission at 2 km s^{-1} velocity intervals toward IC 443. The center velocity is labeled at the upper right corner. The contour interval is 1.16 K km s^{-1}.

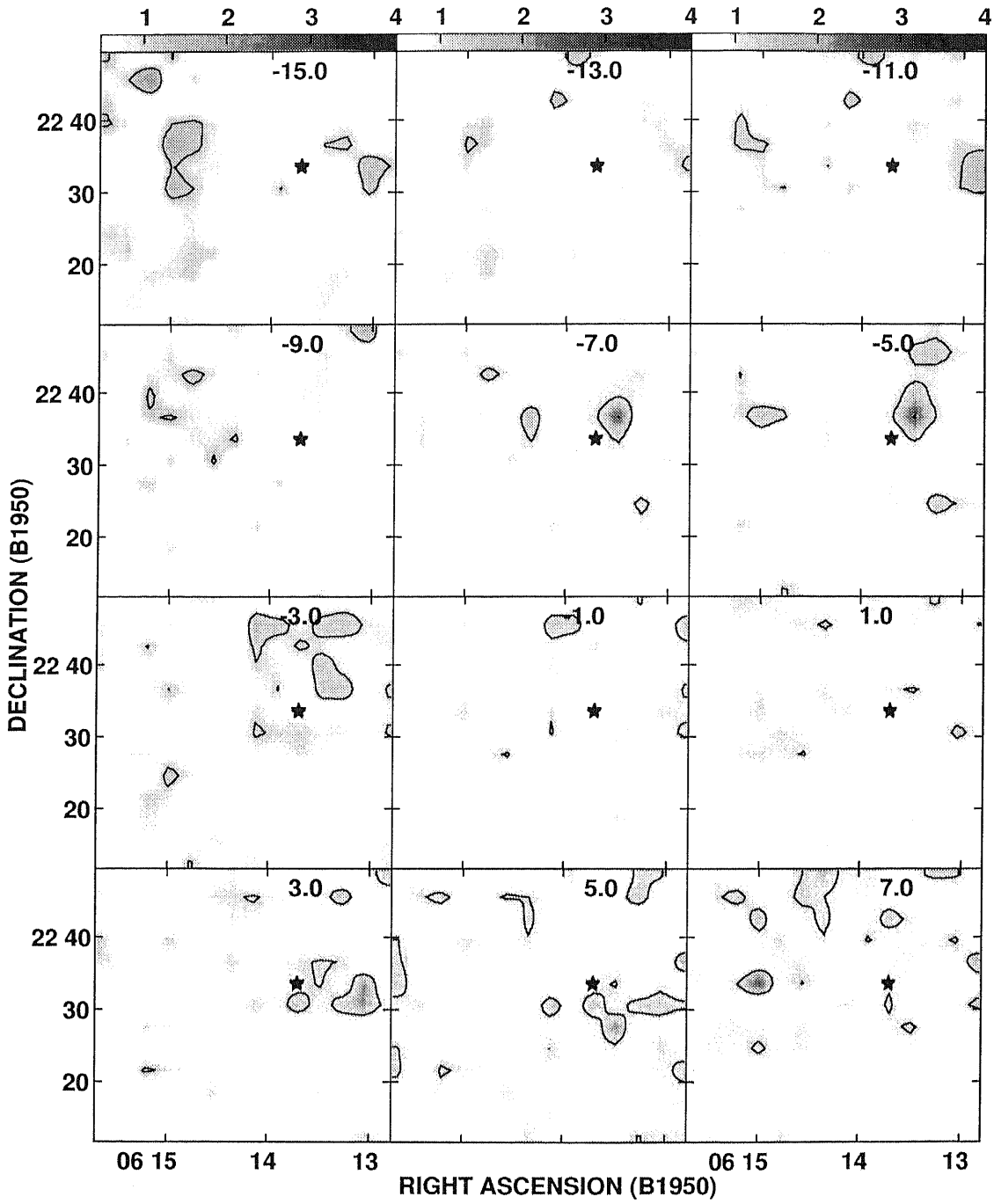

Fig. 4.23.— Part II of Channel maps of the integrated CI ($^3P_1$–$^3P_0$) emission toward IC 443.

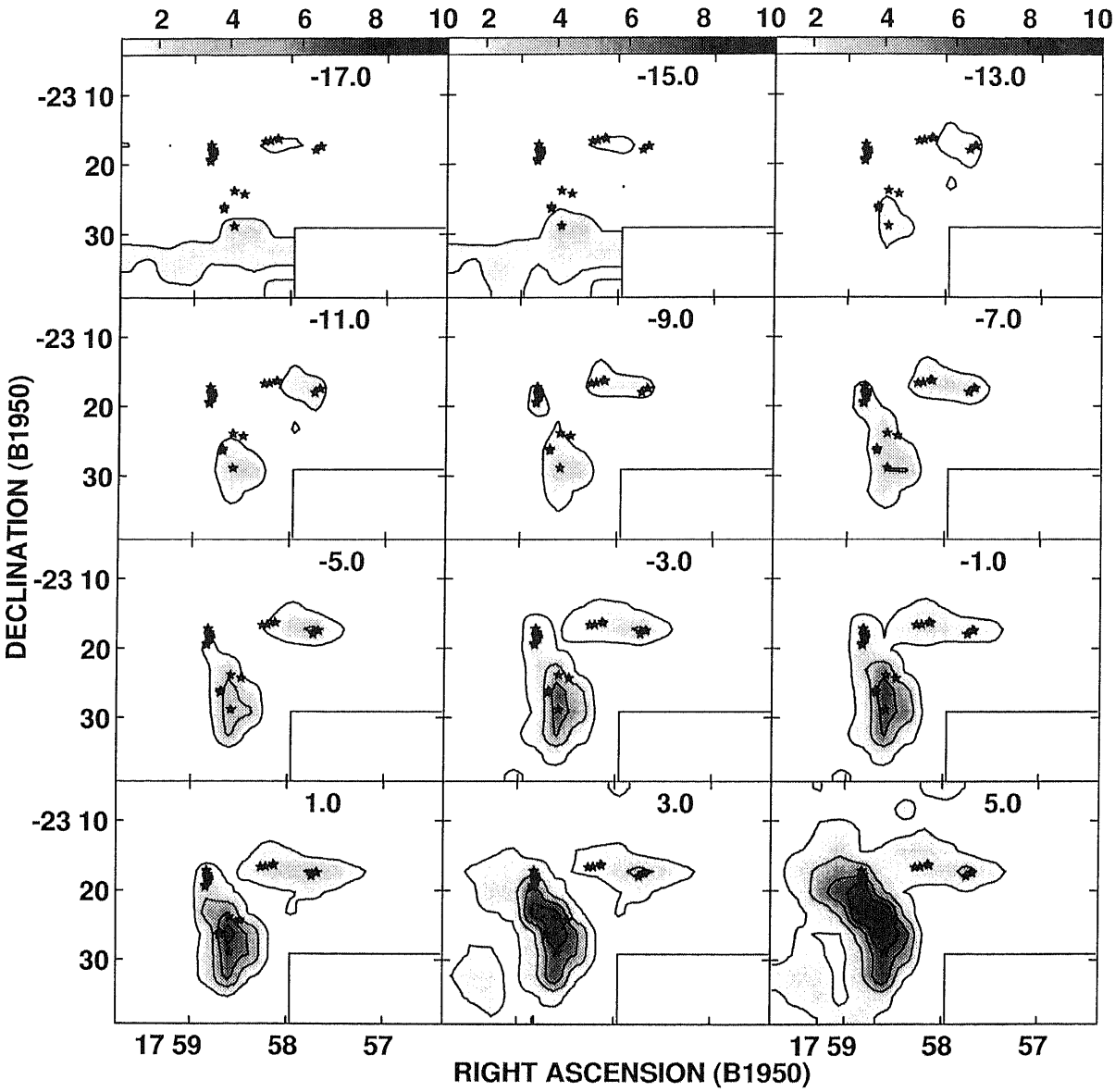

Fig. 4.24.— Part I of Channel maps of the integrated CO (J=3–2) emission at 2 km s^{-1} velocity intervals toward W28. The center velocity is labeled at the upper right corner. The contour interval is 0.81 K km s^{-1} starting from 1.34 K km s^{-1}.

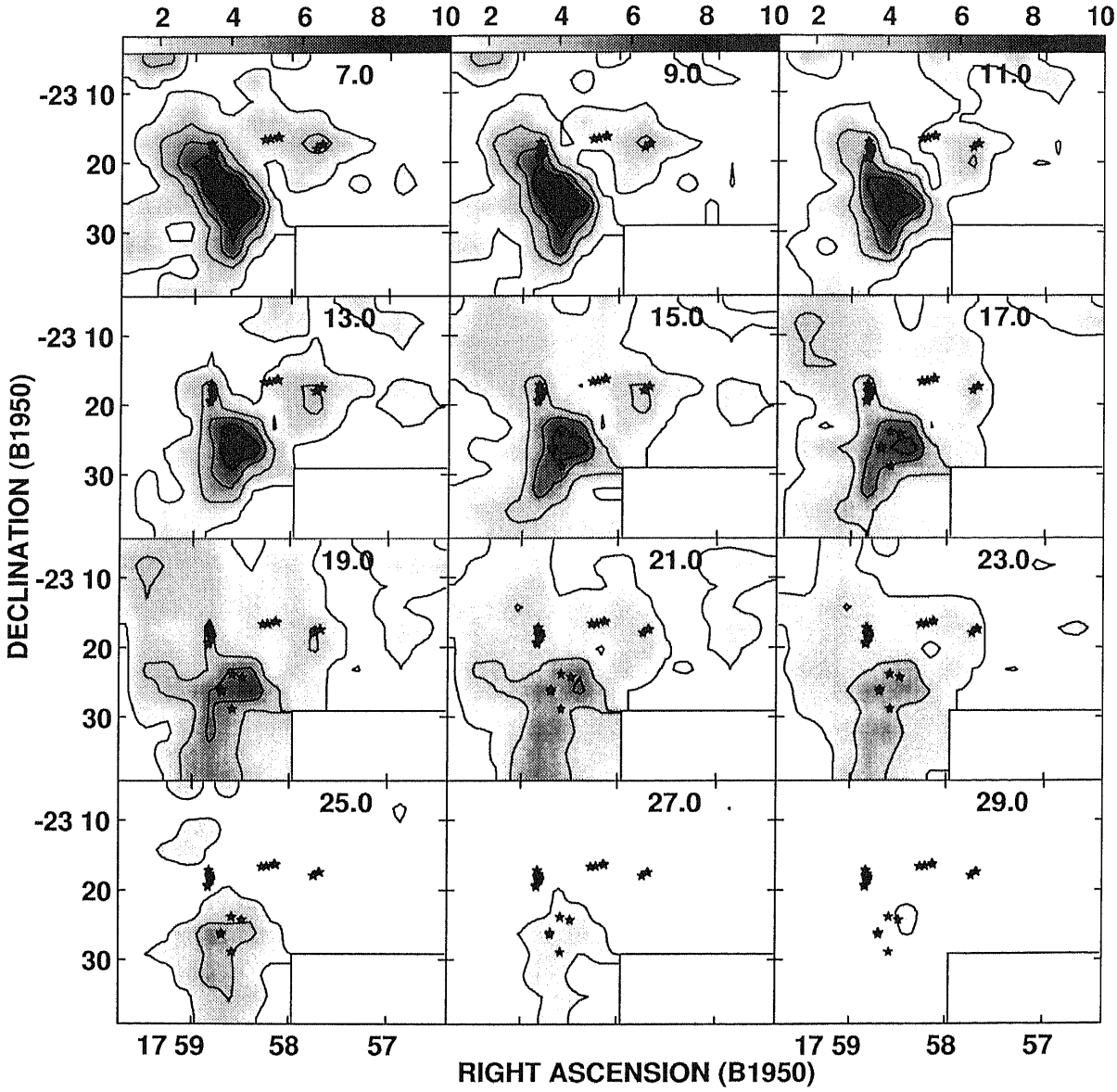

Fig. 4.25.— Part II of Channel maps of the integrated CO (J=3–2) emission toward W28.

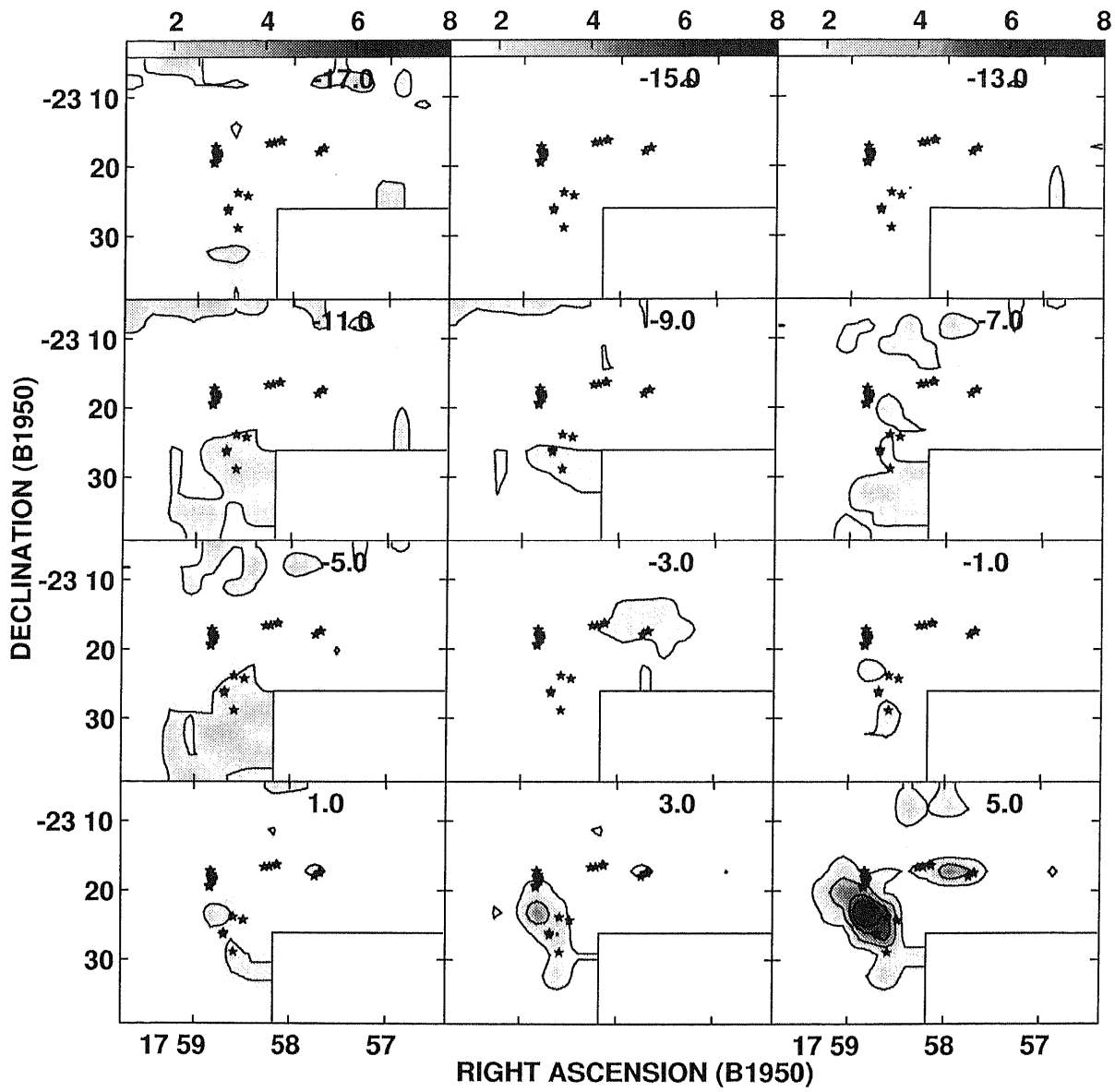

Fig. 4.26.— Part I of Channel maps of the integrated CI ($^3P_1$–$^3P_0$) emission at 2 km s^{-1} velocity intervals toward W28. The center velocity is labeled at the upper right corner. The contour interval is 1.44 K km s^{-1}.

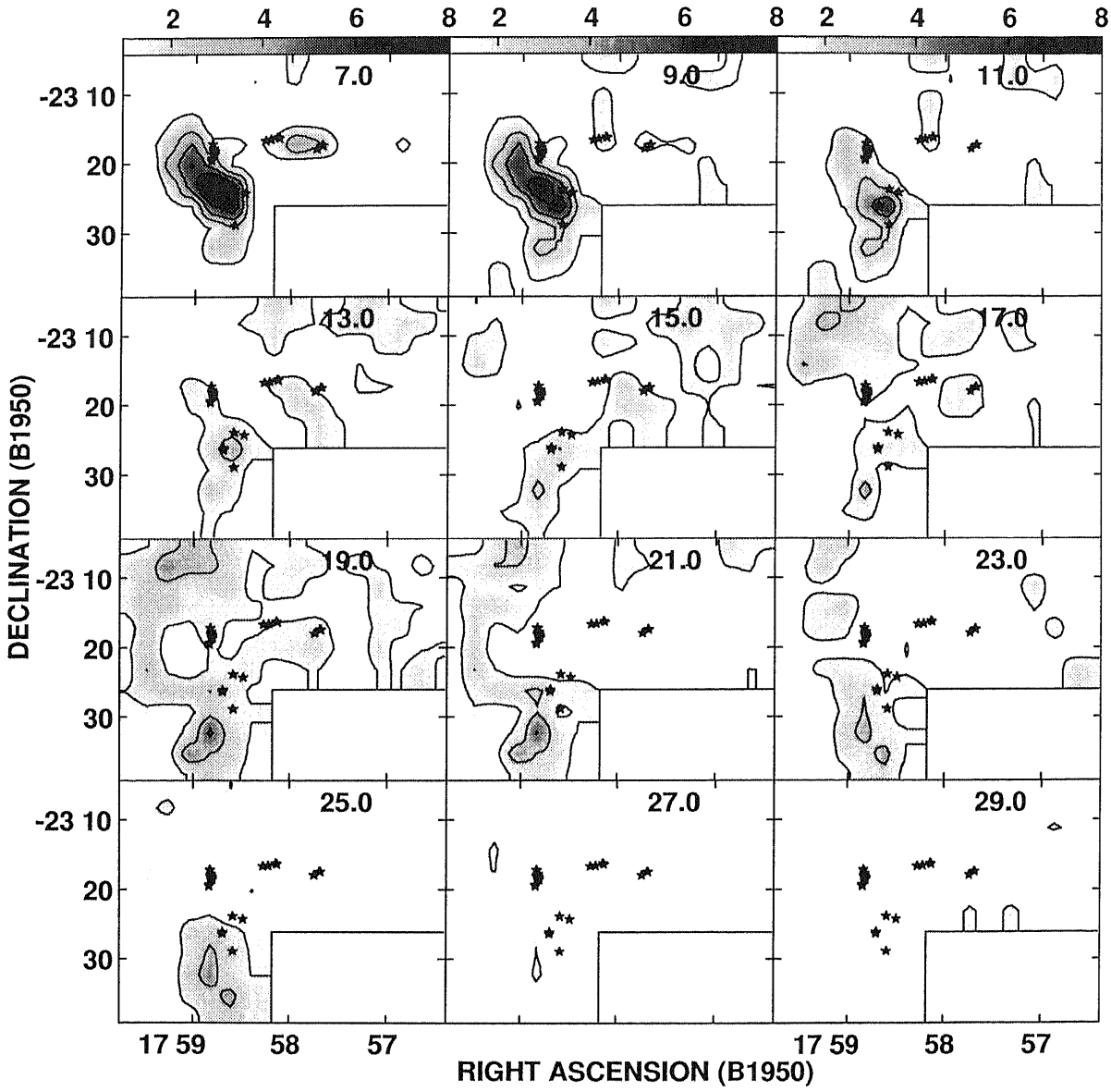

Fig. 4.27.— Part II of Channel maps of the integrated CI ($^3P_1$–$^3P_0$) emission toward W28.

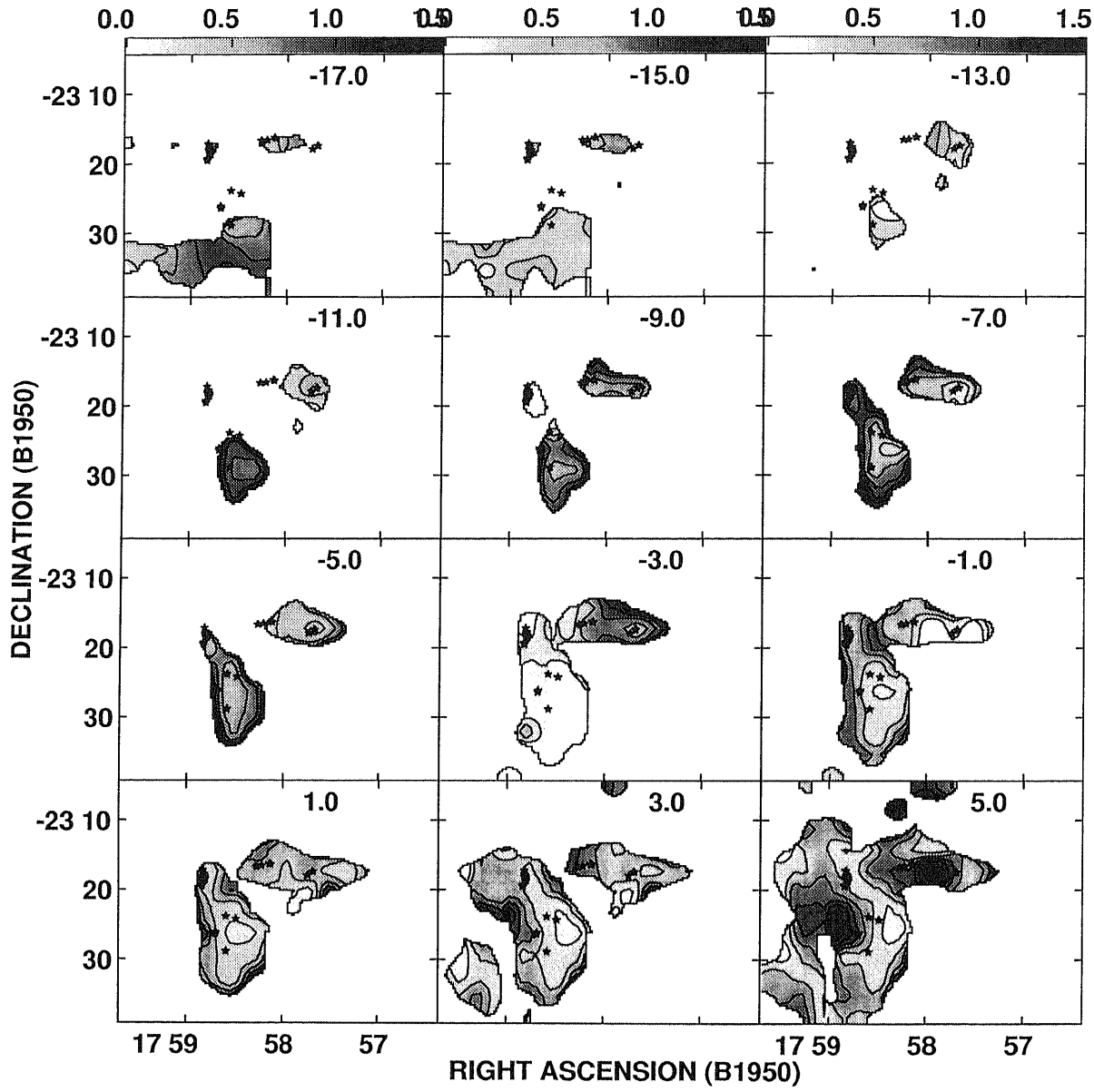

Fig. 4.28.— Part I of Channel maps of the CI ($^3P_1$–$^3P_0$) / CO (J=3–2) integrated intensity ratio at 2 km s^{-1} velocity intervals toward W28. The center velocity is labeled at the upper right corner of each panel. The contour interval is 0.2.

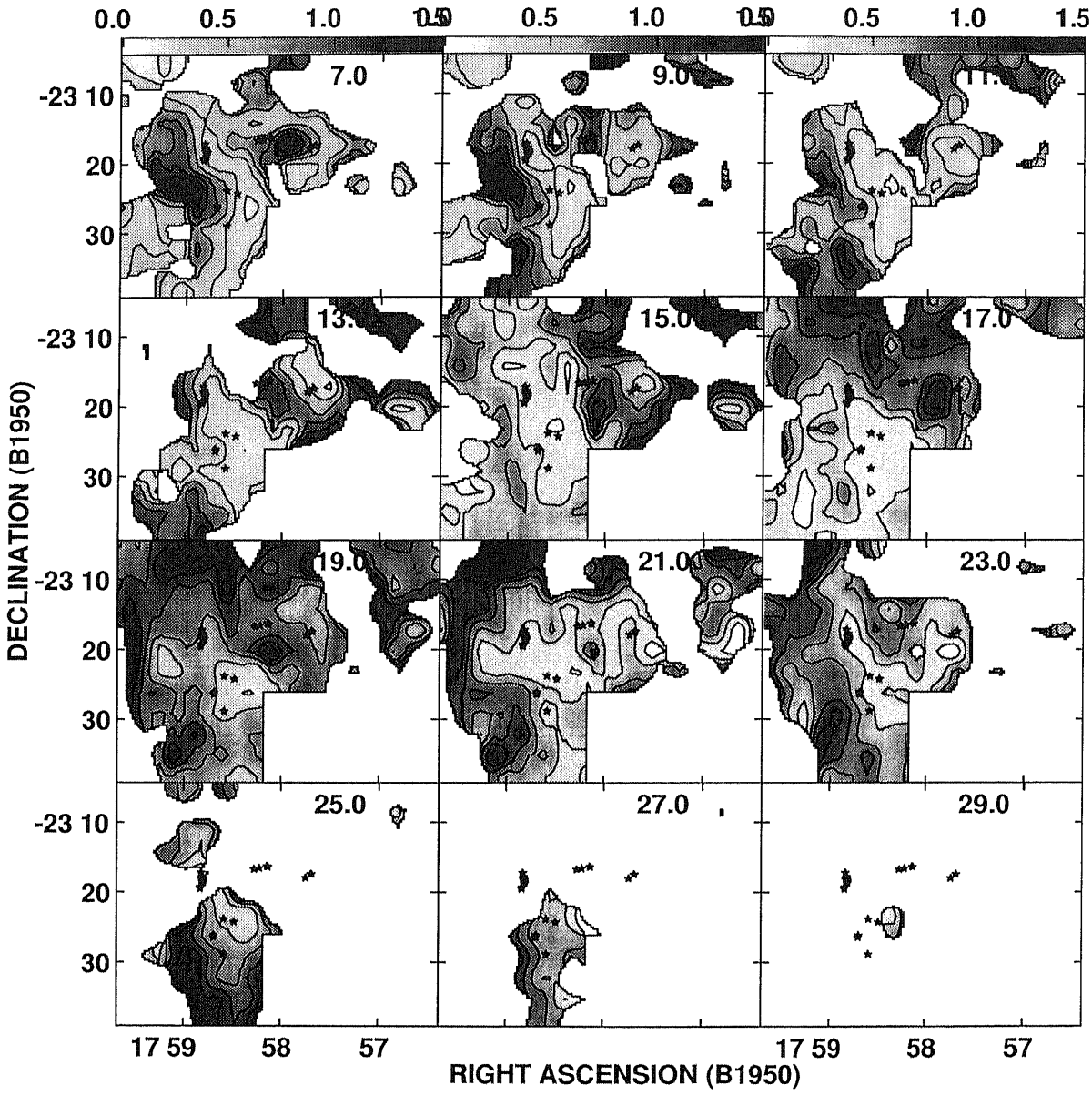

Fig. 4.29.— Part II of Channel maps of the CI ($^3P_1$–$^3P_0$) / CO (J=3–2) integrated intensity ratio toward W28.

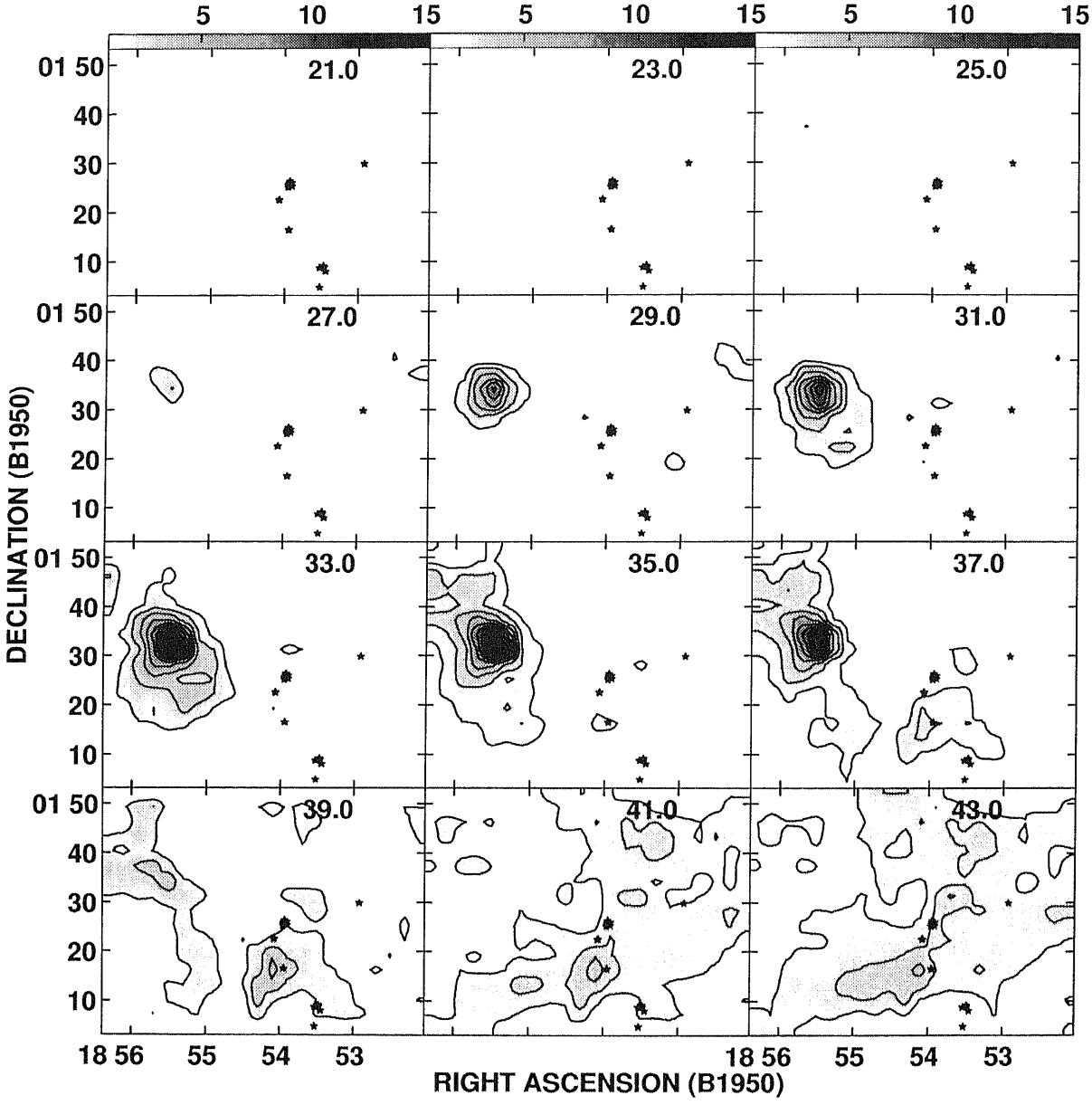

Fig. 4.30.— Part I of Channel maps of the integrated CO (J=3–2) emission at 2 km s^{-1} velocity intervals toward W44. The center velocity is labeled at the upper right corner. The contour interval is 1.39 K km s^{-1}.

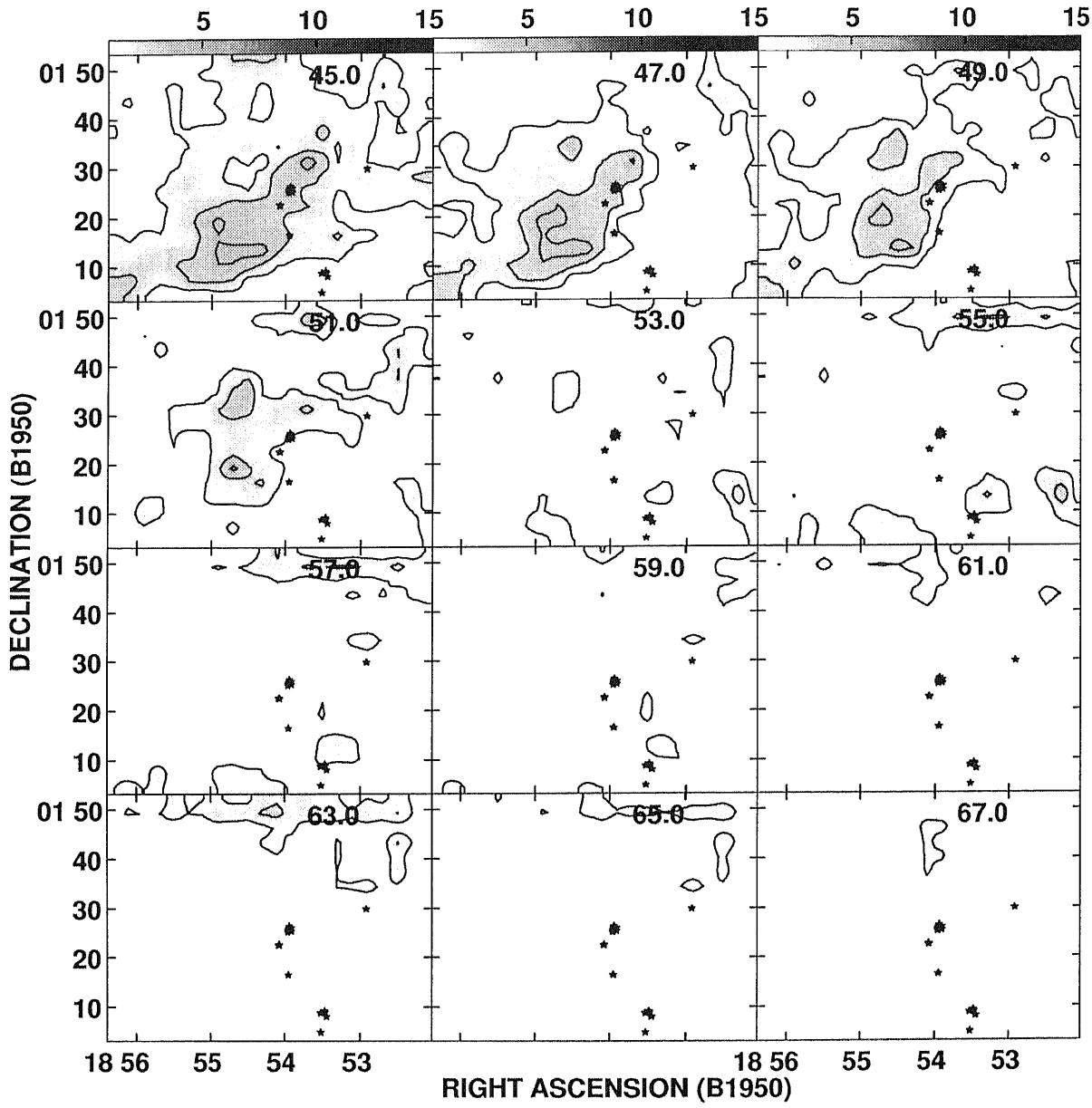

Fig. 4.31.— Part II of Channel maps of the integrated CO (J=3–2) emission toward W44.

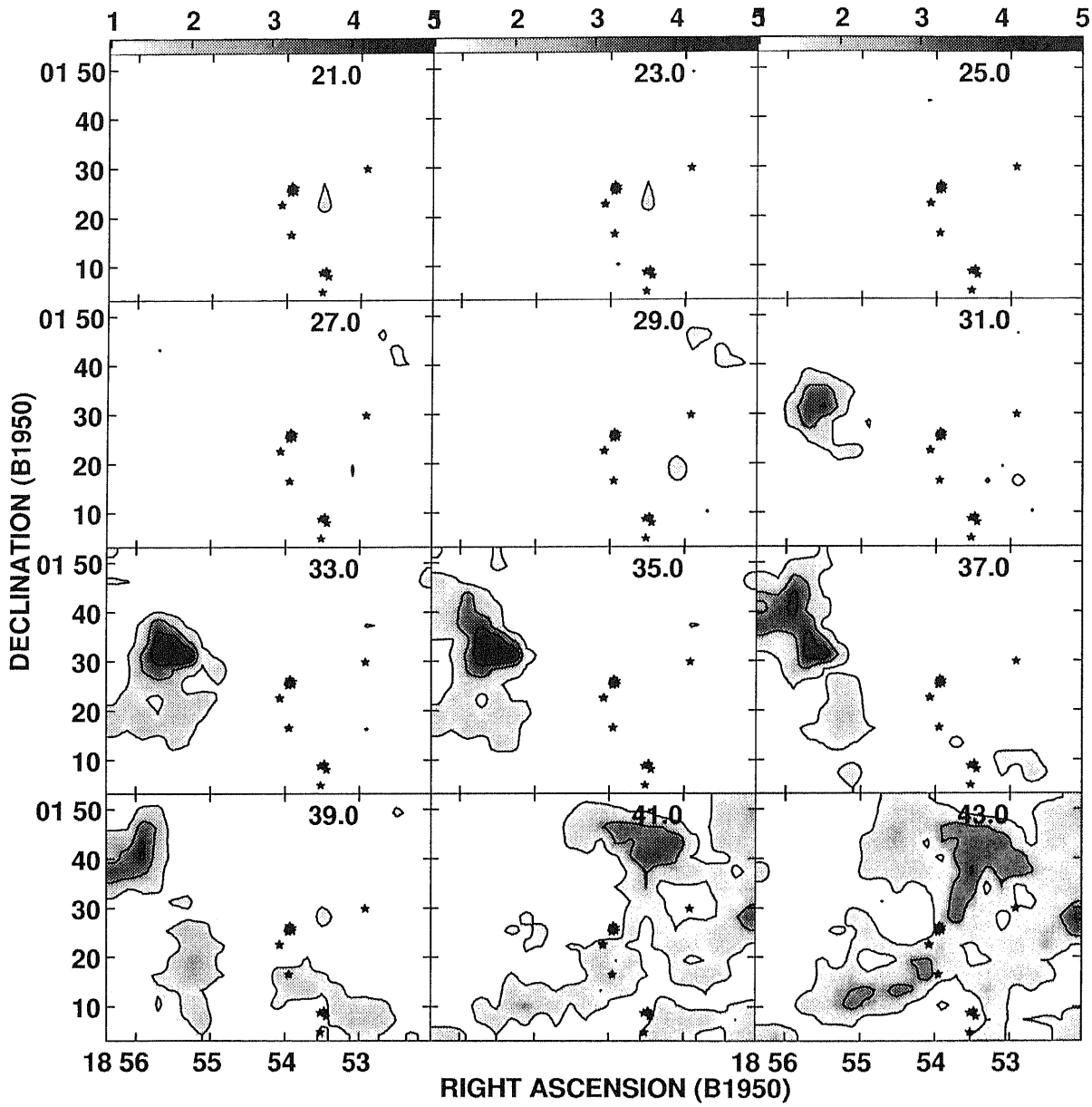

Fig. 4.32.— Part I of Channel maps of the integrated CI ($^3P_1$–$^3P_0$) emission at 2 km s^{-1} velocity intervals toward W44. The center velocity is labeled at the upper right corner. The contour interval is 1.24 K km s^{-1}.

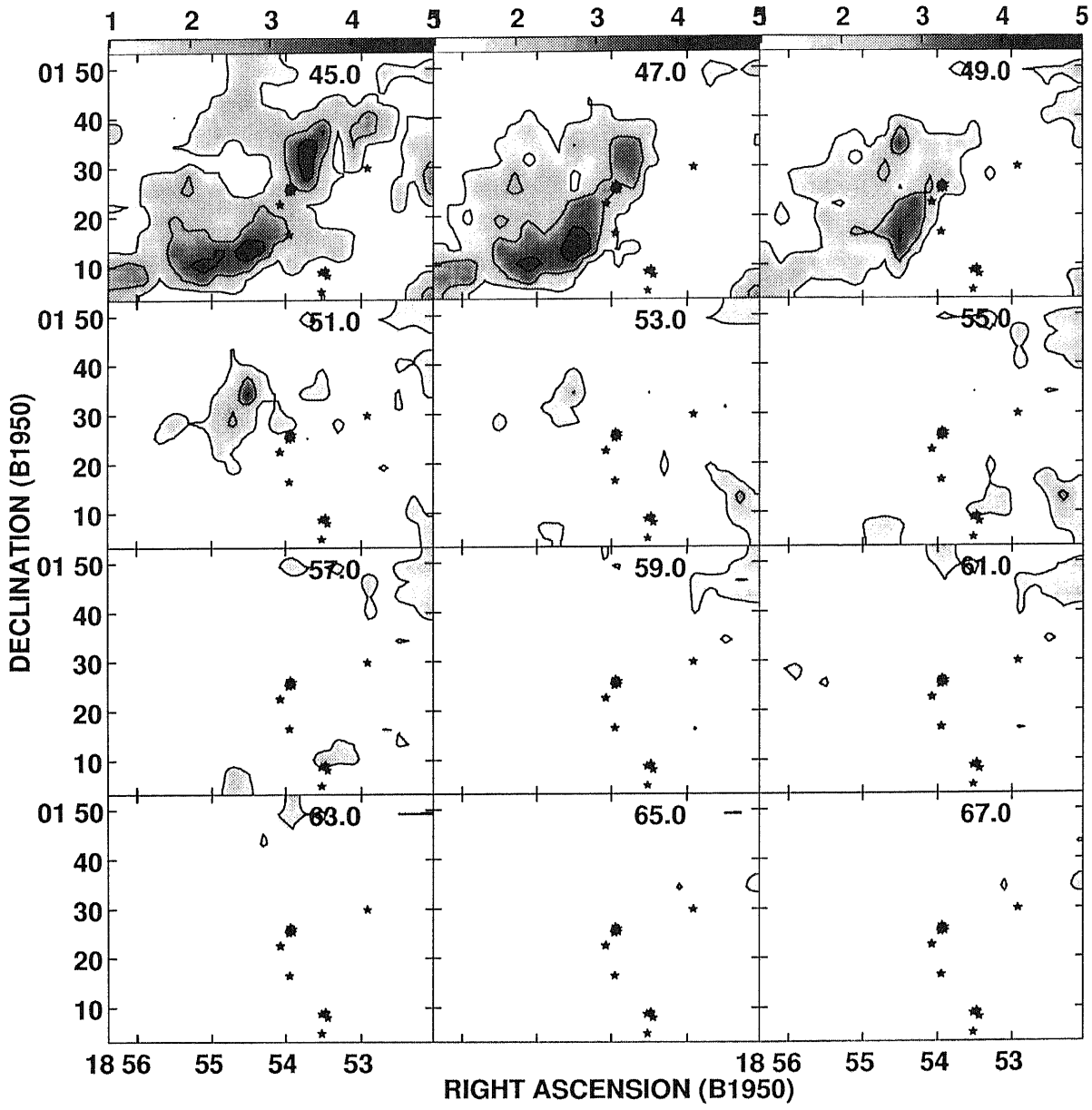

Fig. 4.33.— Part II of Channel maps of the integrated CI ($^3P_1$–$^3P_0$) emission toward W44.

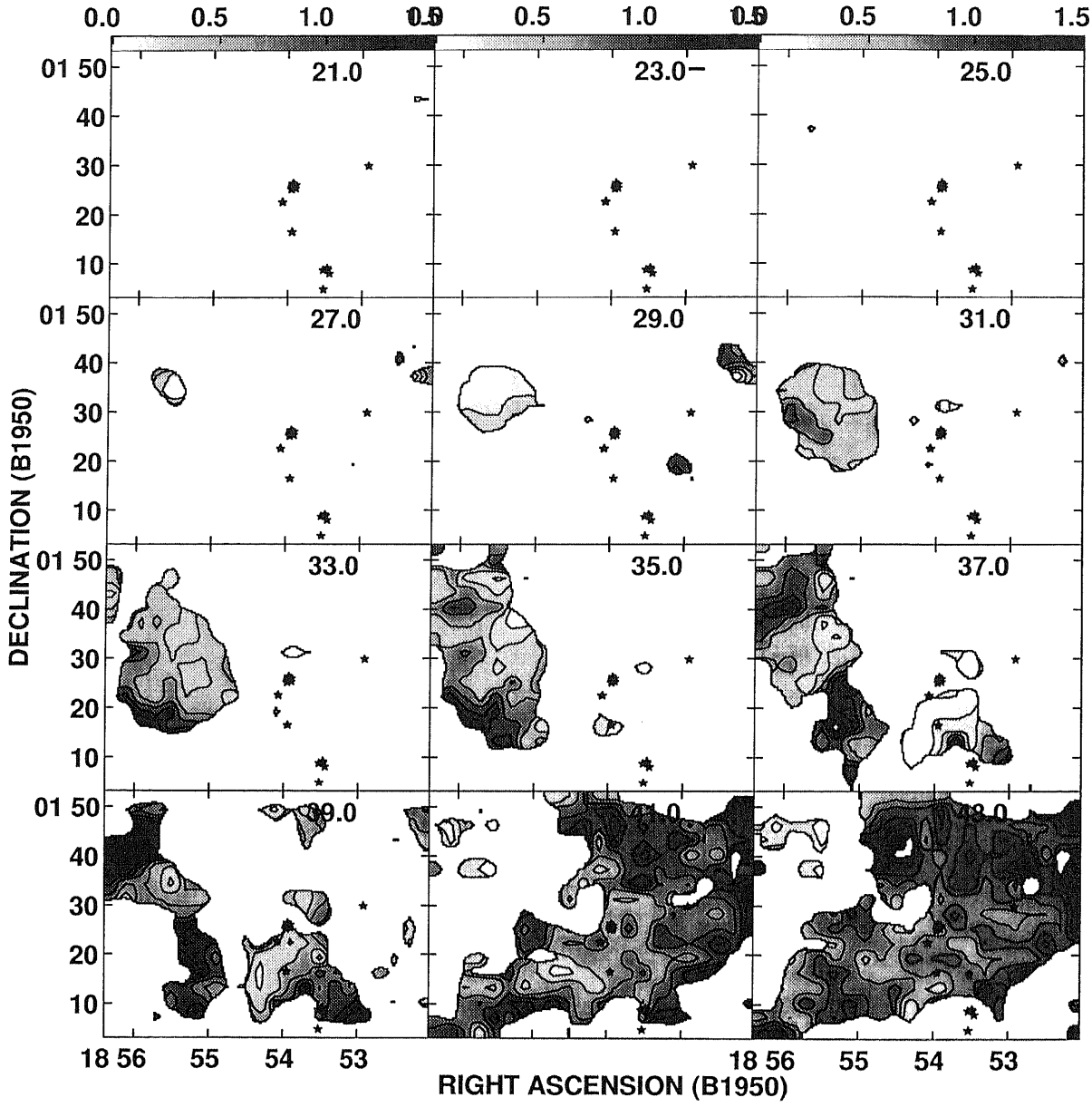

Fig. 4.34.— Part I of Channel maps of the CI ($^3P_1$–$^3P_0$) / CO (J=3–2) integrated intensity ratio at 2 km s^{-1} velocity intervals toward W44. The center velocity is labeled at the upper right corner. The contour interval is 0.2.

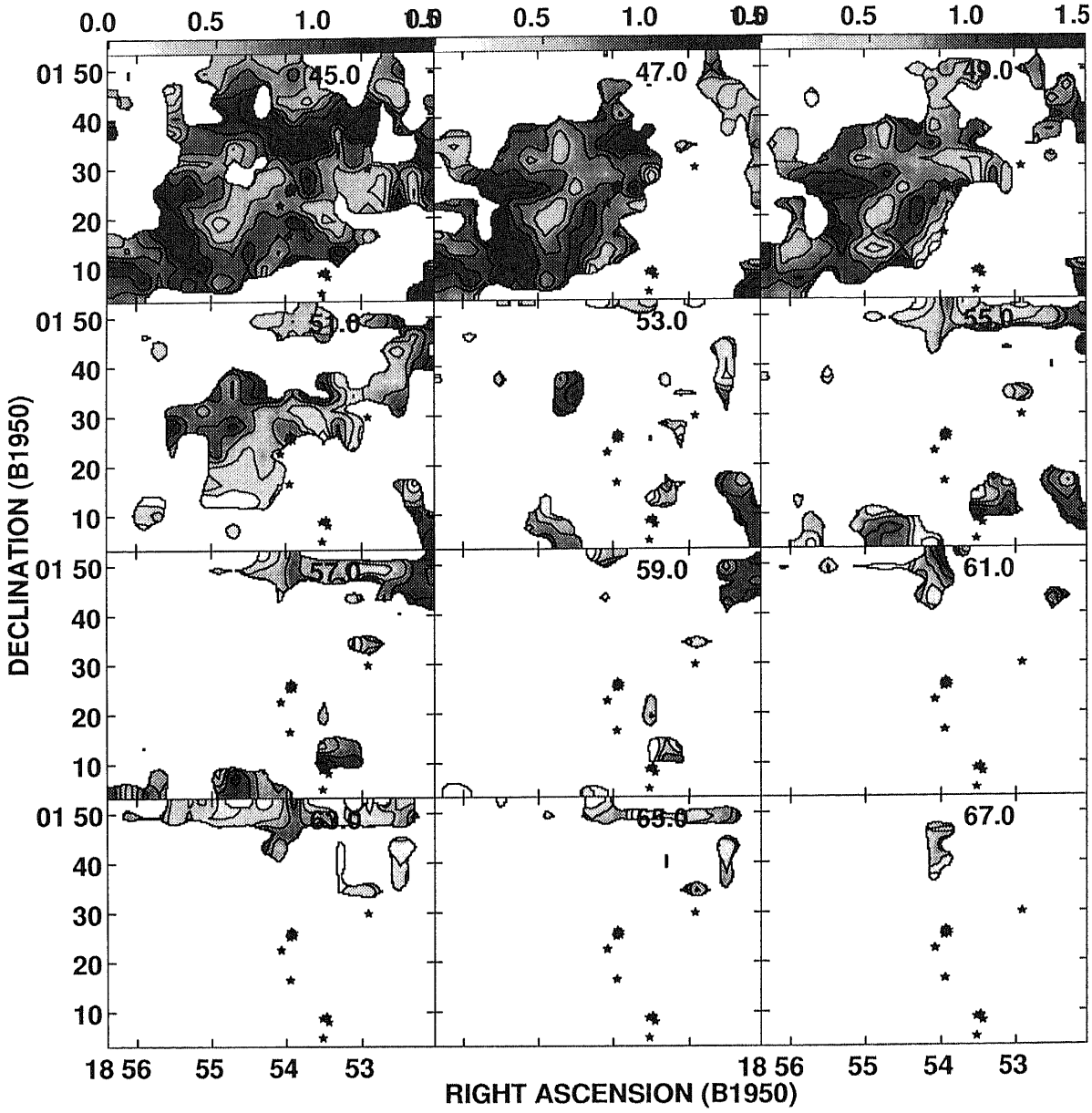

Fig. 4.35.— Part II of Channel maps of the CI ($^3P_1$–$^3P_0$) / CO (J=3–2) integrated intensity ratio toward W44.

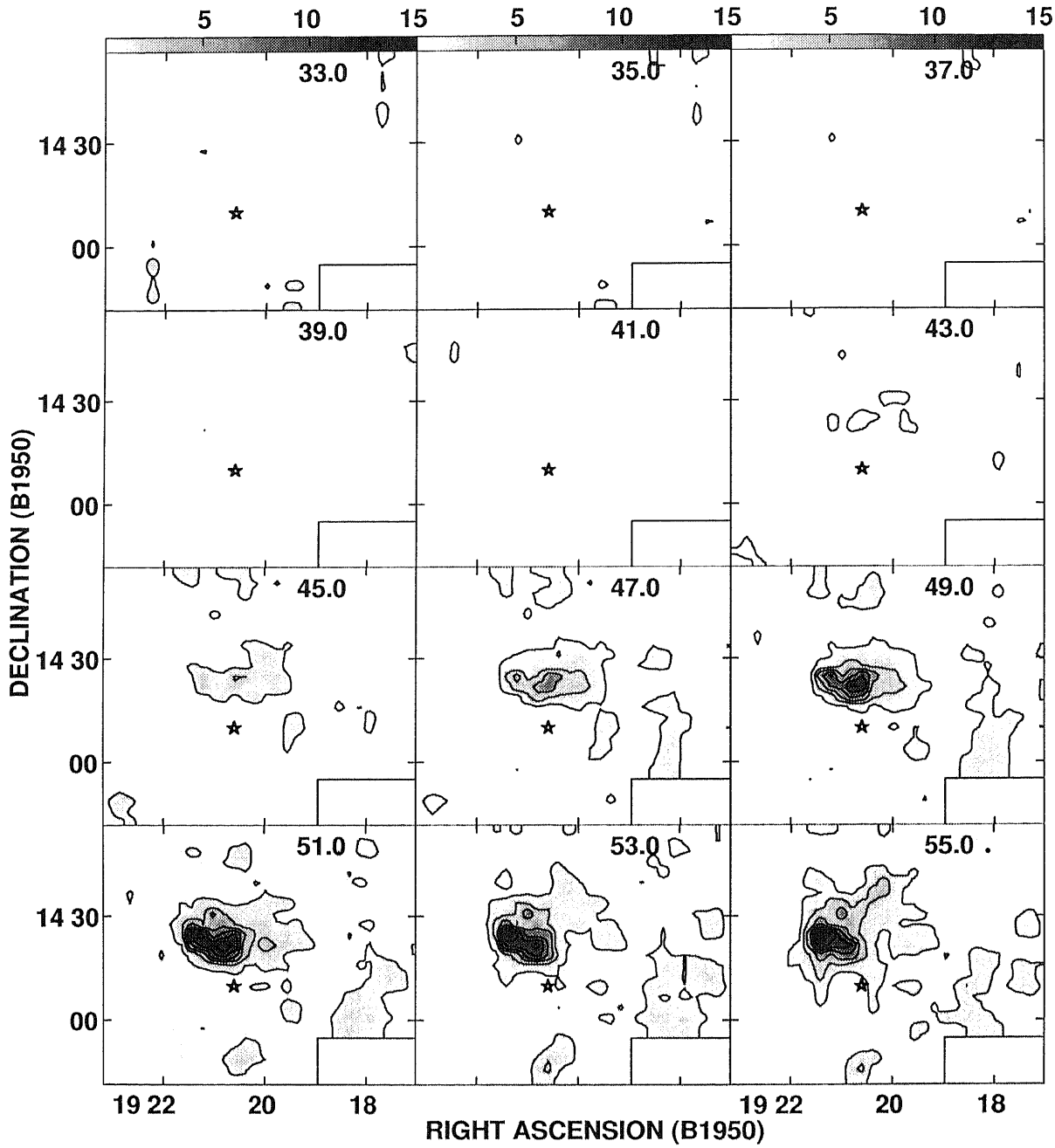

Fig. 4.36.— Part I of Channel maps of the integrated CO (J=3–2) emission to 2 km s^{-1} velocity intervals toward W51. The center velocity is labeled at the upper right corner. The contour interval is 1.00 K km s^{-1}.

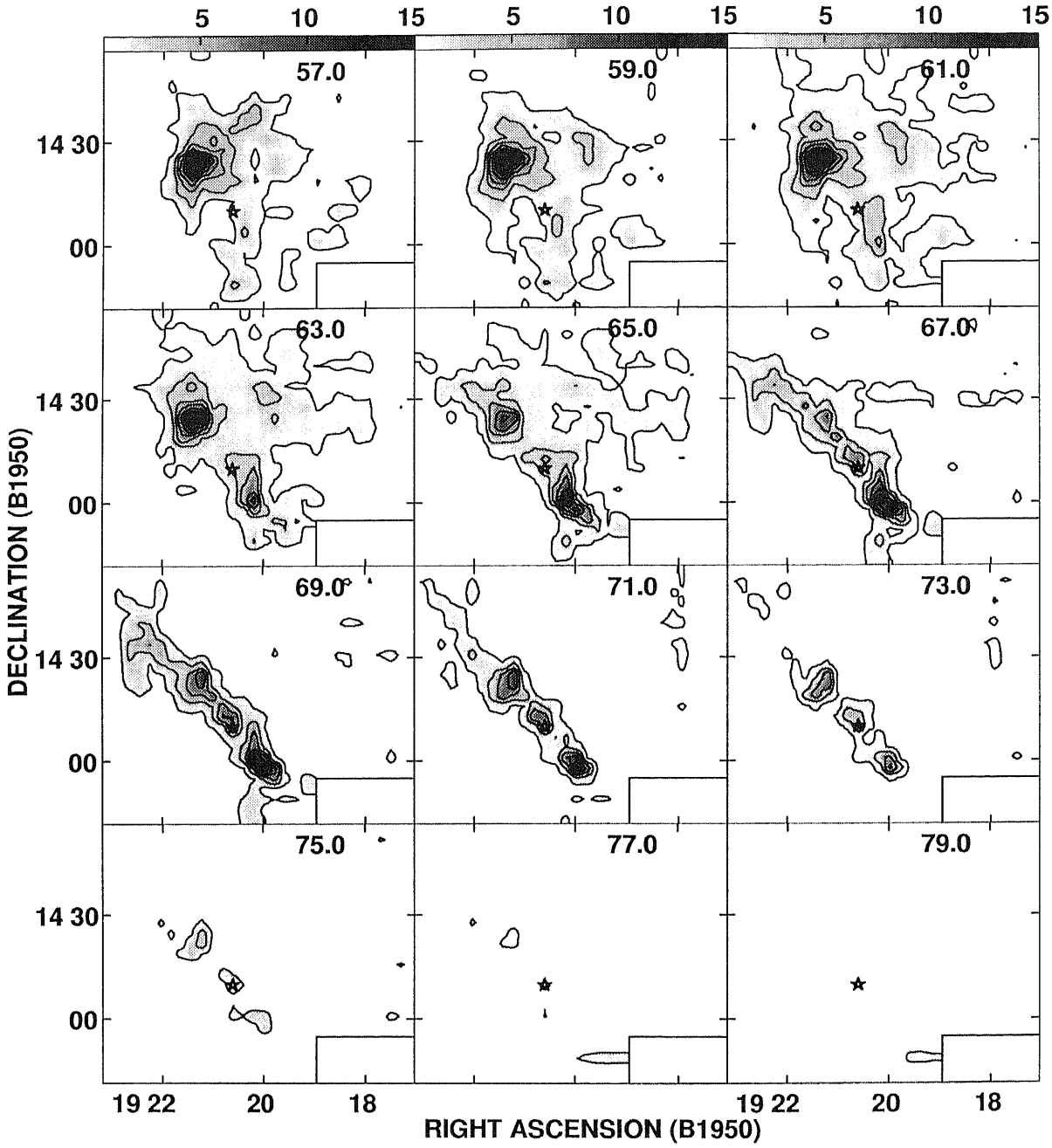

Fig. 4.37.— Part II of Channel maps of the integrated CO (J=3–2) emission toward W51.

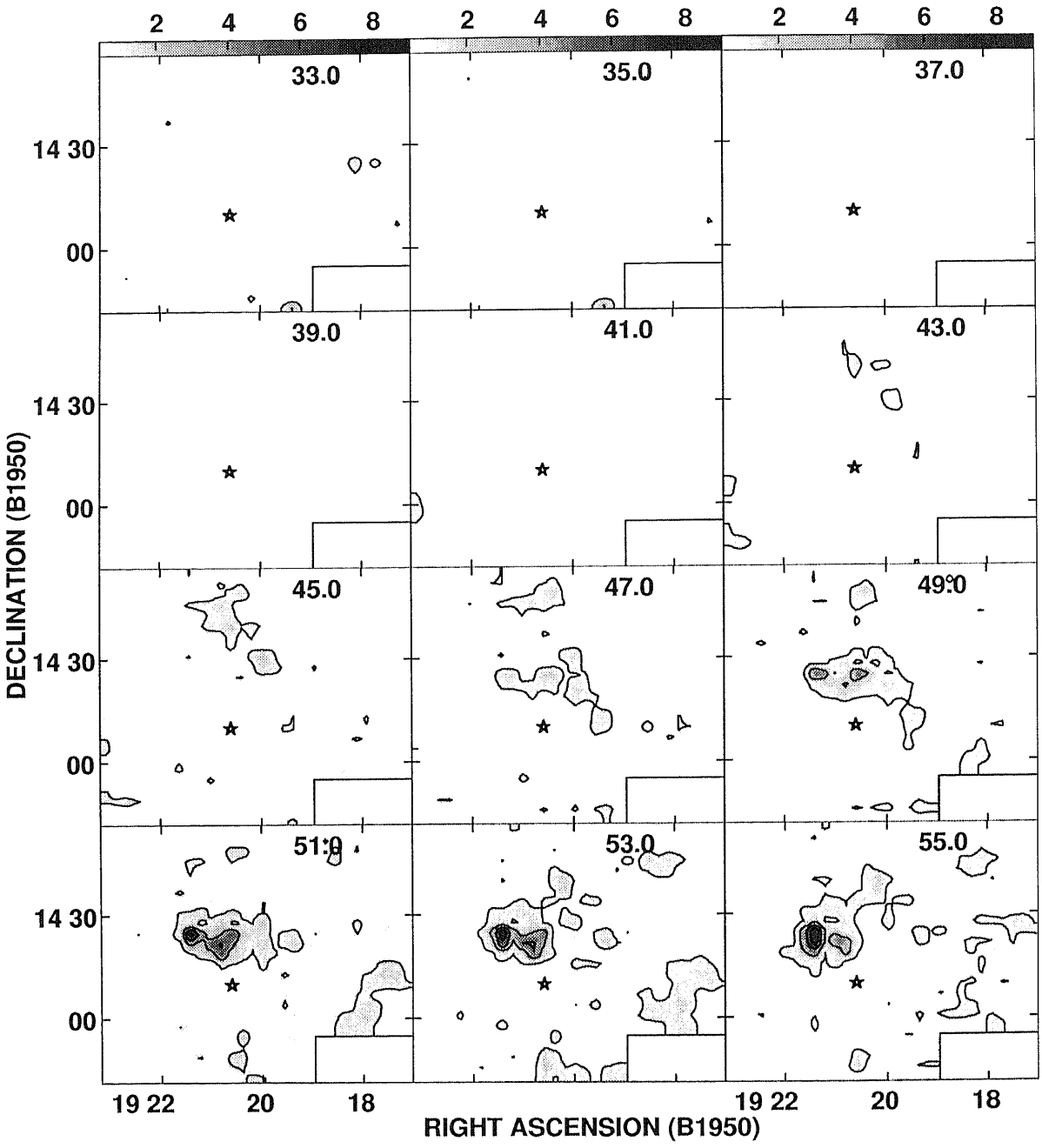

Fig. 4.38.— Part I of Channel maps of the integrated CI ($^3P_1$–$^3P_0$) emission at 2 km s^{-1} velocity intervals toward W51. The center velocity is labeled at the upper right corner. The contour interval is 0.88 K km s^{-1}.

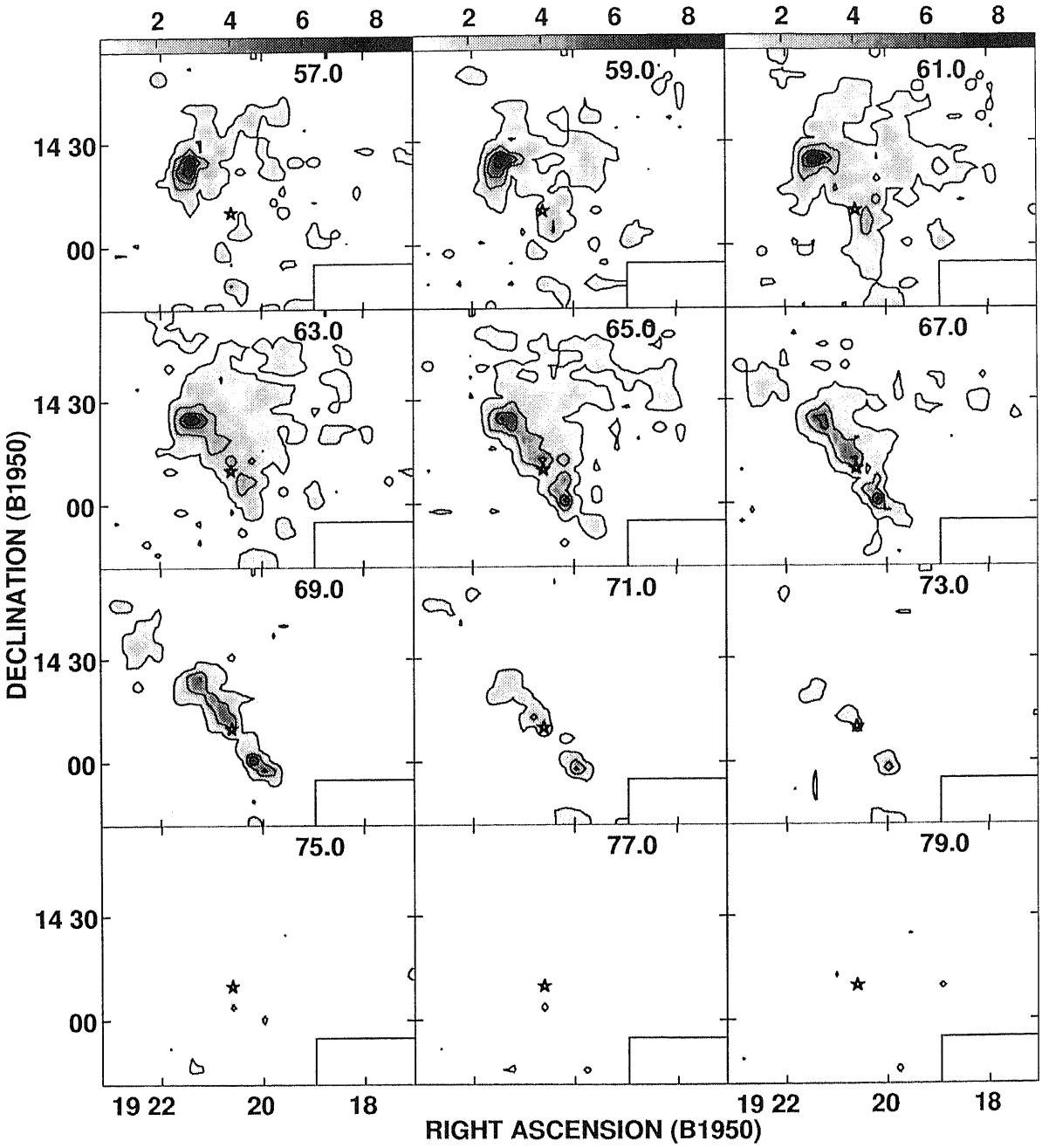

Fig. 4.39.— Part II of Channel maps of the integrated CI ($^3P_1$–$^3P_0$) emission toward W51.

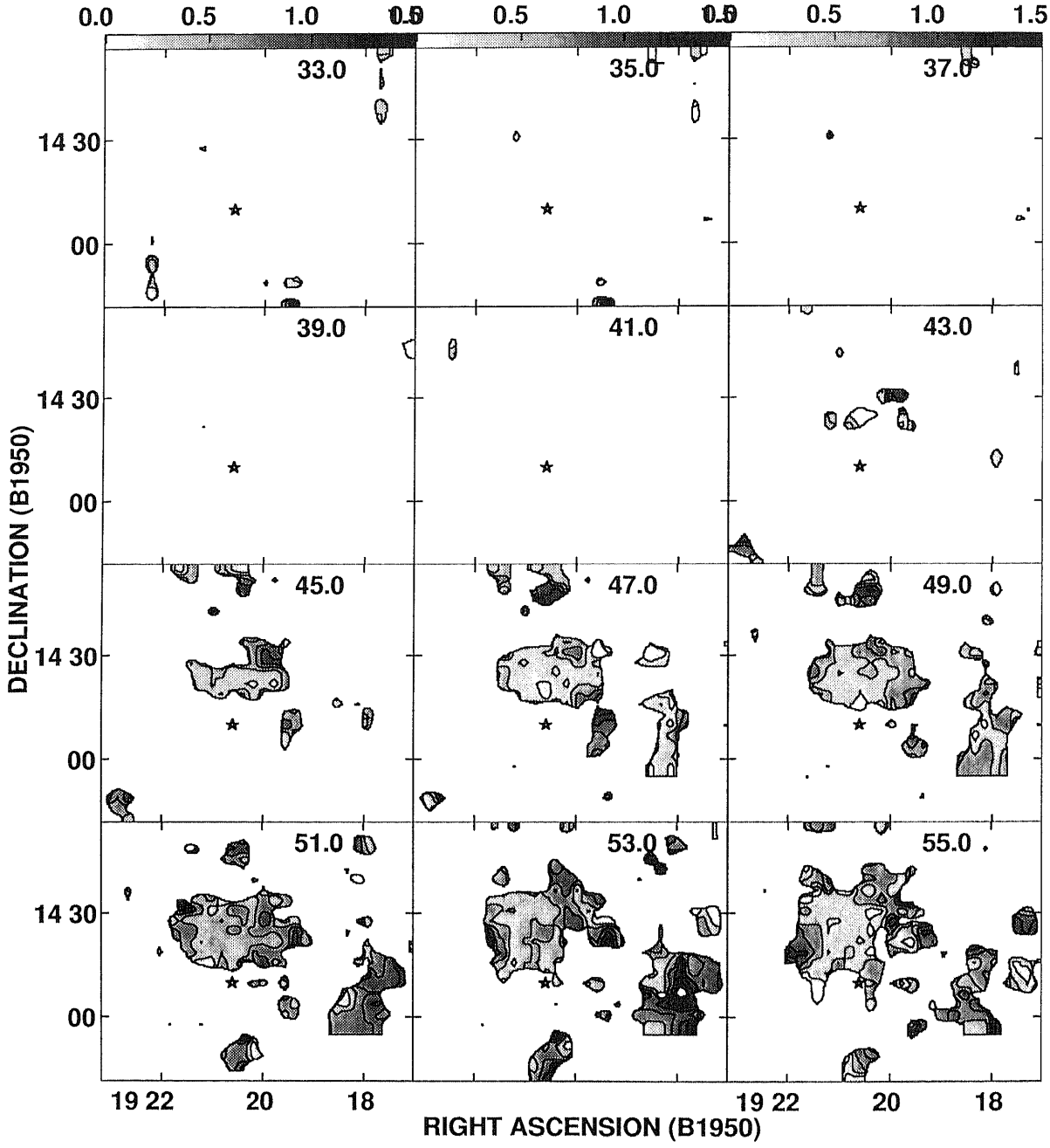

Fig. 4.40.— Part I of Channel maps of the CI ($^3P_1$–$^3P_0$) / CO (J=3–2) integrated intensity ratio at 2 km s^{-1} velocity intervals toward W51. The center velocity is labeled at the upper right corner. The contour interval is 0.2.

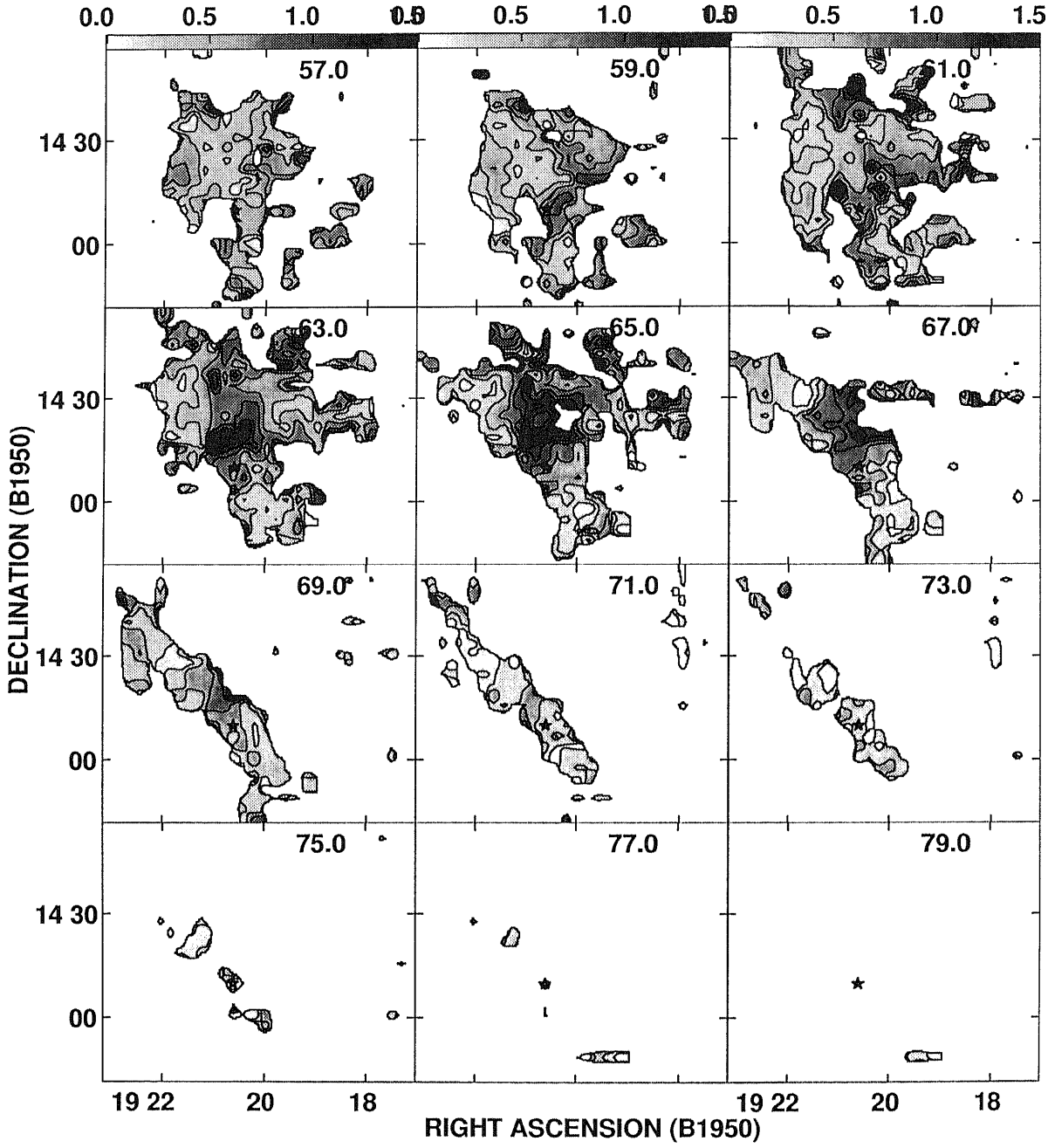

Fig. 4.41.— Part II of Channel maps of the CI ($^3P_1$–$^3P_0$) / CO (J=3–2) integrated intensity ratio toward W51.

References

Arikawa, Y., Tatematsu, K., Sekimoto, Y., Takahashi, T., 1999, PASJ, 51, L7

Burton, M.G., Geballe, T.R., Brand, P.W.J.L., Webster, A.S. 1988, MNRAS, 231, 617

Claussen, M.J., Frail, D.A., Goss, W.M., Gaume, R.A. 1997, ApJ, 489, 143

DeNoyer, L.K. 1979, ApJ, 232, L165

Elitzur, M. 1976, ApJ, 203, 124

Frail, D.A. & Mitchell, G.F., 1998, ApJ, 508, 690

Green, A.J., Frail, D.A., Goss, W.M., Otrupcek, R. 1997, AJ, 114, 2058

Hunag, Y.–L., Dickman, R.L. & Snell, R.L. 1986, ApJ, 302, L63

Ikeda, M., Maezawa, H.,Ito, T., Saito, G. Sekimoto, Y., Yamamoto, S., Tatematsu, K., Arikawa, Y., Aso, Y., Noguchi, T., Shi, S., Miyazawa, K., Saito, S., Ozeki, H., Fujiwara, H., Ohishi, M., Inatani, J. 1999, ApJ, 527, L59

Ingalls, J.G., Chamberlin, R.A., Bania, T.M., Jackson, J.M., Lane, A.P., Stark, A.A. 1997, ApJ, 479, 296

Keene, J., Blake, G., Phillips. G., Huggins, P. & Beichman, C. 1986, ApJ, 299, 967

Kutner, M.L., Ulich, B.L. 1981, ApJ, 250, 341

Koo, B.–C., Moon, D.–S. 1997a, ApJ, 475, 194

Koo, B.–C., Moon, D.–S. 1997b, ApJ, 485, 263

Little, L.T., Brown, A.T., Riley, P.W., Matthews, N., Macdonald,G.H., Vizard, D., & Cohen, R.J. 1983, MNRAS, 203, 409

Meixner, M., Hass, M.R., Tielens, A.G.G.M., & Erickson, E.F. 1992, APJ, 390, 499

Maezawa, H., Ikeda, M., Ito, T., Saito, G., Sekimoto, Y., Yamamoto, S.,Tatematsu, K., Arikawa, Y., Aso, Y., Noguchi, T., S.C. Shi, Miyazawa, K., Saito, S., Ozeki, H., Fujiwara, H., Ohishi, M., Inatani, J. 1999, ApJ 524, L129

Nussbaumer, H. & Rusca, C. 1979, A&A, 72, 129

Phillips, T.G. & Huggins, P.J. 1981, ApJ, 251, 533

Phillips, T.G., Keene, J., van Dishoeck, E.F. 1993, in The Physics and Chemistry Interstellar Molecular clouds, ed G. Winnewisser G.C. Pelz, (Springer: Berli) p96

Plume, R., Jaffe. D.T. & Kenne, J. 1994, ApJ, 425, L49

Saito et al. in preparetion

Sekimoto, Y., Yamamoto, S., Ikeda, M., Maezawa, H., Ito, T., Tatematsu, K., Arikawa, Y., Aso, Y., Noguchi, T., Shi, S.C., Miyazawa, K., Saito, S., Ozeki, H., Fujiwara, H., Inatani, J., Ohishi, M. 1999. in preparation

Seta, M., Hasegawa, T., Dame, T.M., Sakamoto, S., Oka, T., Handa, T., Hayashi, M., Morino, J., Sorai, K., Usuda, K.S. 1998, ApJ, 505, 286

Stutzki, J., Stacey, G., Genzel, R., Harris, A.I., Jaffe, D.T. & Lugten, J.B. 1988, ApJ, 332, 379

Tauber, J.A., & Goldsmith, P.F. 1990, ApJ, 356, L63

Tielens, A.G.G.M. & Hollenbach, D. 1985, ApJ, 291, 722

van Dishoeck, E.F., Jansen, D.J., Phillips, T.G. 1993, A&A, 270, 541

White, G.J., Rainey, R., Hayashi, S.S., Kaifu, N. 1987, A&A, 173, 337

White, G.J. 1994, A&A 283, L25

Wootten, H.A. 1977, ApJ, 216, 440

Wootten, H.A. 1981, ApJ, 245, 105

Chapter 5

Summary

The motivation of this research is to understand the physics and chemistry of the interaction between SNR and the molecular cloud. For this purpose, we carried out observations in the submillimeter-wave lines. The main results are summarized as follows.

5.1 New example of the SNR–cloud interaction : SNR W28

In order to search for the interaction between SNR and the molecular cloud, we observed two SNRs, W28 and γ Cygni SNR, which are supposed to be EGRET gamma-ray sources, in CO (J=3-2) submillimeter-wave line (345 GHz ; 0.9 mm) and in CO (J=1-0) millimeter-wave line (115 GHz ; 2.6 mm).

The shocked gas was not detected toward γ Cygni SNR, but was detected toward W28. In W28, it is found that the line intensity of the CO (J=3-2) emission is stronger than CO (J=1-0) emission in the shocked gas, while CO (J=1-0) emission is stronger than that of CO (J=3-2) emission in the unshocked gas. The observations have clearly shown that the submillimeter-wave lines serve as a powerful tool to investigate the shocked molecular gas.

5.2 Distribution of the shocked molecular gas in SNR W28

In W28, the distribution of the CO gas is similar to that of the 327 MHz radio-continuum emission, and tends to be stronger along the radio-continuum ridge. In addition, the distribution of the unshocked and shocked gas is clearly resolved. The shocked gas is filamentary, and surrounds the center of the supernova explosion. The unshocked gas is displaced by 0.4 – 1.0 pc outward with respect to the shocked gas. The spatial relationship between shocked and unshocked gas has been clarified for the first time for the interaction between SNR and the molecular cloud.

Besides, shocked molecular gas is located in the EGRET error circle. Our observations are consistent with a hypothesis that the interaction of the SNR with the molecular cloud can be the origin of gamma-rays. Moreover, all of the known OH (1720 MHz) maser spots are located along the filament of the shocked gas. These facts convincingly indicate that W28 interacts with the molecular cloud.

5.3 Physical conditions of the shocked molecular gas in W28

The kinetic temperature is $T_{\rm kin} \lesssim 20$ K, and the density is $n({\rm H_2}) \lesssim 10^3$ cm^{-3} for the unshocked gas, while $T_{\rm kin} \gtrsim 60$ K, $n({\rm H_2}) \gtrsim 10^4$ cm^{-3} for the shocked gas.

The total mass of the unshocked gas is estimated to be $M_{\rm unshocked} = 4 \times 10^3\ M_\odot$, and that of the shocked gas is $M_{\rm shocked} = 2 \times 10^3\ M_\odot$. The total kinetic energy deposited in the shocked molecular gas is 3×10^{48} erg, which corresponds to 0.3 % of the energy of the supernova explosion.

5.4 CI abundance in the shocked gas associated with SNR

We observed CO (J=3–2) at 345 GHz (0.9 mm) and CI ($^3P_1$–$^3P_0$) at 492 GHz (0.6 mm) toward the four SNRs, W28, IC 443, W44, and W51C by using the Mt. Fuji submillimeter-wave telescope. The distribution of the CI ($^3P_1$–$^3P_0$) emission toward

W28, W44, and W51 complex region are similar to that of the CO (J=3–2) emission. In IC 443, the CI ($^3P_1$–$^3P_0$) emission was not detected. In the region interacting of SNR with the molecular cloud, the CI ($^3P_1$–$^3P_0$)/CO (J=3–2) peak intensity ratio is high. On the other hand, in unrelated molecular clouds, the ratio is low. This result might imply that the interaction of SNR with the molecular cloud enhances the CI abundance. It is found that the phenomenon of CI abundance enhancement occurs not only in IC 443 but also in other SNRs.

5.5 Future work

The shock region in W28 has rather simple structure and "edge–on". In the future, W28 can be one of the best regions for detailed studies of the SNR–cloud interaction.

At present, though 220 SNRs are cataloged in our Galaxy, the observational examples of the SNR–cloud interaction are only five. In the research in recent years, the about twenty SNRs are the candidate from the existence OH (1720 MHz) maser and the image of X–rays. Through the observation of the JCMT 15 m telescope and Mt. Fuji submillimeter-wave telescope, we clarified that the observation of the submillimeter-wave is effective for the search of the interaction of SNR with the molecular cloud. We are carrying out survey observations in order to find new examples of the interaction by using the Mt. Fuji submillimeter-wave telescope. By increasing the number of the observational examples, we can obtain better understanding of the SNR–cloud interaction.

Acknowledgments

I would like to thank all persons who have been assisting and encouraging me.

First of all, I would like to give my special thanks to Prof. Ken'ichi Tatematsu, my supervisor, for his advice and encouragement. He has provided me with various chances to experience development and research.

I also express my gratitude to Prof. Yutaro Sekimoto for his invaluable suggestions and comments.

I have learned so much from discussion with Prof. S. Yamamoto, M. Ohishi T. Takahashi, and Drs. T. Oka, and Dr. M. Seta, and M. Momose.

I am thankful to the Mt. Fuji submillimeter-wave telescope group members, Prof. S. Saito, M. Inatani, K. Miyazawa, T. Noguchi, and Dr. H. Ozeki, H. Fujiwara, S-C Shi, and Mr. M. Ikeda, H. Maezawa, Y. Aso, T. Ito, G. Saito, for the operation of the telescope, the development of various devices and software, and efforts in improving the performance of the instruments.

I am grateful to Prof. N. Ukita, and Drs. K. Kohno, H. Ezawa, and Dr. K. Nishiyama, S. Takano, K. Sorai, S. Takakuwa, T. Tosaki, and Mr. T. Kamazaki, S. Matsushita, for their friendly help and kind advice

Thanks are also due to Mr. K. Miyazawa, S. Ishikawa, Mrs. S. Inoue, and all of the NRO staff members, for their encouragement.

Finally, I wish to thank my friends and family for their encouragement. I may not complete this dissertation without their continuous support and encouragements.

Appendix A

Mt. Fuji Submillimeter–wave Telescope

Abstract

In this chapter, we explain the Mt. Fuji submillimeter–wave telescope. This telescope was developed by the collaboration of three institutions (*University of Tokyo, Nobeyama Radio Observatory, and Institute for Molecular Science*). The main purpose of the telescope are to obtain large-scale maps of the neutral atomic carbon CI ($^3P_1$–$^3P_0$)emission (f = 492 GHz, λ = 0.6 mm), and to make clear the structure and formation process of the molecular cloud and the phase change of carbon in the interstellar medium. Since the CI ($^3P_1$–$^3P_0$)emission in submillimeter–wave is heavily absorbed by water vapor, and oxygen in the earth atmosphere, observations must be done at high altitude. The summit of Mt. Fuji is one of the best sites for this purpose in Japan. The telescope has a 1.2 m main reflector with a beam size of 3′.0 and 2′.2 at 345 GHz CO (J=3–2) and 492 GHz CI ($^3P_1$–$^3P_0$), respectively. A superconductor–insulator–superconductor (SIS) mixer receiver is used to observe the 492 GHz band in SSB and the 345 GHz band in DSB. The backend is a 1024 channel acousto-optical spectrometer (AOS) with a total bandwidth of 700 MHz. The telescope was installed at the summit of Mt. Fuji in 1998, after test observations was carried out in *Nobeyama Radio Observatory* during 1997 – 1998.

A.1 Introduction

A.1.1 Interstellar Carbon

TABLE A.1

Cosmic Abundances (Phillips et al. 1992)

Element	Relative abundance	Ionization Potential (eV)
H	1.0	13.60
He	8.5×10^{-2}	24.59
O	6.6×10^{-4}	13.62
C	3.3×10^{-4}	11.26

Carbon is an abundant element following hydrogen, helium, and oxygen in the universe. The carbon ionization energy is 11.26 eV, and is lower than the ionization energy of the hydrogen (13.6 eV)(see Table A.1). Carbon is easily ionized by UV radiation even in low energy region where the hydrogen is not ionized. Therefore, Carbon will be in various forms : ionization carbon (CII), neutral atomic carbon (CI), and carbon monoxide (CO). In the low-density region such as the surface of the molecular cloud, carbon is ionized by UV radiation, and exists as CII. Carbon is in the form of CO inside the molecular cloud. CI is sandwiched between CII and CO in photodissociation regions (PDR) (e.g. Tielens & Hollenbach 1985). Moreover, it is suggested that carbon changes its form from CII to CI and CO in chemical evolution of molecular clouds (Suzuki et al. 1992). Therefore, it is possible to make clear the chemical evolution and the detailed structure of the molecular cloud by observing CI. CI plays an important role in interstellar medium.

A.1.2 Neutral Atomic Carbon (CI)

The spectral line of ionized carbon (CII) exists in the far infrared region, and for example it was observed by the group of ISAS (*Institute of Space and Astronautical Science*) by using balloon and satellite (e.g. Makiuti et al. 1996). The spectral line of carbon monoxide molecule CO (J=1-0) exists in the millimeter-wave region (λ = 2.6 mm), and observations have been carried out by various telescopes of all over the

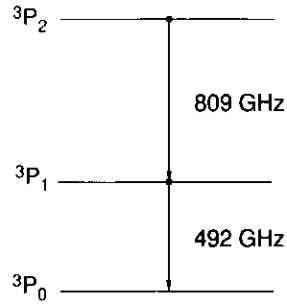

Fig. A.1 Energy levels of atomic carbon

world (e.g. Sanders et al. 1986, Cohen et al. 1986, Dame el al. 1987). In the ground state, neutral atomic carbon (CI) in the ground state has three fine structure levels, $^3P_2, ^3P_1, ^3P_0$ (Figure A.1). The magnetic dipole transition occurs between these levels. The frequencies of the transitions are 492 GHz (λ = 0.6 mm) for $^3P_1$–$^3P_0$ and 809 GHz (λ = 0.4 mm) for $^3P_2$–$^3P_1$.

The first observations of CI were carried out in the transition of $^3P_1$–$^3P_0$ at 492 GHz with the Kuipper Airborne Observatory (Phillips et al. 1981). In 1990's, observational researches of the submillimeter-wave have made great progress, since good detectors using the superconductive technology, which improves the detection sensitivity, have become available even for submillimeter-wave. Two submillimeter telescopes, CSO (*Caltech Submillimeter Observatory*) 10.4 m telescope and 15 m JCMT (*James Clerk Maxwell Telescope*) at the summit of Mauna Kea (el. 4200 m) in Hawaii, which started observations in 1989 and 1988 respectively, have been used for observations of CI. With these telescopes, the detailed maps of the CI ($^3P_1$–$^3P_0$) emission toward the molecular clouds associated with HII regions, S140, M17, and Orion A (White & Padman 1991). The CI emission is observed from dark clouds, TMC–1 and L183, which are nit associated with HII region (Schilke at al. 1995; Stark et al. 1996). From these observational results, it is believed that molecular clouds consist of clumps, and that the UV–radiation penetrates clumpy molecular clouds (e.g. Stutzkil et al. 1988, Tauber & Goldmith 1990, Meixner et al. 1992, Spans et al. 1996).

Galactic-scale CI was observed with the COBE (*Cosmic Background Explorer*), which has a very broad beam (7°) (Wright et al. 1991; Bennet et al. 1994). CI was

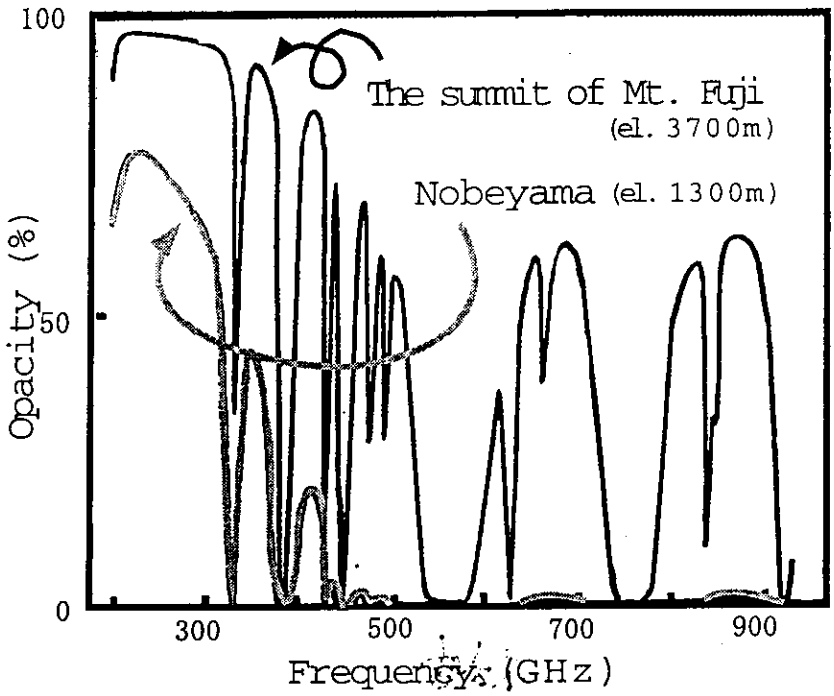

Fig. A.2 Opacity of the submillimeter–wave

observed as intensity as a rotational line J=4–3 of CO, and it was shown that CI play an important role in the cooling of the interstellar medium. Moreover, it has also been found that CI is widely distributed in the Galactic plane. However, the CI distribution on scales of the molecular cloud was not known before our observations.

A.1.3 Opacity of submillimeter–wave

The emission of CI exists in the submillimeter–wave region. The observation of the submillimeter–wave band is very difficult. This is in part due to the the causes at the opacity in the atmosphere of the submillimeter–wave. Figure A.2 shows the opacity in the submillimeter–wave band. Submillimeter–wave observations over 400 GHz is impossible even in Nobeyama Radio Observatory (el. 1300 m) with the millimeter–wave telescope, which is located in a "hi–land". Absorption is due to water vapor (H_2O), O_2, etc, which are included in the earth atmosphere. Therefore, we need high altitude

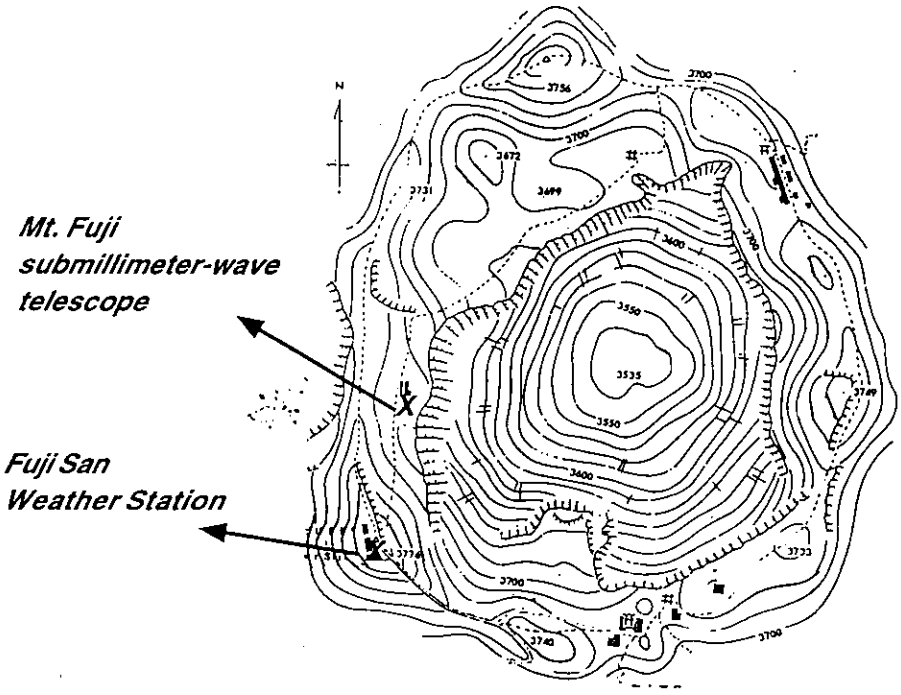

Fig. A.3.— Map of the summit of Mt. Fuji. The telescope site is *Nishi-yasugawara* (el. 3724 m), which is 200 m north of the highest peak, *Kengamine* (el. 3776 m). The Fuji San Weather Station is located at *Kengamine*

places, where water vapor pressure is lower, to observe the submillimeter–wave emission.

A.2 Mt. Fuji submillimeter–wave telescope

Our group (*Nobeyama Radio Observatory, University of Tokyo*, and *Institute for Molecular Science*) constructed a submillimeter–wave telescope at the summit of Mt. Fuji. The telescope site is *Nishi-yasugawara* (el. 3724 m), which is 200 m north of the highest peak, *Kengamine* (el. 3776 m) (Figure A.3).

A.2.1 Antenna

Figure A.4 shows a schematic drawing of telescope. The primary reflector has a diameter of 1.2 m. The surface accuracy is 10 μm, and the material is the aluminum. The half power beam size is about 2′ at 492 GHz and 3′ at 345 GHz, respectively.

TABLE A.2

Speck of Mt. Fuji submillimeter–wave telescope (Sekimoto et al. 1999)

parameter	specification
Diameter	D = 1.2 m
Beam Width (HPBW)	2′.2 @ 492 GHz
	3′.1 @ 345 GHz
Receivers	SIS 492 & 345 GHz
Backend	AOS
bandwidth	700 MHz
channel separation	0.9 MHz
effective resolution	1.6 MHz
Radome:	
diameter	2.92 m
membrane	Gore–Tex 0.3 mm thickness
System Noise temperature	1200 K (SSB) @ 492 GHz
	500 K (DSB) @ 345 GHz

With this beam size, we can obtain the information on scales of molecular clouds in reasonable observational time.

A.2.2 Radome

The telescope is covered by a 3–m space–frame radome with Gore–Tex membrane in order to protect the telescope from strong wind and snow. The transparencies at 492 GHz and 345 GHz are 90 % and 95 %, respectively. The telescope and radome are supported by separate structures so that strong winds will not vibrate the telescope.

A.2.3 Frontend

The receiver frontend is SIS (Superconductor–Insulator–Superconductor) receivers cooled down to about 4.6 K. It can detect the 345 GHz (CO (J=3–2)) and 492 GHz (CI ($^3P_1$–$^3P_0$)) bands simultaneously by using a polarization splitter. It employs Nb–base SIS mixers, which are parallel–connected twin junctions (Shi, Noguchi &

Inatani 1997). The receiver noise temperature is 200 K (DSB) for 345 GHz and 300 K (SSB) for 492 GHz.

A.2.4 Backend

The backend is an acousto-optical spectrometer (AOS) with a total bandwidth of 700 MHz and a channel number of 1024. The velocity resolution is 1.0 km s^{-1} in 492 GHz. The system is stored in a duralumin case of 20 cm × 20 cm × 60 cm size, and it is designed to stably operate even in severe condition of the summit of Mt. Fuji with mechanical and thermal isolation. For simultaneous observation of 345GHz and 492GHz, the IF synthesis is employed and halves of the AOS band are used for the two frequency bands.

A.2.5 Remote control

Because human access to summit is extremely difficult in the observation season (winter), the telescope is connected to NRO or U. Tokyo using the commercial satellite communication (64 kbps), and is operated by the remote control. The system also has a back up line using a commercial satellite telephone system.

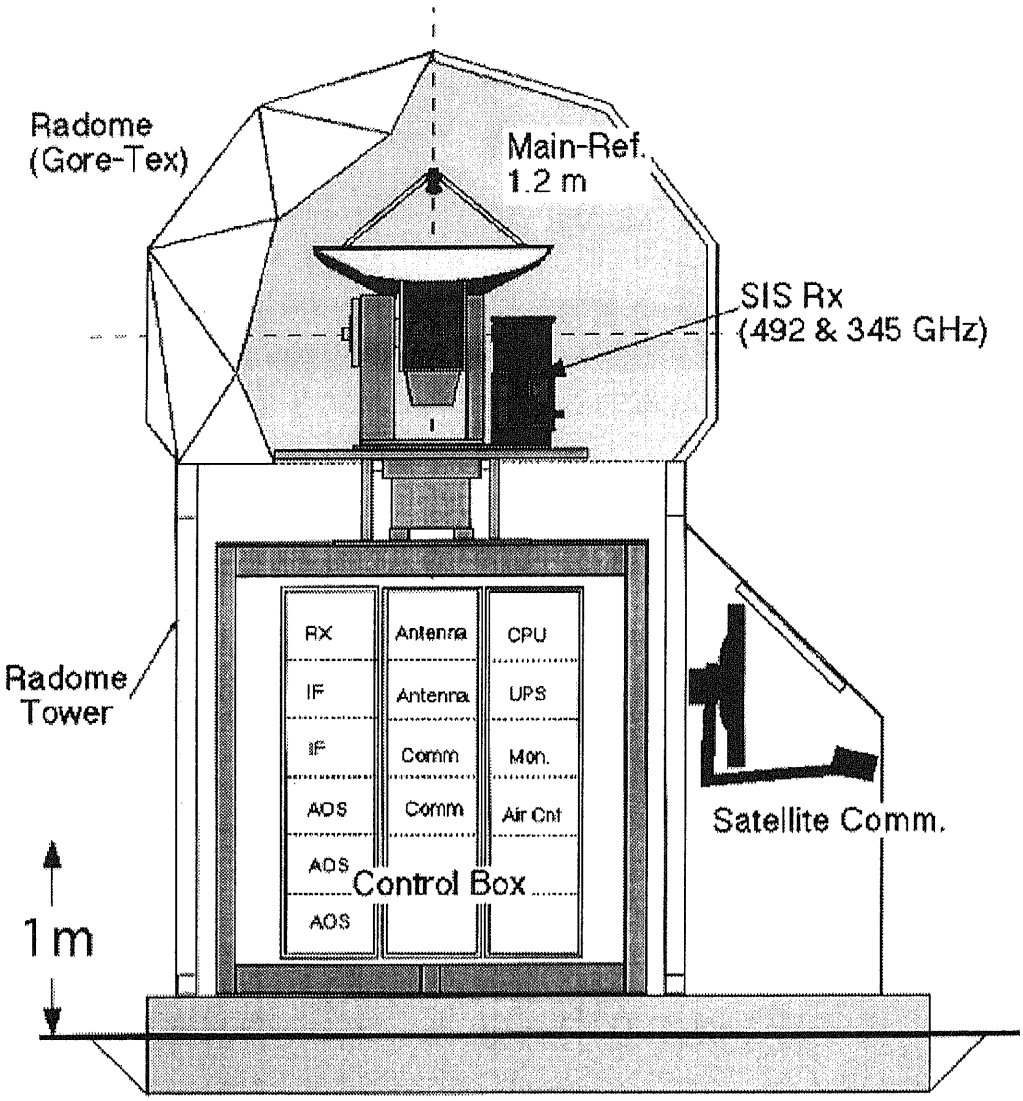

Fig. A.3 Mt. Fuji submillimeter–wave telescope

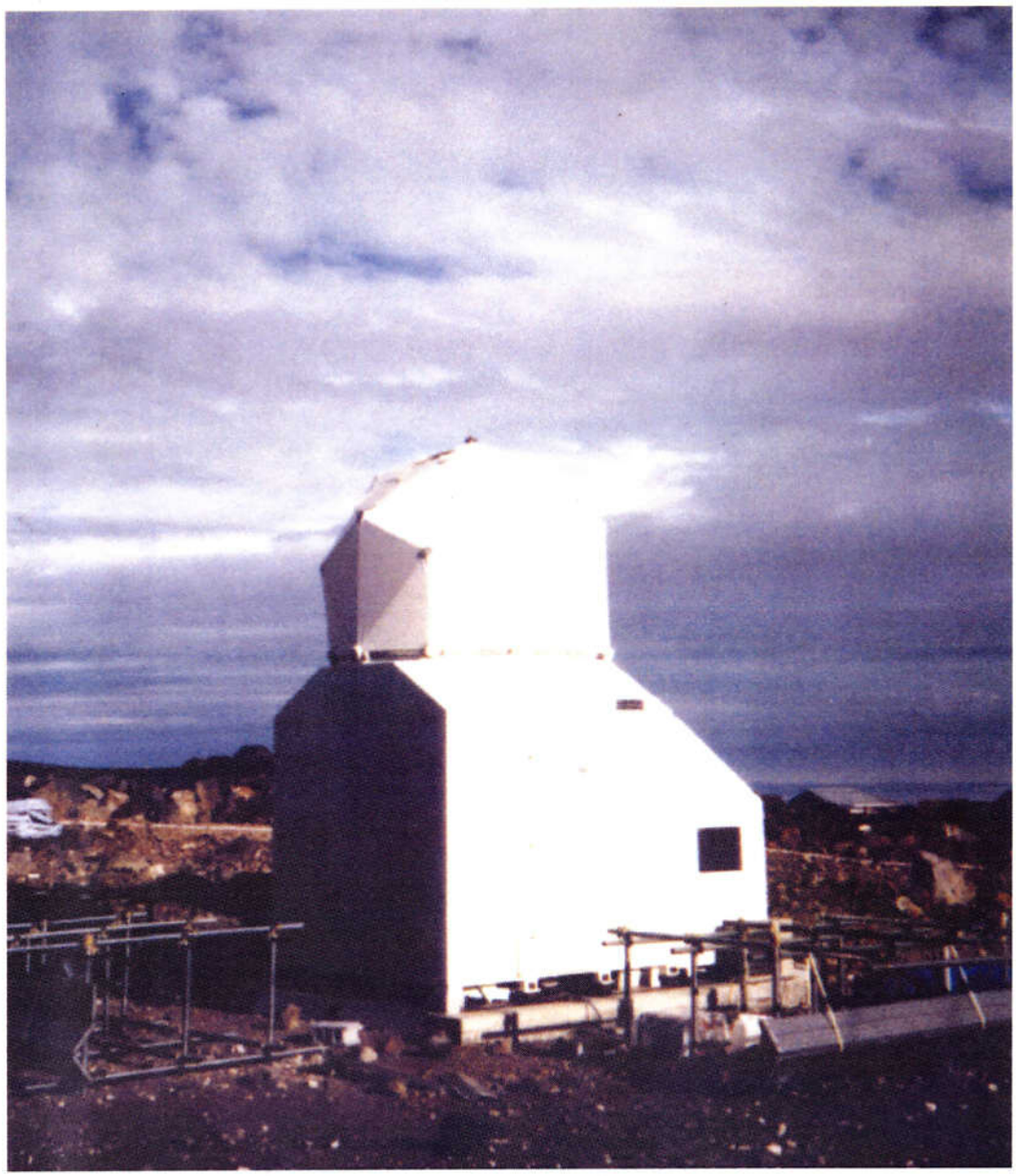

Fig. A.4 Mt. Fuji submillimeter-wave telescope

References

Bennett, C.L. et al. 1994, ApJ, 434, 587

Burton, M.G., Hollenbach, D.J., & Tielens, A.G.G.M., 1990, ApJ, 365, 620

Cohen, R.S., Dame, T.M., & Thaddeus, P., 1986, ApJS, 60, 695

Dame, T.M., Ungerechts, H., Cohen, R.S., de Geus, E.J., Grenier, I.A., May, J., Murphy, D.C., Nyman, L.A. & Thaddeus P. 1987, ApJ, 322, 706

Meixner, M., Hass, M.R., Tielens, A.G.G.M., & Erickson, E.F. 1992, APJ, 390, 499

Makiuti, S., Shibai, H., Okuda, H., Nakagawa, T., Matsuhara, H., Hiromoto, N., & Okumura, K. 1996, PASJ, 48, L71

Phillips, T.G., Huggins, P.J., Kuiper, T.B.H., & Miller R.E. 1981, ApJ, 238, L103

Phillips, T.G., & Keene, J. 1992, Proceedings of the IEEE, 80–11, 1662

Sanders, D.B., Clemens, D.P., Scoville, N.Z., & Solomon, P.M. 1986, ApJS, 60,1

Schilke, P., Keene, J., Le Bourlot, J., Pineau des Forêts, G., & Roueff, E. 1995, A&A, 294, L17.

Shi, S.C., Noguchi, T. & Inatani, J. 1997, IEEE Trans. Applied Supercondoctivity, 7, 2587

Sekimoto, Y., Yamamoto, S., Ikeda, M., Maezawa, H., Ito, T., Tatematsu, K., Arikawa, Y., Aso, Y., Noguchi, T., Shi, S.C., Miyazawa, K., Saito, S., Ozeki, H., Fujiwara ,H., Inatani, J., & Ohishi, M. 1999. in preparation

Stark, R., Wesselius, P.R., van Dishoeck, E.F. & Laureijs, R.J. 1996, A&A, 311, 282

Suzuki, H., Yamamoto, S., Ohishi, M., Kaifu, N., Ishikawa, S., Hirahara, Y., & Takano S. 1992, ApJ, 392, 551

Stutzki, J., Stacey, G., Genzel, R., Harris, A.I., Jaffe, D.T. & Lugten, J.B. 1988, ApJ, 332, 379

Tauber, J.A., & Goldsmith, P.F. 1990, ApJ, 356, L63

Tielens, A.G.G.M. & Hollenbach, D. 1985, ApJ, 291, 722

van Dishoeck, E.F. 1988, ApJ, 334, 771

White, G.J. & Padman, R. 1991, Nature, 354, 511

Wright, E.L. et al. 1991, ApJ, 381, 200

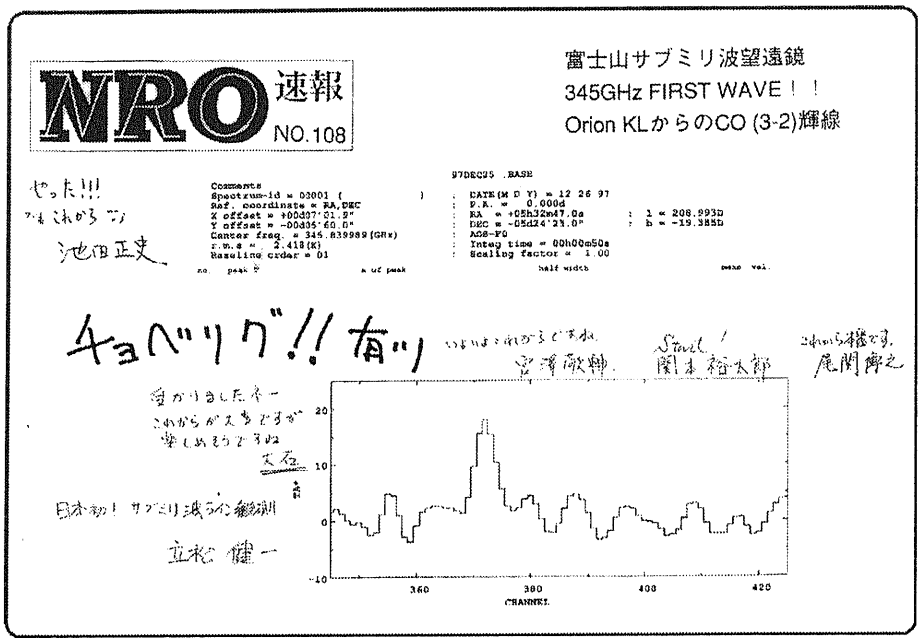

Fig. A.5 No. 108 of NRO News

Fig. A.6 No. 113 of NRO News

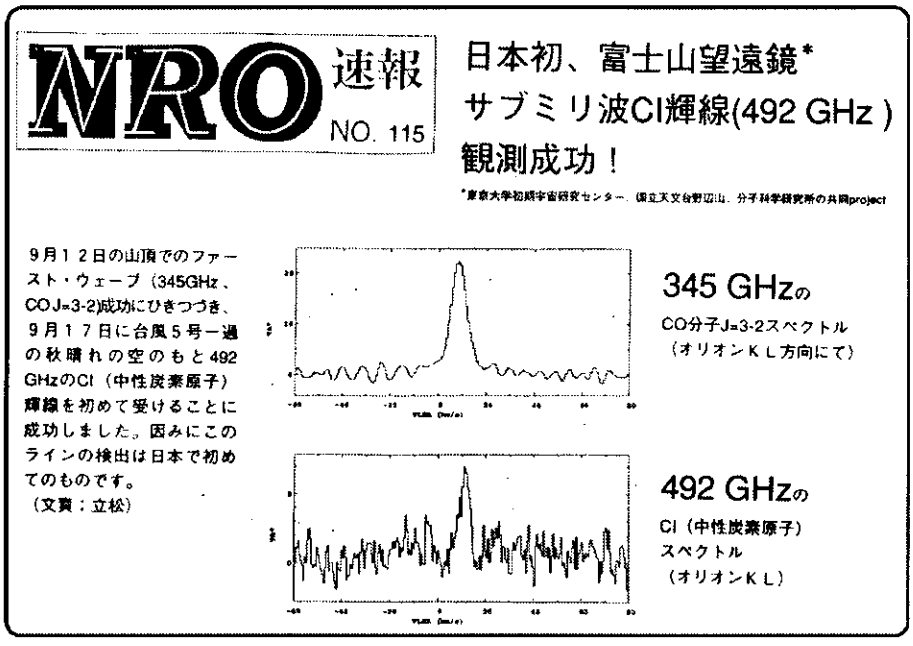

Fig. A.7 No. 115 of NRO News

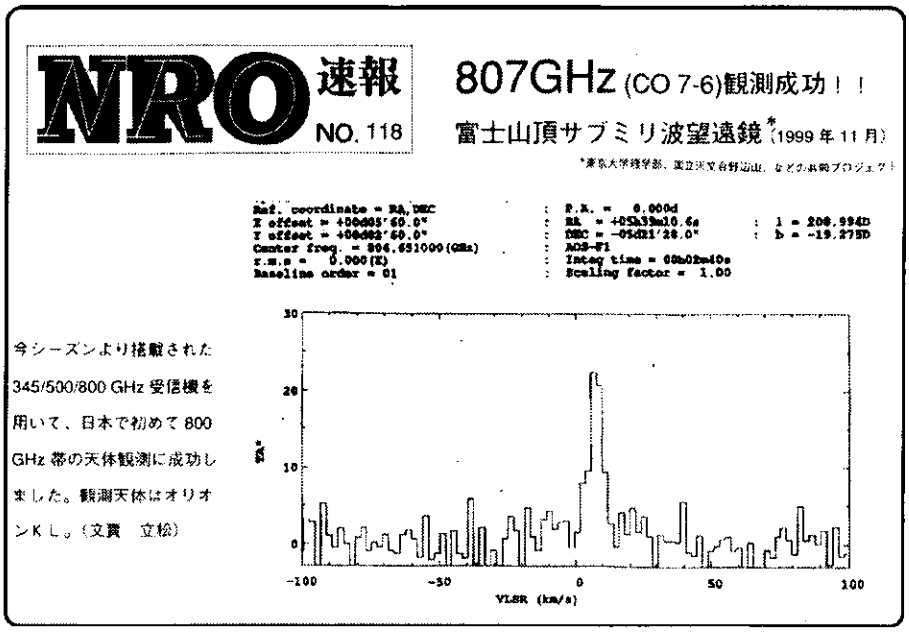

Fig. A.8 No. 118 of NRO News

Appendix B

Development of Software for the Mt. Fuji Submillimeter–wave Telescope

Abstract

In this chapter, the software for the Mt. Fuji submillimeter-wave telescope, which I developed, is explained. The program was developed using the "C language". Human direct access to the summit is extremently difficult in the observational season (winter). The summit and ground-level institutions are connected using the satellite communication, and the telescope at the summit is operated from the ground-level institutions. Therefore, reliability is very essential in the observation software. Besides, all of telescope control, monitor, and data transfer must be done in limited communication speed (64 kbps).

With this in mind, the program is designed as simple as possible, and so that minimum operation is possible even if the effective communication speed decreases. We prepared four scan modes to match various observational requests : One position, Raster scan, Spiral scan, and Random scan. The raw data is written in the group FITS format, which can be fed into the reduction software "NewStar" of Nobeyama Radio Observatory.

B.1 Telescope Control Program

I developed the observation program in order to match the following requirements.

- It must give very high reliability so that the telescope does not malfunction.
- At a limited communication speed (64 kbps), all of telescope control, monitor, and data transfer should be done.
- It must carry out observations very efficiently

Practical designs are as follows.

- Telescope commands and "status monitor" are character-based to minimize the load in communication.
- Even if the effective communications speed lowered, we can observe with the "minimum" two windows (status monitor and command).
- It displays window for Quick Look and various environmental monitor.

B.1.1 Functions

In the following, I list up various "functions" in the observation software.

For Antenna

open_ant()	Initializes the antenna control.
set_pos(&inform)	Gives positional information to the antenna.
if_inpos(&ipos)	Judges whether the tracking is completed (0) or not (1).
ant_read(&zahyo)	Read the telescope position from resolver and encoder.
close_ant()	Closes the antenna control

For Acousto-optical Spectrometer (AOS)

aos_init(int)	Initializes the AOS control and data acquisition.
set_aos(integ_time)	Gives information on integration to AOS.
aos_start()	Starts.
if_inaos(flag)	Judges whether integration is completed (0) or not (1).

get_aos(integ_data)	Acquires the data.
aos_stop()	Quits integration.
set_noise_source()	Turns on the noise source.
ret_noise_source()	Judges whether the noise source turns on (0) or off (1).
set_comb_generator()	Turns on the comb generator source.
ret_comb_generator()	Judges whether the comb generator turns on (0) or off (1).
set_attenuator(int)	Set attenuation to an absolute value.
change_attenuator(int)	Change attenuation a relative value.
ret_attenuator()	Reads the value of the attenuator.

For Frequency Synthesizer

open_synth(int)	Opens or closes the synthesizer operation. (1) open or (2) close.
set_synth(double)	Sets the frequency to the synthesizer.

For Chopper

open_chop(int)	Opens or closes chopper operation. (1) open or (2) close.
set_chopa()	Toggles the chopper in and out.
rec_chopa()	Judges the condition of the chopper. (0) Sky , (1) R, or (2) Error.

B.2 Flow of observation program

The flow chart of main function of the observation program is shown in Figure B.1.

B.3 Observation Table

The observation table is a text file having a filename "tbl", should be located in a directory "observation/table". Observers can use a favorite text editor(e.g. Mule, emacs, or vi). The format of observation table is

Keyword = value # comment.

It judges the end of table with a line of "end". It is possible to increase the number of keywords to much new requirements. Table B.1 shows an example used in 1999 winter.

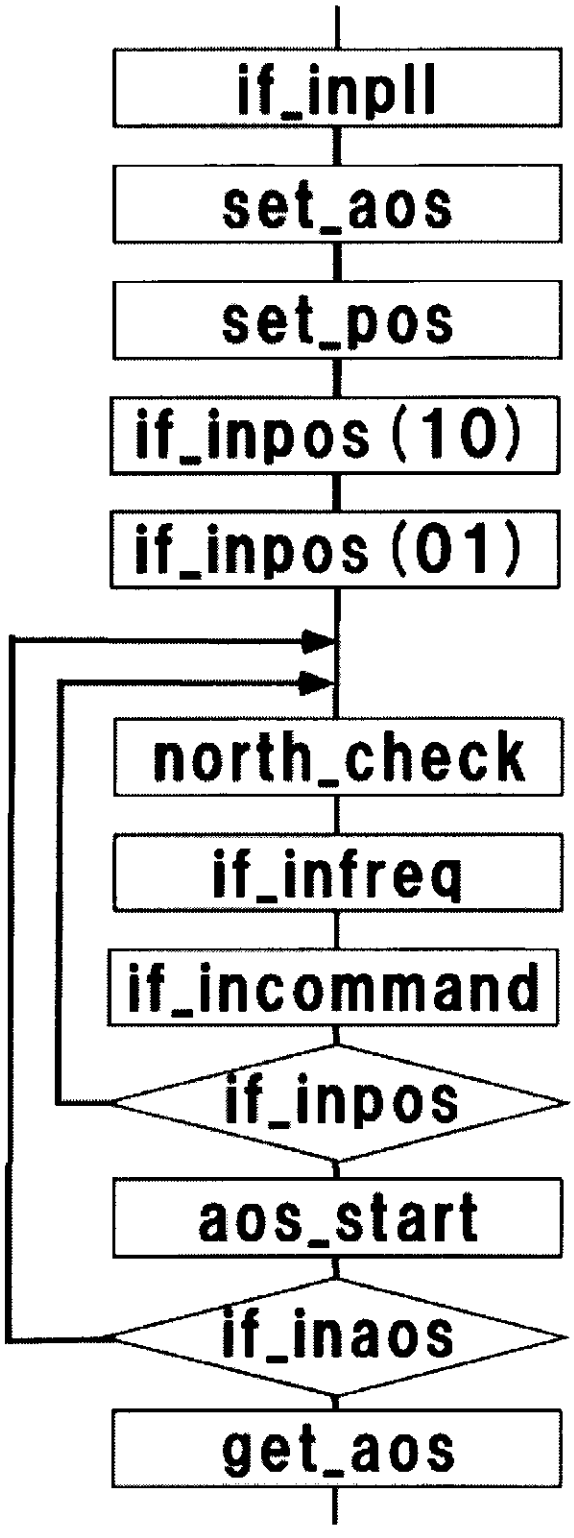

Fig. B.1 Flow chart of main function ofMt. Fuji submillimeter-wave telescope

B.3.1 Descriptions of the keywords

In this subsection, we explain the meaning of the keywords.

OBSERVER	The name of the observer. It should be sandwiched by " ' " and " ' ".
DENPA	Type of the object target. 0 : Radio source, 1 : Moon, 2 : Sun, 3 : Venus, 4 : Mars, 5 : Jupiter, or 6 : Saturn.
OBJECT	The name of the objects. It should be sandwitched by " ' " and " ' ".
ONRA、ONDEC	Coordinates of map reference center. ' hour : minute : sec ' , ' degree : minute : sec '
SWMODE	The mode of telescope switching 0 : position switching [RA, Dec], 1 : frequency switch, or 2 : position switching [Az, El].
OFFDAZ、OFFDEL	Coordinates of the position in minutes relative to the map reference center.
SWFREQ	The frequency in MHz relative to the IF frequency
OFFRA、OFFDEC	Coordinates of the off position. ' hour : minute : sec ', ' degree : minute : sec '
EPOCH	Epoch of the Equatorial coordinates.
VLSR	The reference LSR velocity for telescope tracking.
1CENTFREQ	Rest frequency in MHz
1IFFREQ	IF Frequency in MHz
1SIDBD	Sideband for observations. (0) USB or (1) LSB. At present, CO (J=3–2) is USB, and CI ($^3P_1$–$^3P_0$)is LSB.
2CENTFREQ、2IFFREQ、2SIDBD	2nd parameter for 2–band observation. Should be "0" in the single observations.
ERROR	Tracking error of the antenna in seconds
SEQUENCE	The number of "scans" to be repeated.
INTEGTIME	Integration time per point.

TABLE B.1

OBSERVER	=	'arikawa'	#	observer name
DENPA	=	0	#	0:radio 1:moon 2:sun 3:Venus 4:mars
			#	5:Jupiter 6:Saturn
OBJECT	=	'ariari'	#	object source name
ONRA	=	' 19:20:35.89 '	#	Right Assention
ONDEC	=	' 14:09:54.10 '	#	Declination
SWMODE	=	0	#	0:pos sw[RA,dec] 1:freq sw[MHz]:
			#	2:pos sw[Az,El]
OFFDAZ	=	15	#	off position daz [min]
OFFDEL	=	10	#	off position del [min]
SWFREQ	=	50	#	SW freq [MHz]
OFFRA	=	' 19:23:00.00 '	#	Right Assention
OFFDEC	=	' 14:20:00.00 '	#	Decision
EPOCH	=	1950	#	epoch
VLSR	=	71.9	#	Vlsr [km/s]
1CENTFREQ	=	345796.0	#	1st cent.freq[MHz]
1IFFREQ	=	2350	#	1st IF center freq[MHz]
1SIDBD	=	0	#	1st 0= & USB,1= & LSB
2CENTFREQ	=	492161.0	#	2nd cent.freq[MHz]
2IFFREQ	=	1950	#	2nd IF center freq[MHz]
2SIDBD	=	1	#	2nd 0= & USB,1= & LSB
ERROR	=	40.00	#	error circle [sec]
SEQUENCE	=	3	#	numall
INTEGTIME	=	10	#	integrate time[sec]
RSKYINTER	=	3	#	rsky numeber
MULTI	=	3	#	multi on-off
MAPMODE	=	2	#	0:One 1:Ras[RA,dec] 2:Spi[RA,Dec]
			#	3:Ran[RA,dec] 4:Cro[Az,El]
			#	5:Cro[RA,Dec] 6:Spi[Az,El]
SPACING	=	3.0,3.0	#	grid spacing(x,y) [min]
START	=	0,0	#	start offset(x,y) [min]
NPOINT	=	5,5	#	grid number(x,y)
DIRECTION	=	'+x,-y'	#	map start direction
RAND	=	0	#	
END				

RSKYINTER	The frequency of the chopper wheel calibration in units of off position.
MULTI	The number of continuing ON position.
MAPMODE	Scan mode. 0:One position 1:Raster scan[RA,dec] 2:Spiral scan[RA,Dec] 3:Random position scan[RA,dec] 4:Cross scan[Az,El] 5:Cross scan[RA,Dec] 6:Spiral scan[Az,El]
SPACING	Spacing grid in the mapping observation in minutes
START	Coordinate of relative to the map reference center the start point in minutes.
NPOINT	Grid numbers in RA and Dec in units of "SPACING"
DIRECTION	Raster direction for mapping. For example, $[+x, -y]$ rasters toward the plus direction (left) of RA by changing Dec to the negative direction (bottom).
RAND	Coordinates in random position observations.
END	End of the table.

B.4 Command

In this section, the telescope command is explained. The help is available by typing " ? " in the command window.

el **	Goes to the elevation ** (in degrees). The zenith is 90 degrees, and lower limit is the 16 degrees, and upper limit is the 89 degrees.
az **	Goes to the Azimuth ** (in degrees). North is 0 degrees.
table ***	Defines the observation table to be used. The extension ".tbl" should be omitted.
start m n	Observe m th point to n th point in the table. n, or, both m and n, can be omitted.
stop	Quits observation.
re	refreshes the status window.

tune	Sets up the synthesizer, and moves the antenna at the position in the map reference center. Should be used after defining the table (table command).
qlook	Starts the qlook window.
xrange m n	Changes the channel range of qlook display from m to n. The default value is m = 230ch and n = 850ch.
yrange m n	Changes the scale of the vertical axis of qlook window from m to n. Default is automatical scale. "0 0" to resume to the default.
rms m n	Changes the range of calculation of the rms noise level. Calculation uses the data for (m ch - m+100ch) and ($n$ch - n+100ch). In default, m is 250ch and n is 650ch.
chopon、**chopoff**	Turns on and turns off the chopper.
combon、**comboff**	Turns on and turns off the comb generator.
noiseon、**noiseoff**	turns on and turns off the noise source
setatt	Changes attenuator using the absolute value.
chaatt	Changes attenuator using the offset calue.
492att	In 2-band observations, it changes 492 GHz attenuator using the absolute value.
temp	Measures the latest temperatures of the chopper and the outside atmosphere.
tau492,tau345	Measures the opacity of 492GHz and 345 GHz, respectively, by the antenna tipping.
if345、**if492**、**ifboth**	Switches IF.
exit	Finishes the observation program.

B.5 Control and monitor of the devices

- The operating system for the main computer is Sun OS 4.1.4.
- The AOS relation control (controller, integrator, attenuator) : GP-IB.
- The antenna system control (motor, resolver, encorder) : RS-232C.
- The receiver control.

- The environment system (cooling , vacuum, thermometry) : RS-232C.
- The electric system (mixer relation, LO relation, PLL relation, spectrum analyzer) : GP-IB

- The standard clock (it acquires the time from the GPS) : RS-232C.
- Power stabilization and power down procedure (using the UPS) : RS-232C.
- Satelite communication.
  - The satellite communication of S-NET Co..
  - Communication equipment - terminal : V. 35 and Ethernet

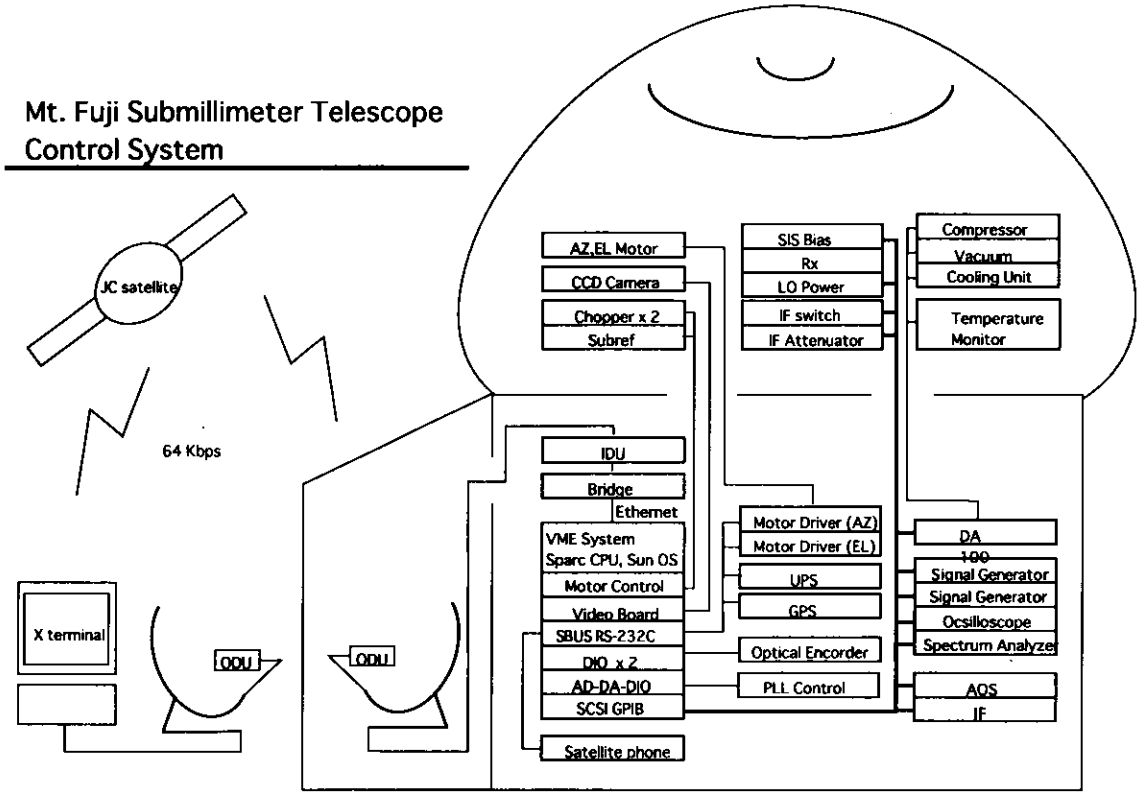

Fig. B.2 Block diagram of Mt. Fuji submillimeter-wave telescope

B.6 Header of FITS file

The raw data is written in the group FITS format (Sp FITS) in order to carry out the data processing by using the reduction software "NewStar" of Nobeyama Radio Observatory. The header of FITS for the Mt. Fuji submillimeter-wave telescope is as follows.

```
SIMPLE  =  T              /
BITPIX  =  32             /
NAXIS   =  2              /
NAXIS1  =  0              /
NAXIS2  =  1024           /
PCOUNT  =  32             /
GCOUNT  =  207            /
PTYPE1  =  'CRVAL2 '      /
PTYPE2  =  'CDELT2 '      /
PTYPE3  =  'RA '          /
PTYPE4  =  'DEC '         /
PTYPE5  =  'RAOJ '        /  RA OF MAP ENTER : VALUE IS DEGREE
PTYPE6  =  'DECOJ '       /  DEC OF MAP CENTER : VALUE IS DEGREE
PTYPE7  =  'DRA '         /  RA OFFSET : VALUE IS DEGREE
PTYPE8  =  'DDEC '        /  DEC OFFSET : VALUE IS DEGREE
PTYPE9  =  'RAF '         /  RA OF OFF : VALUE IS DEGREE
PTYPE10 =  'DECF '        /  DEC OF OFF : VALUE IS DEGREE
PTYPE11 =  'DRAF '        /  RA OFFSET OF OFF : VALUE IS DEGREE
PTYPE12 =  'DDECF '       /  DEC OFFSET OF OFF : VALUE IS DEGREE
PTYPE13 =  'FREQ '        /  CENTER FREQUENCY : VALUE IS HZ
PTYPE14 =  'FQTRK '       /  TRACKING FREQUENCY : VALUE IS HZ
PTYPE15 =  'FQIF1 '       /  1ST IF : VALUE IS HZ, ¡0 IF LSB
PTYPE16 =  'DATE-OBS'     /  YYMMDD.hhm0
PTYPE17 =  'ARRAY-NO'     /  AOS ARRAY NUMBER
PTYPE18 =  'IAVTM '       /  INTEGRATION TIME : VALUE IS SEC
PTYPE19 =  'NAVSP '       /  NO OF SPECTRA AVERAGED
PTYPE20 =  'RMS '         /  RMS NOISE LEVEL : VALUE IS K
PTYPE21 =  'NBASE '       /  DEGREE OF POLYNOMIAL FOR BASELINE FIT
PTYPE22 =  'SCFACT '      /  TA* SCALING HISTORY : ORIGINAL IS 1.0
PTYPE23 =  'TEMP-R '      /  ABSOVER TEMPERATURE
```

```
PTYPE24  =  'TEMP-SKY'  /  SKY TEMPERATURE
PTYPE25  =  'TAU '      /  OPACITY
PTYPE26  =  'DAZ '      /  AZIMUSTH OFFSET
PTYPE27  =  'DEL '      /  ELEVATION OFFSET
PTYPE28  =  'AZ '       /  AZIMUTH
PTYPE29  =  'EL '       /  ELEVATION
PTYPE30  =  'SWMOD '    /  SWITCH MODE
PTYPE31  =  'DFRQ '     /  FREQUENCY OFFSET
PTYPE32  =  ' '         /  NULL
PSCAL1   =  1000.000000 /
PSCAL2   =  1.000000    /
PSCAL3   =  0.000010    /
PSCAL4   =  0.000010    /
PSCAL5   =  0.000010    /
PSCAL6   =  0.000010    /
PSCAL7   =  0.000010    /
PSCAL8   =  0.000010    /
PSCAL9   =  0.000010    /
PSCAL10  =  0.000010    /
PSCAL11  =  0.000010    /
PSCAL12  =  0.000010    /
PSCAL13  =  1000.000000 /
PSCAL14  =  1000.000000 /
PSCAL15  =  1000.000000 /
PSCAL16  =  0.001000    /
PSCAL17  =  1.000000    /
PSCAL18  =  1.000000    /
PSCAL19  =  1.000000    /
PSCAL20  =  0.000010    /
PSCAL21  =  0.000010    /
PSCAL22  =  0.000010    /
PSCAL23  =  0.001000    /
PSCAL24  =  0.001000    /
PSCAL25  =  0.001000    /
PSCAL26  =  0.000010    /
PSCAL27  =  0.000010    /
PSCAL28  =  0.000010    /
PSCAL29  =  0.000010    /
PSCAL30  =  1.000000    /
PSCAL31  =  1000.000000 /
PSCAL32  =  0.000000    /
```

```
CRPIX2   =   512.000000   /
CTYPE2   =   'FREQ '      /
CROTA2   =   0.000000     /
BSCALE   =   0.000100     /
BZERO    =   0.000000     /
BUNIT    =   'K '         /
BLANK    =   -999999999   /
OBJECT   =   'W44OHE '    /
ORIGIN   =   'NOBEYAMA'   /
INSTRUME =   'NOBEYAMA'   /
TELESCOP =   'MT.FUJI '   /
OBSERVER =   'Arikawa '   /
EPOCH    =   1950.000000  /
END
```

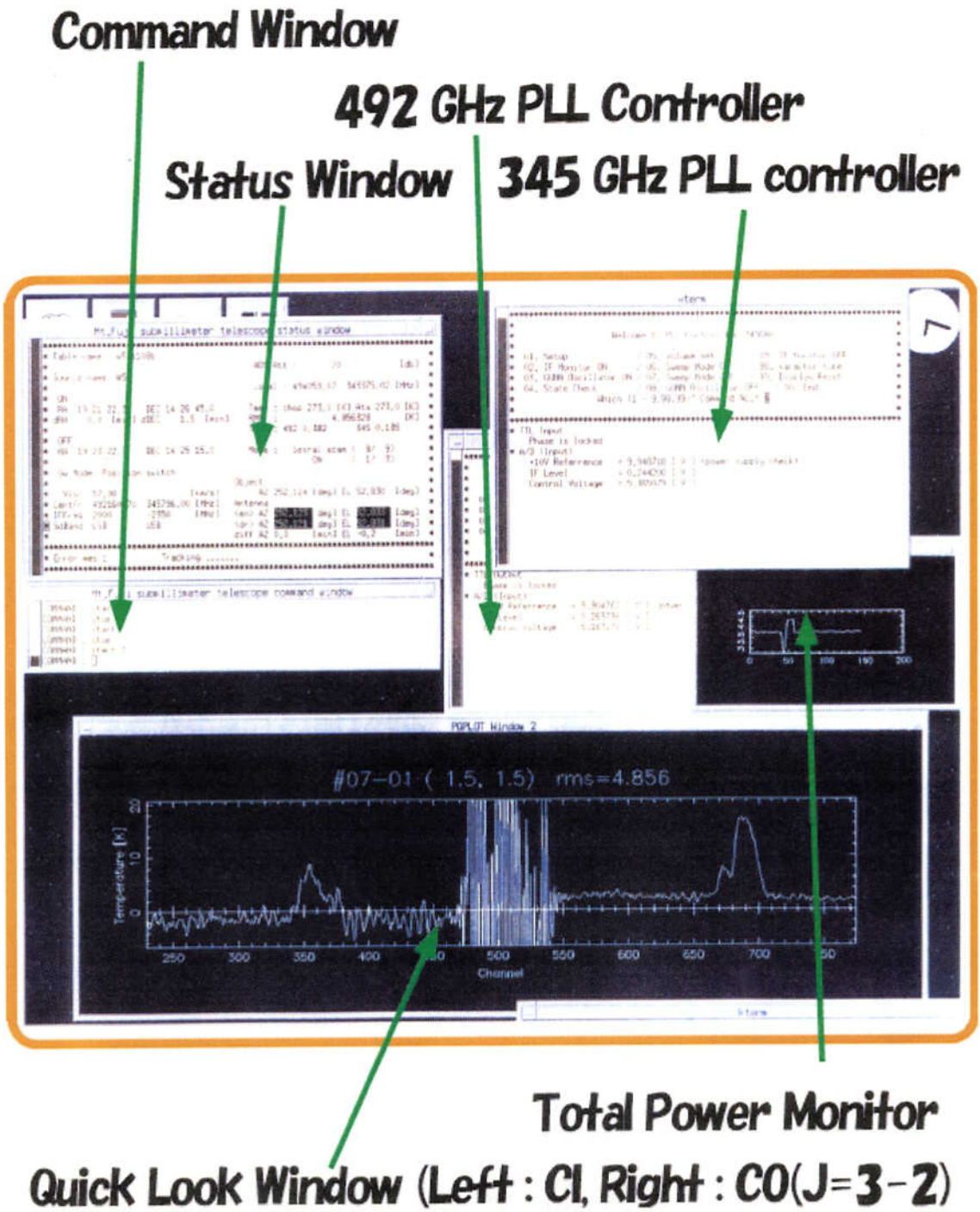

Fig. B.3 Example of observational window of Mt. Fuji submillimeter-wave telescope

Appendix C

LVG Model Calculations

This chapter explains the Large-velocity gradient (LVG) model (Goldreich & Kwan 1974, Scoville & Solomon 1974) It is necessary to solve the equation on radiation and collision at all levels in order to exactly calculate the molecular excitation state. LVG (Large-Velocity Gradient) model widely used in order to calculate the excitation state (e.g. Goldreich & Kwan 1974, Scoville & Solomon 1974). In this model, it is approximated that the molecular cloud has the velocity gradient, and that the photon radiated in some places is not absorbed in different places, since a different place has a different *Doppler* velocity.

Now, we consider the energy levels in Figure C. The rotational levels of diatomic molecule are indexed by the rotational angular-momentum quantum number J. The J rotational state has divided by the level degeneracy g_J. We define n_J per degeneracy, then the population in J state is $g_J n_J$. For normalization, we define n_J as

$$\sum_{J=0}^{\infty} g_J n_J = 1. \tag{C.1}$$

For J which degenerates in to g_J, we consider change of n_J by the collisional excitation, radiation, and absorption. The probability which transites from one of levels of J state which degenerates into g_J to the level of $J+1$, J-1 state by spontaneous emission, induction radiation, absorption can write

$$A_{J,J-1} n_J + B_{J,J-1} n_J I_{J,J-1} + B_{J,J+1} n_J I_{J,J+1}, \tag{C.2}$$

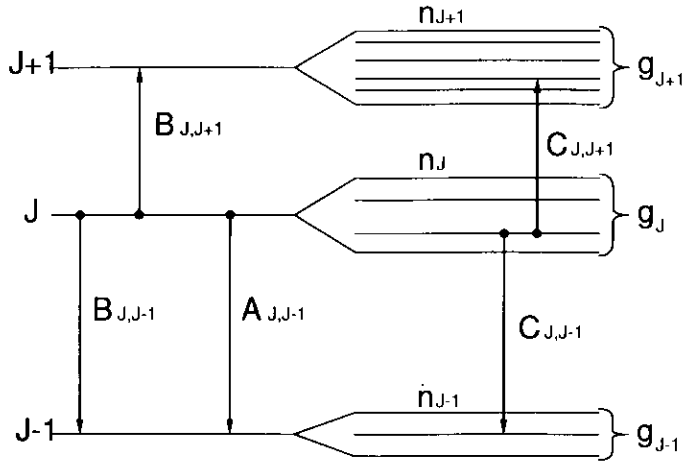

Fig. C.1 Levels of J state

where the first term represents the spontaneous emission, and the second term represents the induction radiation, and the third term represents the absorption. $I_{J,J-1}$ is the intensity of the transition from J to $J-1$ state. In black-body radiation of the temperature T, it can be written

$$I_{J+1,J} = \frac{2h\nu^3}{c^2}\frac{1}{\exp(h\nu/kT)-1} \tag{C.3}$$

$$\nu = \frac{E_{J+1}-E_J}{h}. \tag{C.4}$$

The probability which of the transition to J from $J+1$, $J-1$ by spontaneous emission, induction radiation, and absorption can be written as

$$\frac{1}{g_J}\left[(A_{J+1,J}n_{J+1}g_{J+1})+(B_{J+1,J}n_{J+1}g_{J+1})I_{J+1,J}+(B_{J-1,J}n_{J-1}g_{J-1})I_{J-1,J}\right]. \tag{C.5}$$

When there is the velocity shift ΔV in the inside of the molecular cloud, the opacity $\tau_{J+1,J}$ of transition to $J+1 \rightarrow J$ can be written

$$\tau_{J+1,J} = N(\mathrm{X})\frac{hc}{4\pi\Delta V}B_{J+1,J}g_{J+1}\left[n_J - n_{J+1}\right], \tag{C.6}$$

where $N(\mathrm{X})$ is column density of molecule X. The probability that the photon escapes

to the outside of the system is :

$$\beta_{J+1,J} = \frac{1 - e^{-\tau_{J+1,J}}}{\tau_{J+1,J}} \tag{C.7}$$

where, $\beta_{J+1,J}$ is called escape probability of the photon. If $\tau_{J+1,J}$ is small, $\beta_{J+1,J} \sim 1$. If $\tau_{J+1,J}$ is large, $\beta_{J+1,J}$ decreases as $\beta_{J+1,J} \sim 1/\tau_{J+1,J}$

For the collisional excitation and de-excitation, the probability of the transition from J to L is

$$\sum_{L=0}^{J-1} n(\mathrm{H}_2) C^d_{JL} n_J g_L + \sum_{L=J+1}^{\infty} n(\mathrm{H}_2) C^u_{JL} n_J g_L, \tag{C.8}$$

where $C^u_{J,L}$ means the probability of the excitation (upward collision) from lower level J to upper level L, and $C^d_{J,L}$ means the probability of the de-excitation (downward collision) from J to L. The electric dipole transition is allowed only for $\Delta J = 1$, while the transition de to collision occur between all levels.

In two level system in which collisional excitation and de-excitation have reached equilibriums from the Boltzmann distribution. We have :

$$\frac{dn_J}{dt} = n(\mathrm{H}_2) C^u_{LJ} n_L g_L - n(\mathrm{H}_2) C^d_{JL} n_J g_L = 0 \tag{C.9}$$

$$\frac{n_J}{n_L} = \exp\left(-\frac{E_J - E_L}{kT}\right) \tag{C.10}$$

the relational expression is deduced:

$$C^u_{LJ} = C^d_{JL} \exp\left(-\frac{\Delta E}{kT}\right) \tag{C.11}$$

where equation (C.11)is called detailed balance. From equations (C.2), (C.5), (C.8), one obtains a differential equation of

$$\begin{aligned}
\frac{dn_J}{dt} = {} & \frac{1}{g_J}\left[A_{J+1,J} n_{J+1} g_{J+1} + B_{J+1,J} n_{J+1} g_{J+1} I_{J+1,J} + B_{J-1,J} n_{J-1} g_{J-1} I_{J-1,J}\right] \\
& - A_{J,J-1} n_J - B_{J,J-1} n_J I_{J,J-1} - B_{J,J+1} n_J I_{J,J+1} \\
& + \sum_{L=0}^{J-1} n(\mathrm{H}_2) C^d_{LJ} n_L g_L + \sum_{L=J+1}^{\infty} n(\mathrm{H}_2) C^u_{LJ} n_L g_L \\
& - \sum_{L=0}^{J-1} n(\mathrm{H}_2) C^d_{JL} n_J g_L - \sum_{L=J+1}^{\infty} n(\mathrm{H}_2) C^u_{JL} n_J g_L
\end{aligned} \tag{C.12}$$

If it is in equilibrium, the equation (C.12) becomes zero. By solving equation (C.12) for all levels simultaneously, it is possible to calculate the molecular excitation state in given physical state (temperature and density). Reversely, it is possible to calculate the molecular abundance, when intensity and line width of observed molecular spectral line are given.

References

Goldreich P., & Kwan J., 1974, ApJ, 189, 441

Scoville N.Z., Solomon P.M. 1974, ApJ 187, L67